

**Wind Turbine Load Control and Estimation
Advancements by Coordinate Transformations**

Pamososuryo, A.K.

DOI

[10.4233/uuid:1b3750e2-a4bb-44f5-b07a-f4ebeb8db2c](https://doi.org/10.4233/uuid:1b3750e2-a4bb-44f5-b07a-f4ebeb8db2c)

Publication date

2024

Document Version

Final published version

Citation (APA)

Pamososuryo, A. K. (2024). *Wind Turbine Load Control and Estimation: Advancements by Coordinate Transformations*. [Dissertation (TU Delft), Delft University of Technology].
<https://doi.org/10.4233/uuid:1b3750e2-a4bb-44f5-b07a-f4ebeb8db2c>

Important note

To cite this publication, please use the final published version (if applicable).
Please check the document version above.

Copyright

Other than for strictly personal use, it is not permitted to download, forward or distribute the text or part of it, without the consent of the author(s) and/or copyright holder(s), unless the work is under an open content license such as Creative Commons.

Takedown policy

Please contact us and provide details if you believe this document breaches copyrights.
We will remove access to the work immediately and investigate your claim.

A landscape of wind turbines on rolling hills under a dramatic sky. The sky is a mix of dark blue and light yellow, suggesting a sunset or sunrise. The turbines are white and are scattered across the rolling hills. The foreground is a grassy field with some low-lying vegetation.

Wind Turbine Load Control and Estimation: Advancements by Coordinate Transformations

Atindriyo Kusumo Pamososuryo

Wind Turbine Load Control and Estimation

Advancements by Coordinate Transformations

Wind Turbine Load Control and Estimation

Advancements by Coordinate Transformations

Proefschrift

ter verkrijging van de graad van doctor
aan de Technische Universiteit Delft,
op gezag van de Rector Magnificus prof. dr. ir. T.H.J.J. van der Hagen,
voorzitter van het College voor Promoties,
in het openbaar te verdedigen op
vrijdag 19 april 2024 om 10.00 uur

door

Atindriyo Kusumo PAMOSOSURYO

Ingenieur op het gebied van systeem- en regeltechniek,
Technische Universiteit Delft, Nederland,
geboren te Medan, Indonesië.

Dit proefschrift is goedgekeurd door de promotoren.

promotoren: Prof. dr. ir. J.W. van Wingerden
Dr. R.M.G. Ferrari
copromotor: Dr. ir. S.P. Mulders

Samenstelling promotiecommissie bestaat uit:

| | |
|-----------------------------------|-------------------------------|
| Rector Magnificus, | voorzitter |
| Prof. dr. ir. J.W. van Wingerden, | Technische Universiteit Delft |
| Dr. R.M.G. Ferrari, | Technische Universiteit Delft |
| Dr. ir. S.P. Mulders | Technische Universiteit Delft |

Onafhankelijke leden:

| | |
|------------------------------|---|
| Prof. dr. D. von Terzi | Technische Universiteit Delft |
| Prof. dr. ir. M. Langelaar | Technische Universiteit Delft |
| Prof. dr. P.W. Cheng | Universit t Stuttgart, Duitsland |
| J.D. Grunnet, M.Sc.EE, Ph.D. | SEWPG European Innovation Center ApS, Denemarken |
| Dr. ir. H. Polinder | Technische Universiteit Delft, reservelid |



Keywords: wind turbine control, coordinate transformation, convex economic model predictive control, model demodulation transformation, modulation-demodulation control, periodic load estimation

Printed by: Gildeprint

Cover: “Wind turbines during daytime.” Photo by Dragon Pan on Unsplash

Style: Adapted from:
TU Delft House Style, with modifications by Moritz Beller
<https://github.com/Inventitech/phd-thesis-template>

Copyright   2024 by A.K. Pamososuryo
ISBN 978-94-6366-842-2

All research data and code supporting the findings described in this dissertation are available in 4TU.Centre for Research Data at
<https://doi.org/10.4121/fec1562d-7968-4e24-9660-d3ed5ac118e6>

An electronic version of this dissertation is available at
<http://repository.tudelft.nl/>.

For Kristy and Edgar.

Contents

| | |
|---|-------------|
| Summary | xi |
| Samenvatting | xiii |
| Acknowledgments | xvii |
| 1 Introduction | 1 |
| 1.1 Climate crisis and wind energy | 2 |
| 1.2 Control of modern wind turbines. | 3 |
| 1.2.1 Wind turbine components | 3 |
| 1.2.2 Control objectives and conventional strategies | 4 |
| 1.3 State-of-the-art and challenges | 10 |
| 1.4 Thesis objective and contributions | 12 |
| 1.5 Thesis organization. | 14 |
| 2 Individual Pitch Control by Convex Economic Model Predictive Control for Wind Turbine Side-Side Tower Load Alleviation | 17 |
| 2.1 Introduction | 18 |
| 2.2 Nominal Wind Turbine Model | 19 |
| 2.3 Transformed Wind Turbine Model | 21 |
| 2.4 Convex Economic Model Predictive Control Formulation | 23 |
| 2.5 Simulation Results and Discussions | 24 |
| 2.5.1 Steady Wind Case | 25 |
| 2.5.2 Turbulent Wind Case. | 26 |
| 2.6 Conclusions | 28 |
| 3 Convex Economic Model Predictive Control for Blade Loads Mitigation on Wind Turbines | 29 |
| 3.1 Introduction | 30 |
| 3.2 Wind Turbine Model | 32 |
| 3.2.1 Drivetrain Dynamics. | 33 |
| 3.2.2 Static Blade and Rotor Moments Formulation | 34 |
| 3.2.3 Potential Nonconvexity and Related Challenges for CEMPC-IPC Design | 35 |
| 3.3 Transformed Wind Turbine Model | 36 |
| 3.3.1 Kinetic Energy Dynamics | 37 |
| 3.3.2 Static Blade and Rotor Moments in Power and Energy Terms | 38 |
| 3.4 Convex Economic Model Predictive Control Setup | 39 |
| 3.4.1 Optimal Control Problem Formulation | 40 |
| 3.4.2 Estimator Designs | 42 |

| | | |
|----------|--|------------|
| 3.5 | Simulation Results and Discussions | 44 |
| 3.5.1 | Step Wind | 45 |
| 3.5.2 | Turbulent Wind | 48 |
| 3.6 | Conclusions | 55 |
| 4 | Periodic Load Estimation of a Wind Turbine Tower using a Model Demodulation Transformation | 57 |
| 4.1 | Introduction | 58 |
| 4.2 | Nominal Wind Turbine Model | 59 |
| 4.3 | Extended Demodulated Model | 60 |
| 4.3.1 | Extended Demodulated State Equation | 63 |
| 4.3.2 | Output Equation Derivation | 63 |
| 4.3.3 | Measurement Signal Demodulation | 64 |
| 4.4 | Kalman Filter Design | 64 |
| 4.5 | Case Study | 65 |
| 4.5.1 | Model Validation | 65 |
| 4.5.2 | Kalman Filter Performance Assessment | 66 |
| 4.6 | Conclusions | 69 |
| 5 | On the Analysis and Synthesis of Wind Turbine Side-Side Tower Load Control via Demodulation | 71 |
| 5.1 | Introduction | 72 |
| 5.2 | Wind Turbine Dynamics and Conventional Tower Damping Controller | 74 |
| 5.2.1 | Tower and aerodynamic models | 74 |
| 5.2.2 | Conventional Active Tower Damping Controller | 76 |
| 5.2.3 | Frequency Domain Representation | 77 |
| 5.3 | Modulation-Demodulation Control Scheme | 77 |
| 5.4 | MDC Controller and System Analysis | 79 |
| 5.4.1 | SISO Modulated Controller Representation | 80 |
| 5.4.2 | MIMO Demodulated Plant Representation | 82 |
| 5.4.3 | Application of MDC on a Simplified Wind Turbine | 83 |
| 5.5 | Quadrature and In-Phase Channels Decoupling by Phase Offset Inclusion | 86 |
| 5.5.1 | Relative Gain Array Analysis | 86 |
| 5.5.2 | Phase Offset Inclusion | 87 |
| 5.6 | Simulation Results | 90 |
| 5.6.1 | Simplified Turbine Simulations | 90 |
| 5.6.2 | OpenFAST Simulations | 93 |
| 5.7 | Conclusions | 100 |
| 6 | Conclusions and Recommendations | 101 |
| 6.1 | Conclusions | 102 |
| 6.2 | Recommendations | 103 |
| A | Turbulent Wind Case Simulation Results | 105 |
| | Bibliography | 107 |
| | Curriculum Vitæ | 117 |

List of Publications

119

Summary

Wind energy has become one of the most economically attractive energy sources thanks to technological advances, such as wind turbine upscaling. To harness higher-quality wind reachable at greater heights, wind turbine towers are made taller; to increase power capture, rotors are made with wider diameters. Mass/material reduction for the manufacture of such components is thus imperative to keep large-scale turbines profitable, resulting in more flexible structures but exacerbating fatigue loading. Therefore, the reliance on advanced control methods is ever higher to mitigate multiple wind turbine structural loads while ensuring optimal power production.

Advanced convex economic model predictive control (CEMPC) methods have garnered attention lately in the wind turbine control community. Such techniques possess several advantages apart from those inherent in being subsets of the model predictive control (MPC) family. First, it is capable of accounting for multiple economic objectives for wind turbines, such as power production optimization, fatigue load reduction, and excessive actuation limitation, in a straightforward and unified way. This also means that the trade-off calibration between the economic objectives (by weight tuning) can be done with ease. Additionally, the convexity of the underlying optimization control problem (OCP) guarantees that a globally optimal solution can be found with high numerical effectiveness, which may lead to real-time feasibility. This thesis, in particular, is focused on the development of a unified CEMPC framework, combining the potentials of two emerging CEMPCs in the wind turbine area, namely the power-and-energy CEMPC and the quasi-linear parameter-varying model predictive control (qLPV-MPC), for addressing multiple wind turbine structural loads.

The former achieves its convexity by exchanging nominal wind turbine variables, such as blade pitch, generator torque, and rotational speed, with alternative variables in terms of aerodynamic and generator powers and rotor kinetic energy. This results in the OCP containing linear dynamics, convex constraints, and concave objectives to be maximized. Being originally focused on fulfilling power gradient requirements from a grid code, a fatigue load mitigation consideration was introduced later on for fore-aft tower motion in the literature. Unfortunately, little attention was paid to the mitigation of the more weakly-damped side-side tower loading, as well as blade fatigue loads.

Such a knowledge gap is filled in this thesis; in particular, both key components' fatigue loads are mitigated by exploiting the individual blade pitching capabilities of the power-and-energy CEMPC framework. Since, in this framework, blade pitch actuation is achieved mainly by manipulating aerodynamic power inside the CEMPC, a redefinition of the latter is necessary to enable such a feature. To be precise, multiple aerodynamic powers, each representing that of a single blade, were employed as decision variables of the CEMPC instead of a single quantity. Further mapping of the aerodynamic powers into side-side blade forces, as well as augmentation of side-side tower dynamics into the CEMPC's internal model, enables counteractive control actions for reducing side-side

tower load. Mapping the powers into blade and rotor moments enables alleviation of the blade loads.

On the other hand, the utilization of qLPV-MPC for deploying a passive wind turbine tower resonance prevention by dynamically optimal frequency skipping has been gaining attention in the literature. For enabling active load cancelation in this framework, however, a periodic load estimation is needed. In this thesis, such an estimation scheme is developed, employing a Kalman filtering method. Aligned with the qLPV-MPC implementation for the aforementioned passive method, the internal model of the filter is rendered in a demodulated fashion by applying a model demodulation transformation (MDT) to an extended wind turbine side-side tower dynamics. Measurement signal demodulation (MSD) is utilized for capturing the slow-varying components of wind turbine tower measurements to be fed to the Kalman filter. The filter is thus capable of not only estimating the demodulated periodic load signals but also those of the unknown and unmeasured tower states with good agreement with the ground truth.

The next challenge addressed in this thesis is the provision of an active control method specifically aimed at tackling the side-side periodic loading of the tower. A family of repetitive control methods, namely modulation-demodulation control (MDC), is adopted in this thesis to handle the cancellation of the periodic loading. In principle, MDC consists of output signal demodulation, projecting the frequency component of interest (namely the rotor frequency) in the signal into low-frequency quadrature and in-phase representations. On these axes, diagonal single-input, single-output (SISO) controllers can be designed, resulting in control signals, which, by a modulation process, are translated into a single control signal, being an additive generator torque signal, oscillating at the frequency of the disturbance and thereby canceling it. A phase offset, with its optimal value determined by the plant's phase at the disturbance frequency, is needed and included in the modulation. This results in the full decoupling of the control channels, as well as the correction of an occurring gain sign flip due to the varying excitation frequency, which could have deteriorated the controller's performance and induced instabilities. The MDC extends a conventional tower damper controller specifically aimed at mitigating the tower loading at its natural frequency. As a result, both the tower load components at the natural frequency and the rotor frequency are mitigated simultaneously.

This thesis has, thus, highlighted the significant role various coordinate transformations play in advancing state-of-the-art wind turbine control, be it a transformation of signals into a different set of variables in power and energy terms or into different time scales. The former has enabled the formulation of power-and-energy CEMPC for side-side tower load and blade loads mitigation, extending this framework's fatigue load mitigation capabilities. The latter transformation, demonstrated by the MDT, paves the way for estimating unknown and unmeasurable periodic load and tower states in a demodulated manner, essential in activating the periodic load cancelation feature of the novel qLPV-MPC method. The MDC method has successfully enabled active side-side periodic tower load cancelation by leveraging a modulation-demodulation scheme, another way of transforming coordinates into different time scales where convenient yet effective control system design can be made. This thesis has, therefore, provided elements required for constructing a unified CEMPC framework, where the benefits of the said coordinate transformations may be further harnessed.

Samenvatting

Windenergie is een van de meest economisch aantrekkelijke energiebronnen geworden dankzij de technologische vooruitgang, zoals het opschalen van windturbines. Om de hogere kwaliteit wind beschikbaar op grotere hoogten te benutten worden windturbinetoren langer gemaakt; om de vermogensopbrengst te vergroten worden rotors met bredere diameters gemaakt. Massa-/materiaalreductie voor de productie van zulke componenten is dus noodzakelijk om grootschalige windturbines winstgevend te houden, resulterend in meer flexibele structuren maar groeiende vermoeiingsbelasting. Daarom wordt steeds meer vertrouwd op geavanceerde regelmethode om meerdere structurele windturbinebelastingen te verminderen terwijl optimale vermogensopbrengst wordt gegarandeerd.

Geavanceerde convexe economische modelvoorspellende regelmethode (CEMPC) hebben recent aandacht verzameld in de windturbine-regelingsgemeenschap. Zulke technieken beschikken over een aantal voordelen bovenop de eigenschappen die inherent zijn aan het zijn van subsets van de familie van modelvoorspellende regelmethode (MPC). Ten eerste zijn ze in staat op een heldere en verenigde manier rekening te houden met meerdere economische doelen voor windturbines zoals optimalisatie van vermogensopbrengst, vermindering van vermoeiingsbelasting, en beperking van bovenmatige actuatie. Dit betekent ook dat de kalibratie van de afwegingen tussen deze economische doelen (door middel van het afstellen van je gewichten) gemakkelijk kan worden gedaan. Daarnaast garandeert de convexiteit van het onderliggende optimalisatie regelprobleem (OCP) dat een globaal optimale oplossing kan worden gevonden met hoge numerieke effectiviteit, wat kan leiden tot haalbaarheid in echte tijd. Dit proefschrift, specifiek, concentreert zich op de ontwikkeling van een verenigd CEMPC-kader, waarin het potentieel van twee opkomende CEMPC's op het gebied van windturbines wordt gecombineerd, namelijk de vermogen-en-energie CEMPC en de quasi-lineaire parametervariërende modelvoorspellende regelaar (qLPV-MPC), voor het aanpakken van meerdere structurele windturbinebelastingen.

De eerste bereikt zijn convexiteit door het uitwisselen van nominale windturbinevariabelen, zoals bladhoek, generatorkoppel, en draaisnelheid, met alternatieve variabelen in termen van aerodynamisch- en generatorvermogen en kinetische energie van de rotor. Dit resulteert in het OCP bestaande uit lineaire dynamica, convexe beperkingen, en concave doelen om te maximaliseren. Van oorsprong geconcentreerd op het voldoen aan vermogensgradiënten van een elektriciteitsnetcode, is later in de literatuur een overweging van vermoeiingsbelasting toegevoegd op de voor-achter torenbeweging. Ongelukkigerwijs is er weinig aandacht geschonken aan de vermindering van de zwakker gedempte zij-zij torenbelasting, alsook de vermoeiingsbelastingen op de bladen.

Dit kennistekort wordt behandeld in dit proefschrift; in het bijzonder wordt de vermoeiingsbelasting van beide sleutelonderdelen verminderd door de mogelijkheid tot individuele bladhoekdraaiing van het vermogen-en-energie CEMPC-kader te benutten. Omdat, in dit kader, bladhoekactuatie hoofdzakelijk wordt bereikt door het manipuleren van

aerodynamisch vermogen in de CEMPC is een herdefinitie noodzakelijk om deze functie toe te voegen. Om precies te zijn worden meerdere aerodynamische vermogens, die elk een enkel blad vertegenwoordigen, ingezet als beslissingsvariabelen in de CEMPC in plaats van een enkele grootheid. Verder vertalen van aerodynamische vermogens naar zij-zij krachten op de bladen, alsook toevoeging van zij-zij torendynamica in het interne model van de CEMPC, maakt tegenwerkende regelacties mogelijk voor het verminderen van de zij-zij torenbelasting. Het vertalen van vermogens naar momenten op bladen en rotor maakt verlichting van de bladbelastingen mogelijk.

Aan de andere kant krijgt het gebruik van de qLPV-MPC groeiende aandacht in de literatuur voor het inzetten van een passieve preventie van windturbinetorenresonantie door dynamische optimale overslaan van frequenties. Voor het realiseren van actieve belastingsopheffing in dit kader is echter een periodische belastingsschatting nodig. In dit proefschrift wordt zo een schattingsschema ontwikkeld met behulp van een Kalmanfiltermethode. Op een lijn met de qLPV-MPC implementatie van de eerdergenoemde passieve methode, wordt het interne model van het filter op een gedemoduleerde manier opgezet door het toepassen van de modeldemodulatietransformatie (MDT) op een uitbereide zij-zij torendynamica van een windturbine. Meetsignaaldemodulatie (MSD) wordt benut voor het vangen van de langzaamvariërende componenten van de windturbinetorenmetingen om in te voeren in het Kalmanfilter. Het filter is daarmee in staat niet alleen de gemoduleerde periodieke belastingssignalen te schatten, maar ook die van de onbekende en ongemeten torentoestanden met goede overeenkomst met de grondwaarheid.

De volgende uitdaging aangepakt in dit proefschrift is de voorziening in een actieve regelmethode specifiek gericht op het aanpakken van de periodieke zij-zij belasting van de toren. Een familie van repetitieve regelmethoden, namelijk modulatie-demodulatie regeling (MDC), wordt toegewend in dit proefschrift om de opheffing van de periodieke belasting aan te pakken. In principe bestaat MDC uit demodulatie van het uitgangssignaal en projectie van de frequentiecomponent van interesse (namelijk de rotorfrequentie) uit het signaal naar de langzame-frequentie quadratuur en in-fase representaties. Op deze assen kunnen diagonale enkele-ingang, enkele-uitgang (SISO) regelars worden ontworpen, resulterend in regelsignalen welke door een modulatieproces worden vertaald in een enkel regelsignaal, zijnde een additief generatorkoppelsignaal, oscillerend op de frequentie van de verstoring en waardoor deze wordt opgeheven. Een faseverschuiving, met zijn optimale waarde bepaald door de fase van het systeem op de verstoringfrequentie, is nodig en ingesloten in de modulatie. Dit resulteert in volledige ontkoppeling van de regelkanalen, alsook de correctie van een optredende tekenwisseling in de versterking door de variërende excitatiefrequentie, welke had kunnen leiden tot verslechtering van de prestatie van de regelaar en instabiliteiten. De MDC breidt een conventionele torendempingsregelaar uit specifiek gericht op het verminderen van de torenbelasting op de natuurlijke frequentie. Als gevolg worden beide torenbelastingcomponenten tegelijk verminderd op zowel de natuurlijke frequentie als de rotorfrequentie.

Dit proefschrift heeft de significante rol uitgelicht die verschillende coördinatentransformaties spelen in de vooruitgang van meest geavanceerde windturbिनeregelingen, zowel met transformatie van signalen naar een andere set variabelen in termen van vermogen en energie als naar andere tijdsschalen. De eerste heeft de formulering mogelijk gemaakt van vermogen-en-energy CEMPC voor vermindering van zij-zij torenbelasting en bladbelas-

tingen, waarmee de mogelijkheden voor vermindering van vermoeiingsbelasting binnen dit kader zijn uitgebreid. De tweede transformatie, gedemonstreerd door de MDT, maakt de weg vrij voor het schatten van onbekende en onmeetbare periodieke belastingen en torentoestanden op een gedemoduleerde manier, essentieel voor het activeren van de periodieke belastingsopheffingsfunctie in de nieuwe qLPV-MPC methode. De MDC methode heeft succesvol actieve periodieke zij-zij torenbelastingsopheffing mogelijk gemaakt door het benutten van een modulatie-demodulatie schema, een andere manier op coördinaten te transformeren naar verschillende tijdsschalen waarmee een handig maar effectief regelsysteemontwerp kan worden gemaakt. Dit proefschrift heeft daarmee voorzien in de benodigde onderdelen voor de constructie van een verenigd CEMPC-kader waarin de voordelen van de genoemde coördinatentransformaties verder kunnen worden benut.

Acknowledgments

In February 2018, I wrapped up my MSc in Systems and Control at TU Delft, where I worked together with Jan-Willem van Wingerden and Sebastiaan Mulders as my supervisors for the thesis project. Doing research with this group further sparked my interest in the wind turbine control field; thus, I wanted to do a PhD. A position in the same group opened about a year later and after several email correspondences with Jan-Willem, we scheduled a Skype meeting to discuss the PhD position further. “Do you wanna do this PhD?” he asked, “Yes, of course!” was my answer—me in a hospital in Indonesia, as my son had just been born about 12 hours before, and he was in a hotel in the US. That’s how it started.

My first promotor, Jan-Willem, thank you for the trust and the opportunity. It’s been such an experience doing research with you; your enthusiasm, curiosity, guidance, encouragement, and reminder for me to be more pragmatic. To my second promotor, Riccardo, thank you for your curiosity and critical attitude; you have set me an example. My copromotor Sebastiaan, it is funny to think that you graduated from your PhD and left the group for about a year, then we met again and worked together—just like during my MSc thesis. Thank you for being a great mentor; not only did you teach me a lot about writing more engagingly, but you also told me to keep my work-life balance in check (“Promise yourself not to work on weekends!”). I also want to use this opportunity to thank Jacob, who helped me kickstart my economic MPC studies in the first months of my PhD, and Tobias, with whom I wrote my first two papers on the topic. Thank you for sharing your vast knowledge and insights, it’s been a great experience working with industrial experts like you, and I look forward to working with you again in the future.

Next, I’d like to thank the whole DCSC wind energy control group (the number of which has ‘exploded’ compared to when I started) without whom the (old and new) second floor and *Kraaiennest* would be less vibrant and fun. Yichao, I learned much from your open attitude, strong work ethic, and good humor: you kept telling me, “Don’t work too hard!” while you clearly worked the hardest. Thanks for helping me a lot in the early phase of my PhD! Maarten, we shared the same office for almost four years; during this period I always enjoyed our conversations, about work or personal life. Most importantly, you never fail to show integrity in whatever you do—please don’t stop! Livia (ciao!), although we know things haven’t always been easy, you have very strong willpower and a fighting spirit; at the end of the day, you always make it. I’ve always enjoyed our conversations from learning some new Italian words to personal challenges in my PhD; I wouldn’t have been able to tackle them if I had not talked with you! Daniel, my sole (so far) commute partner from the Hague; thank you for making my commute much less boring with our discussions about so many things (floating turbines, the Helix, marathon, etc.), which sometimes (somehow) ended up about a cat screaming in the morning or Steam Deck™. Mees, thanks for the everyday humor in the office, your (sometimes) unstoppable left-hand shots on the foosball table, and the awesome collaborations in the past years. I still don’t get how

you managed to travel the world westward by jumping from conference to conference and making *rendang* from scratch (*fuiyoh!*). Daan, it has always been enjoyable talking about our kids and how they grow up; at least with you, I have someone I can relate to in the group (talking about PAW Patrol with others would feel weird). Despite no longer being a part of the group, I want to thank Alessandro, who helped me in the PoliMi turbine assembly, and for being that friendly, Italian face at wind energy conferences! It has also been pleasant to work and have a chat with you Unai, Marcus, David, Amr, Rogier, Emanuel, Jonas, Bert, Marion, Guido, Matteo, Tim, Jesse, Uwe, Claudia, Bart, Joeri, Sachin, Alex, Zhixin, and Jean—you are amazing! Apart from the wind people, DCSC also wouldn't be as fun without you: Abhimanyu, Coen, Clara, Edoardo, Frederiek, Frederik, Frida, Gabriel, Ivo, Jacques, Léonore, Max, Pascal, Paul, Roger, Samuel, Sander, Sreeshma, and Tushar. Grateful to have you all as colleagues! Furthermore, I can't thank the hard-working DCSC (former) secretaries and managers enough: Marieke, Heleen, Francy, Martha, Anna, Bo, Erica, and Sandra; I owe you so much!

Outside of research, I'm grateful for taking a small part of the Wind Turbine Design course as a "control TA." Michiel and Dominic, teaching/assisting students in this course with you had been fun and I've never seen teachers so passionate as you. To my co-TAs, Mihir, Deepali, and Rishikesh: thanks for the nice collaborations!

Living 11.000+ km away from my home country, I'm most grateful for my fellow Indonesians with whom I shared the highs and lows of living abroad. Aldy and Bramka (and Bitu), we did our Master's together, then reunited as fellow PhDs; it wouldn't be as enjoyable coming back to Delft without seeing some familiar faces: grabbing some ice cream at Delft's center or watching the sunset at Kijkduin; thank you! During the COVID-19 pandemic, David, Rene, Denis, and Sandy had been such nice housemates (and landlady): thank you for the support, chats, barbecues, and movie evenings! Pak Stanley and the whole GKIN-RWDH congregation: thank you for the fellowship and always-welcoming gestures! Weekends can be really boring without you guys: Albert, Diaz, Annisa (and Bart), Wicak, Desy, Teddy, Ike, Sandy, Dissy, Doni, Tia, Markus, Carol, Geo, and Lena, thank you for the laughs and food!

My unwavering supporters—my family, my final thank yous are for you: my mother Magdalena, thank you for your love and prayers; my brother Anugrah and sister Anggraini, thank you for always giving me the right advice whenever I needed it and for caring for our mother while this little brother of yours was away. My parents-in-law, Djahyo and Soerti, thank you also for your prayers and support. To the love of my life: Kristy, thank you for always being there by my side since the beginning of my PhD journey, for the always-honest feedback, the tireless motivation when I'm not at my best, and for the random midnight Samyang dinners. My son, Edgar, the past four years flew really fast; seeing you grow and better understand what's happening around you has been most wonderful and the excitement you show whenever I return from work has always been my greatest joy. I hope I've set a good example for you in the future. For both of you: I'm sorry for not always being there when you needed me, for being late from work, and for the many evenings and weekends I spent working—it will just get better next time :).

Atindriyo
Den Haag, 19 April 2024

1

Introduction

Transitioning to sustainable energy sources such as wind energy is becoming ever-urgent, given the escalating destructive consequences of climate change driven by global fossil fuel consumption. In the past years, wind energy has grown into one of the most price-competitive energy sources, attributed to the technological advancements in the field, particularly the up-scaling of wind turbine sizes. Taller towers make high-quality wind at high altitudes harnessable and bigger rotors enable increased power capture, effectively reducing wind energy prices. Unfortunately, to keep large wind turbines economically viable, a reduction in the materials used to construct large wind turbines is deemed necessary, yielding more flexible structures and, thus, higher fatigue loading. Therefore, the urgency to employ advanced control methods, such as convex economic model predictive control (CEMPC), capable of mitigating multiple structural loads of wind turbines is ever higher. This thesis focuses on developing a load-mitigating CEMPC, unifying existing CEMPC frameworks in the literature. To provide additional background information and motivation for this research, this chapter will begin with a brief introduction to the latest trends in the field of wind energy, followed by a brief overview of modern wind turbine control. Then, a summary of state-of-the-art wind turbine control methods and challenges will be laid out, after which this thesis's main objective and contributions will be provided. The section will be closed with a brief outline of the thesis organization.

1.1 Climate crisis and wind energy

According to the 2023 Intergovernmental Panel on Climate Change (IPCC) report, the earth has become (on average) 1.1°C warmer than the beginning of industrialization [1]. This also means that the 1.5°C limit in the global temperature rise, as agreed upon by world leaders during the Paris Agreement in 2015 [2], is almost reached. In multiple regions of the world, destructive consequences of global warming have been reported: severe heatwaves [3], wildfires [4], flash floods [5], and droughts [6] have been shown to be linked with the increased worldwide temperature. Medical studies have also shown that a wide range of human diseases is aggravated by climate change [7]. Among several factors¹, the production of fossil-based energy is the main culprit of the global heating as it contributes to three-quarters of greenhouse gases emissions worldwide [1, 8]. A transition to sustainable energy sources with low carbon footprint, such as wind energy, is hence becoming ever urgent.

Wind power generation systems have been growing significantly in the past decades, with a new power capacity of 78 GW being added in 2022 to the worldwide electricity grid, adding up to 906 GW of total installed capacity, as reported by the Global Wind Energy Council (GWEC) [9]. It is forecasted that by 2024, the first terawatt installed capacity milestone will be reached, with the second terawatt anticipated by the end of the decade. This growth is associated with the continued efforts in lowering the levelized cost of energy (LCOE) [10], with onshore wind energy recently costing $\$0.03/\text{kWh}$ and its offshore counterpart $\$0.08/\text{kWh}$ [11].

The above-mentioned reduction in LCOE has been driven by the improvement of the wind turbine capacity by the distribution of fixed individual turbine costs over a greater (mega)wattage number [12]. Taller towers enable faster and richer quality wind (being less influenced by surface friction) at higher altitudes to be more accessible. Following this reasoning, in regions where only fair wind speeds are available a new market for wind power generation may be established [13, 14]. With tall towers, larger rotor installation is possible; thus, the resulting aerodynamic power—directly proportional to the square of rotor diameter—also increases². Subsequently, improved power production (and thus LCOE) can be achieved regardless of whether an increase in the generator capacity follows (such that rated power becomes higher) or not (allowing for the rated power to be reachable at lower wind speeds) [10, 12].

Nonetheless, when the upscaling is accomplished in a conventional manner, that is by maintaining the geometrical likeness from a reference turbine, the weight increase due to the added material of the upscaled machine may result in cost-prohibitiveness—contravening the original intention of upscaling. Therefore, in achieving the economic target of large wind turbines, material reductions in the structural design become imperative. This approach, nonetheless, often results in increased structural flexibility [14, 15], and thus more severe fatigue loading, as well as more prominent dynamic coupling between different turbine components [16]. These complexities pose additional challenges for wind turbine operations and in particular, emphasize the need for reliable, advanced control solutions by which safe wind turbine operation and continuous power production

¹Such as human lifestyles and patterns of consumption, land use, and land-use change.

²Under the assumption of an equal power coefficient among the rotors.

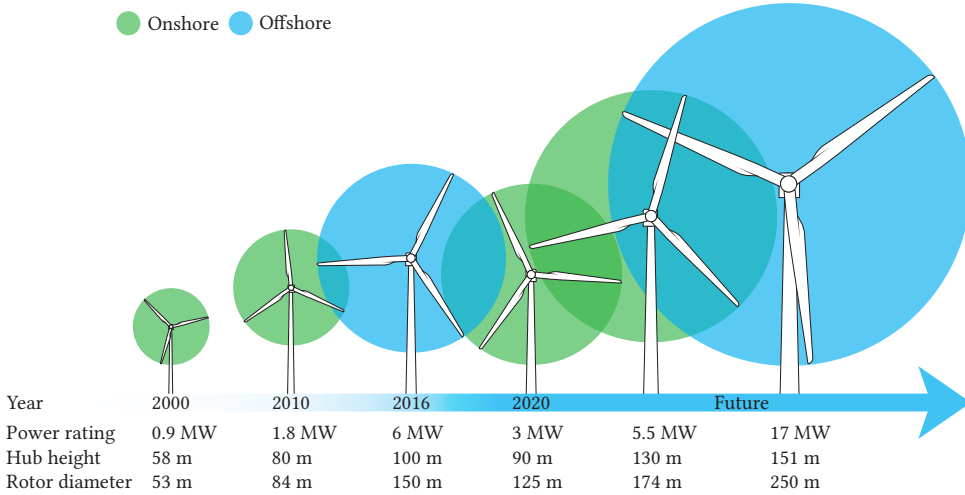


Figure 1.1: Wind turbine size growth throughout the past decades due to the upscaling trend. Wider rotors are designed to enhance power capture; taller towers enable high-quality wind at greater heights to be harnessable. Data collected from [17, 18].

can be ensured throughout its lifespan. In the following section, an introduction to the control aspects of modern wind turbines is presented.

1.2 Control of modern wind turbines

This section is dedicated to providing technical insight into modern wind turbine control aspects. First, a brief description of wind turbine components is given in Section 1.2.1. Then, in Section 1.2.2, the most essential objectives of wind turbine control systems are addressed, wherein the conventional control strategies for each objective are explained.

1.2.1 Wind turbine components

In the wind energy industry, utility-scale wind turbines are predominantly manufactured using the upwind ('facing-the-wind'), three-bladed, horizontal-axis configuration, known as the 'Danish' concept, as illustrated in Figure 1.2. The tower acts as a support structure, atop of which the nacelle is being mounted. The rotor, being an assemblage of the blades and a hub, develops torque from the kinetic energy in the wind, which is then transferred into a generator where the electricity is produced. Typically, a gearbox is also installed to convert the high torque and slow rotation of a rotor-connected low-speed shaft (LSS) into lower torque and faster rotation at the generator-connected high-speed shaft (HSS). A gearbox can also be dispensed from the design of a wind turbine such that there are no torque and speed conversions between the rotor and generator in a mechanism known as the direct-drive [19]. This rotor, gearbox, generator, and connecting shaft arrangement is known as the drivetrain, with the latter two components housed inside the nacelle. The rotor-nacelle assembly (RNA) can be yawed to align the rotor axis with the upcoming wind direction, thus preventing a loss in power generation and increased fatigue loading due

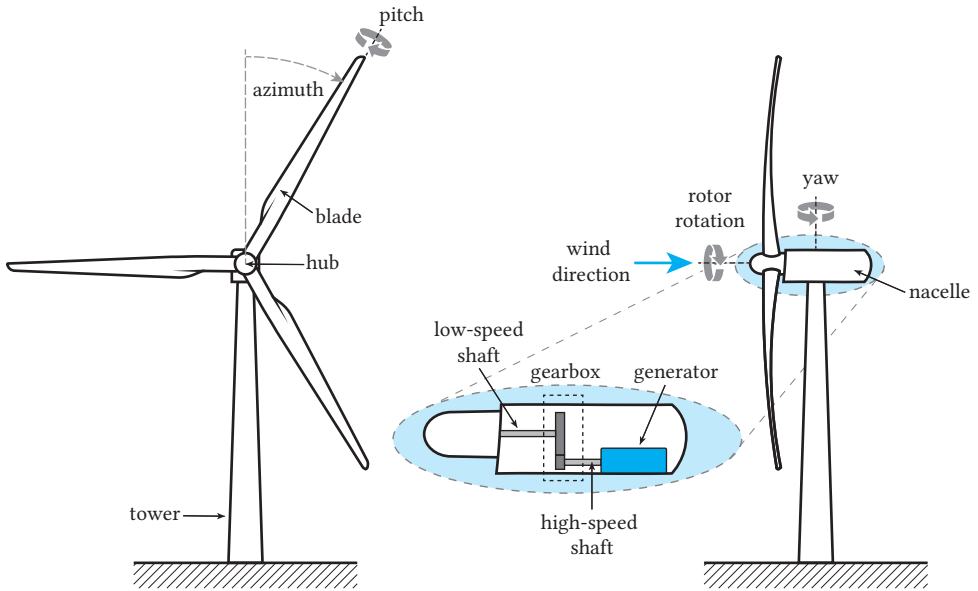


Figure 1.2: Main wind turbine components.

to the resulting rotor yaw moment. However, in wind farm settings, slightly misaligning wind turbines from the upcoming wind purposefully can help increase the overall wind farm production by deflecting the resulting wake from downstream turbines [20, 21].

1.2.2 Control objectives and conventional strategies

Modern wind turbines are commonly designed to operate for 20 years or longer [13], the time period in which the machines need to generate as much power as possible to maximize electricity generation profit. In addition, the turbines must endure persistent and intricate mechanical stresses to prevent early decommissioning due to damages induced by various and continuous loads posed by the wind. These two objectives are the primary ones for wind turbine control systems. In several regions in the world where wind energy resource is abundant and wind power penetration is high, transmission system operators impose additional requirements for wind turbines, being the capabilities to provide power generation-load balance of the grid. This is known as the grid ancillary services. Being machines with various moving and interacting components, wind turbines emit acoustic noise during their operation. From the environmental impact perspective, certain noise may not be desirable and affect public acceptance of wind turbines. Being able to control the noise level of the turbines, at least to an extent, is thus desirable. These last two requirements form the secondary control objectives of wind turbines.

Different control strategies to satisfy the above-mentioned objectives are needed depending on the wind turbine's operational mode. These modes are based on whether the turbine rotational speed can be varied by manipulation of generator torque (*fixed- or variable-speed*) and if the blade is pitchable to manipulate the aerodynamic torque (*fixed- or*

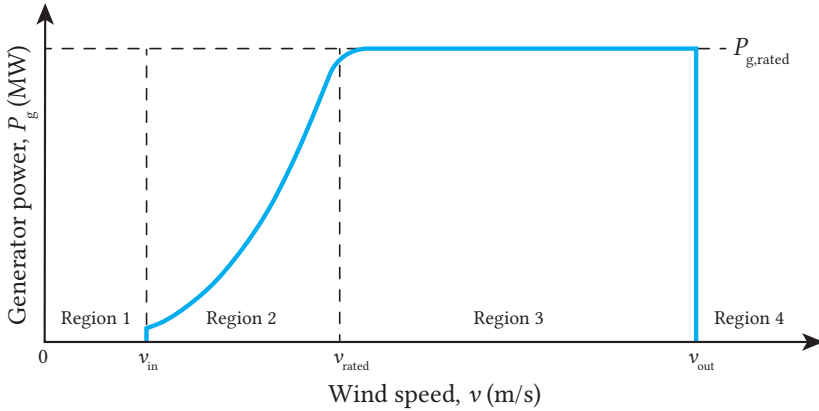


Figure 1.3: A typical wind turbine power curve. The blue line shows the change in the generator power P_g for four different regions, determined by the cut-in wind speed v_{in} , rated wind speed v_{rated} , and cut-out wind speed v_{out} . In Region 2, the wind turbine maximizes power capture from the wind, whereas in Region 3, the power regulation mechanism comes into play to maintain generator power at its rated value $P_g = P_{g,rated}$. In Regions 1 and 4, no power is produced due to economic and safety considerations.

variable-pitch) [15, 22, 23]. The majority of modern wind turbines employ variable-speed, variable-pitch (VS-VP) configuration as it allows for overall better power extraction, speed regulation, and mechanical load reduction compared to the other configurations. In the following subsections, these objectives and how they are attained under the VS-VP configuration are explained in more detail.

Objective 1: Power production optimization

The following relation determines the power contained in the wind

$$P_w(t) = \frac{1}{2} \rho \pi R^2 v(t)^3, \quad (1.1)$$

with ρ , R , and v as the air density, rotor radius, and wind speed, respectively. Not the entire wind power above can be harnessed into aerodynamic power. The aerodynamic power, defined as

$$P_a(t) = P_w(t) C_p(\beta(t), \lambda(t)), \quad (1.2)$$

is limited by the power coefficient function $C_p < C_{p,Betz}$, being a function of the pitch angle β and tip speed ratio (TSR) $\lambda = \omega_r R / v$ with ω_r as the rotor angular speed. For a wind turbine, its C_p function can be found numerically by using blade element momentum theory. The constant $C_{p,Betz} = 16/27 \approx 0.59$ is known as the Betz limit, which is the theoretical maximum efficiency of a wind turbine [13].

The power production profile of a wind turbine for a range of wind speeds is commonly presented in a ‘power curve’ such as exemplified in Figure 1.3. This power curve is sliced into multiple regions by the cut-in (v_{in}), rated (v_{rated}), and cut-out (v_{out}) wind speeds indicating distinguished power production objectives of the turbine as follows

- **Region 1 (idle)** - $v < v_{in}$: In this region, the power production objective of the wind turbine is not to generate any power; thus, the turbine is set to idle. This is because

the wind speed is not sufficiently high to overcome losses in the turbine system, not to mention only little to no economic profit can be gained from such low wind speeds. By pitching the blade at the ‘feather’/parked position, nominally at $\beta = 90^\circ$, the aerodynamic torque is minimized such that the rotor is prevented from spinning.

- **Region 2 (below-rated/partial load)** - $v_{in} \leq v < v_{rated}$: Within this wind speed range, the main objective is to harness as much power as possible from the wind by ensuring that the maximum power coefficient $C_p = C_p^*$ is always reached. The maximum power tracking can be achieved by setting the optimal generator torque demand T_g^* based on generator speed measurements $\omega_g = G\omega_r$, with G as the gearbox ratio, determined by the following relation

$$T_g^*(t) = \frac{\rho\pi R^5 C_p^*}{2G^3 \lambda^{*3}} \omega_g(t)^2, \quad (1.3)$$

known as the K -omega-squared control law [13, 24], where K is a constant, optimal gain. The notation λ^* in (1.3) indicates the design TSR of the turbine. At this point, the blade pitch is set to the ‘fine’ position, which, in combination with $\lambda = \lambda^*$, allows for the maximum aerodynamic power to be captured.

- **Region 3 (above-rated/full load)** - $v_{rated} \leq v \leq v_{out}$: After the wind speed reaches v_{rated} , the generated power may become larger than what the generator is capable of producing. Thus, the power production objective switches from power maximization to power regulation at the rated capacity. To this end, the blades are collectively pitched such that the aerodynamic power is lowered to keep constant rotational speed, which, in turn, limits the generated power. Simultaneously, structural loads are also mitigated by the reduction in the rotor thrust force; thus, the multiple roles the collective blade pitching serves in this region. Due to the varying blade aerodynamic sensitivity with respect to the pitch angle, a gain-scheduled control strategy is often employed to ensure equal dynamic performance for the entire Region 3 [25]. With regard to generator torque control in this region, either constant torque or constant power strategy can be applied, where the former is mainly beneficial for floating offshore wind turbines, whereas the latter is commonly preferred for onshore turbines [25–27].
- **Region 4 (shut down)** - $v > v_{out}$: When the wind speed becomes higher than the cut-out, it is deemed unsafe to operate the turbine as mechanical loads are very high at this point. Furthermore, wind speeds at this regime do not frequently occur; thus, the economic value of operating here is very low. Therefore, the wind turbine is shut down by pitching the blades toward the feathered position and no power is produced.

Apart from the aforementioned regions, note that in some literature, e.g. [25, 28], a transition between Region 1 and 2, namely Region 1.5, is also included in such a power curve for wind turbine start-up purposes. For the sake of brevity, this region is omitted from this thesis and the interested reader is referred to the literature for more details.

Objective 2: Structural load mitigation

Having moving mechanical structures, wind turbines experience an ample amount of structural loading. Therefore, in conjunction with the power production objectives previously discussed, structural load mitigation objectives must also be taken into account to ensure the safe operation of the wind turbines until their designated end-of-life and preferably longer. In the following, the load mitigation aspect of several wind turbine key components are listed.

- **Tower load:** Generally, wind turbine towers are not well-damped and are easily excited by wind excitations, both in the fore-aft and side-side directions. As a tower makes up a large portion of a wind turbine capital expenditure [29], alleviation of its fatigue loads becomes one of the highly prioritized control objectives. To this end, an active load control method is designed by scaling the integrated tower-top acceleration measurements with a gain negatively proportional to the tower-top velocity. This way, the effective tower damping is increased such that the tower becomes more resistant to fatigue loading resulting from wind excitations. For the fore-aft tower control, the collective pitch is actuated to provide the additional damping [30, 31]. On the other hand, in the case of side-side tower motion, either generator torque [31, 32] or individual pitching [33, 34] can be chosen as the actuation method. The former actuator, however, is coupled with the power generation, and thus, influence on the power quality is inevitable, while the latter costs more in terms of increased wear and tear of the pitch mechanism.

Apart from the conventional active tower damping above, an additional tower load mitigation strategy might need to be incorporated depending on the tower type. A wind turbine tower type is categorized based on the relation between its natural frequency and frequencies of excitation, commonly being the rotational frequency (1P) and blade-passing frequency (3P, for a three-bladed wind turbine) [13, 35]. As illustrated in Figure 1.4, a *stiff-stiff* tower has its natural frequency beyond the blade-passing frequency; that of a *soft-stiff* design has its natural frequency between the 1P and the blade-passing frequency (indicated by a gray arrow in the figure); and for a *soft-soft* tower, its natural frequency is located lower than the rotational frequency. Being the strongest, the stiff-stiff tower type is rather uneconomical to construct due to the extra mass/material required. On the contrary, the soft-soft type is more affordable but more easily excited by low-frequency loads, such as waves for offshore installation. To reconcile both the strength and affordability requirements, wind turbine engineers often resort to soft-stiff designs.

Nevertheless, conventional upscaling, as mentioned in Section 1.1, may reach a bottleneck for soft-stiff towers as their economic benefit diminishes by the excessive materials used as a result of the scaling. For onshore wind turbines, inland transportability constraints, which vary from country to country, may limit the extent to which the tower base diameter could be upscaled [14]. Their offshore counterparts, especially those with power ratings larger than 5 MW and fixed-bottom foundations in deep waters, face significant challenges in meeting the demanding requirements for monopile diameters and tower wall thicknesses to maintain soft-stiff character-

istics [35]. Thus, further compromise is taken by relocating the tower's natural frequency within the rotor operating range³, as illustrated by a red arrow in Figure 1.4, for instance, by reducing tower wall thicknesses [14]. A clear consequence of this design is the increased chance of tower resonance by excitation of the rotor frequency, thereby creating severe fatigue loading, which can be exacerbated if a more intensive 1P loading is present due to an imbalance in the rotor. Such an imbalance may arise from the aerodynamics (for instance, by non-aligned blade pitch positions or degradation in the blade profile) or accumulation of extra masses (such as from dirt, moisture, or ice) [36, 37].

Although the conventional active control method is available, such as by scaling of the integrated tower-top acceleration stated above, this challenging situation is often addressed using a passive control technique, namely the *frequency skipping* by *speed exclusion zone* application [15, 35, 38]. To this end, the generator torque demand is manipulated so that the rotor accelerates or decelerates near the tower's natural frequency, depending on whether the rotational speed is lower or higher than the critical frequency. This passive strategy enables reduced tower fatigue load as it becomes less frequently excited by the 1P frequency, resulting from the shortened duration of rotor operation about the resonance frequency.

- **Blade load:** Wind turbine blades slice through a complex, three-dimensional, and time-varying wind field structure as they rotate. This structure is made up of local variations in wind speed (turbulence), increasing wind speed as height increases (wind shear), wind speed deficit at the tower (tower shadow), and yaw misalignment discussed earlier in Section 1.2.1. As the blades become longer and more flexible due to the upscaling, there is a greater impact in terms of asymmetric loading from such spatiotemporal variability in the wind. Mainly, this is observed as an increase in the spectral components of the blade out-of-plane moments at the 1P frequency and its higher harmonics (at 2P, 3P, and so forth), measured in the rotating frame. By the fixed structure (or reference frame) these periodic loads are sensed as the 0P (static component), 3P, 6P, and so on, in the case of three-bladed wind turbines.

As wind turbines nowadays are widely equipped with individual pitch actuators, it is possible to make amends to the rise in periodic blade moments aforementioned by controlling the blade pitch positions independently, known as individual pitch control (IPC). The conventional approach for IPC [30] utilizes the projection of the blade load measurements from the rotating into the orthogonal tilt and yaw axes in the nonrotating reference frame through an azimuth-dependent Coleman transformation [39]. Subsequently, two identical single-input single-output (SISO) controllers are designed onto these axes, from which the tilt and yaw pitch control actions are generated. Both pitch signals are transformed back into the rotating frame by an inverse transformation, resulting in three individual pitch angles, being 120° out of phase from each other. A phase offset inclusion to the inverse transformation is

³Due to the lack of definition in the literature (and for convenience's sake), in some of the following chapters, the term soft-soft is also used to refer to towers with their first natural frequency within the 1P range.

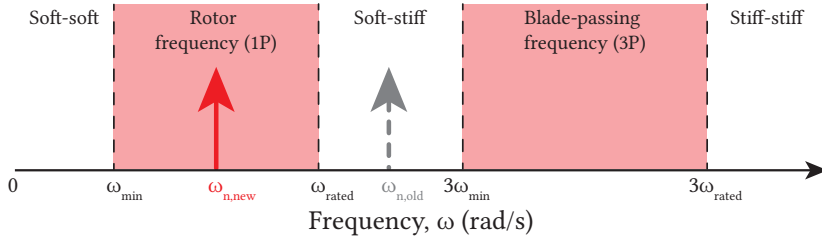


Figure 1.4: Wind turbine tower categorization based on its natural frequency location relative to the rotor frequency (1P) and blade-passing frequency (3P, for a three-bladed turbine) ranges. A soft-soft wind turbine has its natural frequency below the 1P frequency range (indicated by the minimum and rated speeds ω_{\min} and ω_{rated}), soft-stiff between the 1P and 3P frequency ranges, and stiff-stiff beyond the 3P range. A typical tower has its natural frequency in the soft-stiff regime, as shown by the gray line at $\omega_{n,\text{old}}$. A compromise between increasing cost associated with a greater mass of large towers and strength requirements motivates designs with natural frequency relocated into the 1P range, as exemplified by the red arrow at $\omega_{n,\text{new}}$.

often considered in the literature, e.g. [16, 30, 40], to ensure that the two nonrotating axes are fully decoupled. Such a dynamic coupling is often the case for modern turbines, especially those with elongated, non-rigid blades; thus, the phase offset inclusion becomes indispensable for the SISO control design to be justified. In some literature, this scheme is also recognized as a *modulation-demodulation* scheme, such as in [41].

- **Drivetrain torsional mode:** A wind turbine drivetrain system may be modeled as two rotating masses, each representing the rotor and the generator, interconnected by a torsional spring and a torsional damper [42]. Although in several wind turbine designs their drivetrain torsional mode is well-damped by appropriate rubber mount or coupling designs, other designs might exhibit otherwise [26]. Low torsional mode damping can exhibit undesirable and considerable torque variations at the gearbox, which may also affect the generated power quality. A conventional method to improve the damping of this mode is to create an additive generator torque demand by band-pass filtering the generator speed measurements at the natural frequency of the torsional mode [26].

Objective 3: Grid ancillary services

Apart from the aforementioned objectives, wind turbines nowadays are expected to partake in reducing the imbalances between power generation and load/consumption sides of the utility grid. Another expectation imposed on wind turbines is their responsiveness to grid frequency fluctuations so as to prevent grid instability. These two additional objectives fall under the grid ancillary services aspect of wind turbine operation, which can be provided by wind turbines using the so-called active power control (APC) [43].

APC is done by down-regulating a wind turbine or wind farm, that is, tracking power set points commanded by the transmission system operator, which is lower than the currently available wind power. Several APC schemes have been investigated in the literature, for instance, derating, delta reserve, and percentage reserve [44]. In the derating scheme,

maximum power output is controlled by reducing the rated generator torque with constant rated rotor speed [43]; delta reserve maintains an unchanged aerodynamic power in reserve [45]; and percentage reserve captures a portion of the maximum available power over the entire range of operational wind speed [46]. The interested reader is referred to the literature for further elaboration with regard to these methods.

Objective 4: Acoustic noise reduction

With various moving and interacting components, wind turbines emit acoustic noise. The blades' tip speed is one of the most dominant acoustic noise sources such that an upper limit to this speed is commonly imposed. This limit also implies that a limitation on the rotor speed is necessary for a given rotor radius. Accordingly, the control systems for Regions 2 and 3 need to consider such a speed limit in their design. Furthermore, it requires an additional buffer zone between these regions, namely Region 2.5, capable of obtaining rated power production while satisfying the rotor speed constraint. [26, 47].

1.3 State-of-the-art and challenges

From the control system design perspective, a wind turbine is a complex, multivariable system with various degrees of dynamic coupling between its components. It is also a system whose operation must adhere to several constraints, such as actuator limitations, acceptable structural loads, power production and quality constraints, and so forth. In addition, meeting a number of control objectives, as stated in the previous section, is far from trivial, as multiple trade-offs exist such that satisfying one objective without sacrificing another is not always possible. The employment of a control paradigm capable of taking into account multivariable systems, respecting the system constraints, and capable of conveniently tuning the trade-off of multiple control objectives thus becomes necessary. A viable candidate to meet these needs is the model predictive control (MPC).

MPC is a model-based control technique that optimizes a system's inputs to achieve control objectives over a finite prediction horizon in the future while directly accounting for the system's constraints [48]. The first elements of the optimal input sequence are applied to the system, after which the system's information via measured outputs and/or estimated unknown states are supplied into the MPC to enable the next optimization routine with a one-step forward shift of the horizon. This controller type can be categorized into two: tracking MPC (TMPC) and economic MPC (EMPC). TMPC is designed to control a system to track steady-state references, embodied in the optimization's objective function. Although a large body of literature has been dedicated to exploring the potential of TMPC, the connection between the tracking objective and the economic performance of a system's operation is less than straightforward. This has motivated the development of EMPC, which minimizes (or maximizes) directly the system's economic performance indicator by integrating it into its objective function. Moreover, as the system does not need to track steady-state references, better performance during transient with respect to TMPC is expected [49] and more convenient trade-off tuning between economic objectives is possible.

In MPC, the arrangement of its objective function (to be minimized or maximized), system dynamics, and constraints, known as the optimal control problem (OCP), determines whether the optimization can be solved effectively. A contributing factor to this is

the OCP's convexity since it does not have local minima (or maxima), i.e., only a global minimum (or maximum) exists. From the numerical perspective, having such a property in an OCP is highly desirable as effective methods to solve it are available and require much less computational load than a non-convex OCP. Additionally, as no global optimality can be guaranteed for non-convex OCPs, the risk of converging to a local minimum is ever-present [50].

A particular form of EMPC possessing such a convex OCP is termed *convex EMPC* (CEMPC) and has been garnering attention lately, in particular since the advent of the work of [51]. In the study, an MPC framework is designed to satisfy wind turbines' power gradient requirements dictated by a grid code. The key to the establishment of the OCP convexity in this framework lies in a variable transformation, replacing nominal wind turbine rotational speed, blade pitch, generator torque, and wind speed signals into kinetic energy and power terms. The generated control input is thus globally optimal based on the known measurement/estimation information received by the controller. An extension, accounting for fatigue loading of the fore-aft tower motion, was studied later on by different authors [52], which also employs an adaptive feature to improve power production despite model-plant mismatches. However, side-side tower motion, despite being known to have approximately one order of magnitude lower damping than the fore-aft [13], has not yet been taken into account in this framework. Thus, the following challenge in the development of CEMPC by variable transformation in power and energy terms is posed.

Challenge 1: Enhance the tower load mitigation capability of the CEMPC framework by the inclusion of a side-side tower load mitigation aspect.

Additionally, in the same CEMPC framework, load reduction aspects of the blades, being also wind turbine key components, have not received any attention. The 1P periodic loading experienced by each blade is commonly tackled by an individual pitching mechanism, given the information of the loading from the load sensors. The next challenge is thus to incorporate such a mechanism in the CEMPC framework as follows.

Challenge 2: Enable blade load mitigation capabilities of the CEMPC framework by the inclusion of an individual blade pitching mechanism.

Other than the previously mentioned framework of [51], another novel CEMPC method has also been introduced in the literature with the original aim of preventing a soft-soft tower resonance in the side-side direction [53]. This work was motivated by the shortcomings of the conventional frequency-skipping method (see Section 1.2.2), being the intricacies of the additional logic that needs to be incorporated. Additionally, whether the resulting control solution is dynamically optimal is unknown. Nevertheless, this is not the case in the work of [53], which is shown to exploit the advantages of EMPC, especially its capability to optimize both objectives directly in the controller formulation while accommodating an optimal trade-off between them. This work incorporates a quasi-linear parameter varying (qLPV) model formulation, resulting from augmenting drivetrain dynamics with an alternative representation of tower dynamics. The key to obtaining the

alternative tower dynamics here is the application of a *model demodulation transformation*, brought from the field of mechatronics [54] to a nominal second-order approximation of a tower flexural mode. This transformation enables the decoupling of the slow-varying components of the signals from their fast-varying counterparts. The convex OCP that follows owes to the obtained affine qLPV dynamics; moreover, the economic control objectives can be directly accounted for. As a result, the qLPV-MPC algorithm, adopted from [55], prevents prolonged operation of the turbine about the tower's natural frequency by the dynamic and optimal frequency skipping behavior it exhibits.

Regardless of the effectiveness of the aforementioned qLPV-MPC framework, the periodic loading is still not dealt with in an active manner; that is, the disturbance is not actively canceled by the control action. Therefore, in order to incorporate active tower load cancellation, an estimation scheme of the unknown periodic load arising from the mass imbalance at the rotor needs to be established. Furthermore, as the model demodulation transformation has enabled the controller framework, employing this transformation scheme for the load estimation purpose may provide a cohesive controller-estimator scheme. By incorporating the periodic load estimation scheme into the qLPV-MPC algorithm, the controller is expected to exhibit frequency skipping while canceling the effect of the periodic load simultaneously, resulting in better tower fatigue load reduction. Hence, the next challenge posed in this thesis is as follows.

Challenge 3: Design an unknown periodic tower load estimation scheme utilizing a model demodulation transformation as a step toward a qLPV-MPC framework with an active periodic load cancellation capability.

Although designing an improved qLPV-MPC implementation incorporating periodic load cancellation may be possible after the unknown load estimation scheme is ready, not even a conventional method exists yet for active cancellation of such load, to the author's knowledge. For instance, modulation-demodulation control (MDC) schemes have been widely used in mechatronics and other areas (see [56–58] and references therein). Such schemes leverage a coordinate transformation to project periodic signals to steady-state, where straightforward linear time-invariant (LTI) controllers can be designed, and cancel the periodic disturbances. Therefore, the last research challenge in this thesis is posed.

Challenge 4: Design a side-side tower load mitigation control scheme for actively canceling a periodic load based on MDC techniques.

1.4 Thesis objective and contributions

CEMPC has been gaining more and more attention in the wind turbine control community due to the direct relation of the OCPs' objective function with the actual economic objectives of the wind turbine operation. The convexity of the OCP ensures the global optimality of the solution, which is also advantageous from the numerical vantage point. However, a lack of attention is given to the exploitation of the power-and-energy CEMPC

framework, the convexity of which is achieved by a variable transformation in power and energy terms, in that its potential to mitigate the loads of the side-side tower motion and the blades has been overlooked. On the other hand, the qLPV-MPC was developed for the purpose of passive tower resonance prevention in the presence of a 1P periodic loading, showcasing the potential of a demodulation (transformation) technique in rendering its convexity. Nevertheless, for an active periodic load cancellation to be incorporated into the framework, an unknown periodic disturbance estimation scheme is a missing puzzle piece to achieve this feature. Interestingly, a conventional control method specifically targeting the 1P load cancellation of the side-side tower motion is currently unknown in the academic literature despite the availability of modulation-demodulation control to serve this purpose. Therefore, an exploration into active periodic load cancellation in a conventional manner can help in understanding how such a mechanism would work later if such a feature exists in a CEMPC framework. Furthermore, the two separate CEMPC frameworks have the potential to be crossed, resulting in a unified CEMPC framework capable of addressing the structural loads of multiple wind turbine components. Hence, the following thesis objective is formulated based on the stated motivations.

Thesis objective: Establish a unified CEMPC framework capable of simultaneously optimizing operational performance with structural load mitigations.

The first step toward achieving the objective above is expanding the load mitigation capability of the CEMPC framework of [51], in which power and energy variables are used in place of nominal wind turbine variables to obtain the convexity of its optimization problem. Tower fatigue load reduction is a crucial objective in a control system design with only the fore-aft direction of the motion being addressed in this framework [52]. The inclusion of side-side tower load mitigation objective into this CEMPC framework is thus the next step required to complete the tower load mitigation aspect of this framework and, thereby, forms the first contribution of this thesis:

Contribution 1: Develop an enhancement of the CEMPC framework by incorporation of a side-side tower load mitigation aspect.

After fully integrating fore-aft and side-side tower fatigue loads into the aforementioned CEMPC framework, the next step is to address the fatigue loads of other key wind turbine components. In particular, the potential of the blade loads mitigation facet of the CEMPC scheme has not yet been explored in the literature. Thus, the next contribution of this thesis is to address this knowledge gap:

Contribution 2: Integrate a blade loads mitigation feature within the CEMPC framework by exploiting the individual pitch capabilities of modern turbines.

One of the challenges in modern wind turbine control where a tall, slender, soft-soft tower is used is the presence of the tower's natural frequency within the operating range

of the turbine. In the literature, the dynamic frequency skipping by qLPV-MPC [53] has been introduced, the convexity of which is made possible by the employment of a model demodulation transformation. As the side-side periodic load in this framework is only dealt with passively, an active control capability of this framework might be worth exploring. This requires an unknown periodic load estimation scheme to be first developed so that the qLPV-MPC algorithm can be supplied with the crucial load information. Since this load is unknown, an estimation method needs to be developed to supply this algorithm with the unknown periodic load. This forms the third contribution of this thesis:

Contribution 3: Develop an unknown periodic side-side tower load estimation method utilizing a model demodulation transformation.

With regard to conventional periodic side-side tower load mitigation for tower resonance prevention, only passive, frequency-skipping methods are available. While conventional periodic load mitigation has been developed for blade loads mitigation purposes, employing a modulation-demodulation control scheme, that of side-side tower load has not yet been addressed in a similar manner. Therefore, the final contribution of this thesis is:

Contribution 4: Provide an active side-side tower load cancellation method by means of a modulation-demodulation control approach.

1.5 Thesis organization

This thesis contains six chapters, with the first one being the current introduction chapter. The subsequent four chapters are practically duplicates of scientific publications by the author of this thesis with co-authors. These chapters showcase the contributions of this work in the same order as mentioned in the previous chapter.

Chapter 2 is dedicated to developing a CEMPC framework for side-side tower load mitigation by individual pitching. The chapter is based on the following publication:

A.K. Pamososuryo, Y. Liu, T.G. Hovgaard, R.M.G. Ferrari, J.W. van Wingerden. Individual pitch control by convex economic model predictive control for wind turbine side-side tower load alleviation. In *The Science of Making Torque from Wind (TORQUE)*, Delft, Netherlands, 2022.

In **Chapter 3**, the development of a CEMPC framework for blade loads mitigation by individual pitching is explained. The chapter is based on the following publication:

A.K. Pamososuryo, Y. Liu, T.G. Hovgaard, R.M.G. Ferrari, J.W. van Wingerden. Convex economic model predictive control for blade loads mitigation on wind turbines. *Wind Energy* 26 (12), 1276-1298, 2023.

Then, in **Chapter 4**, the development of periodic load estimation using a model demodulation transformation is given. The chapter is based on the following publication:

A.K. Pamososuryo, S.P. Mulders, R.M.G. Ferrari, J.W. van Wingerden. Periodic load estimation of a wind turbine tower using a model demodulation transformation. In *American Control Conference (ACC)*, Atlanta, Georgia, USA, 2022.

Chapter 5 lays out the development of periodic side-side tower load cancellation by a modulation-demodulation control approach. The chapter is based on the following publication:

A.K. Pamososuryo, S.P. Mulders, R.M.G. Ferrari, J.W. van Wingerden. On the analysis and synthesis of wind turbine side-side tower load control via demodulation. *IEEE Transaction in Control Systems Technology*, 2024.

Finally, in **Chapter 6**, the main conclusions of this thesis are drawn and recommendations for future research are provided. The structure of this thesis is shown in Figure 1.5.

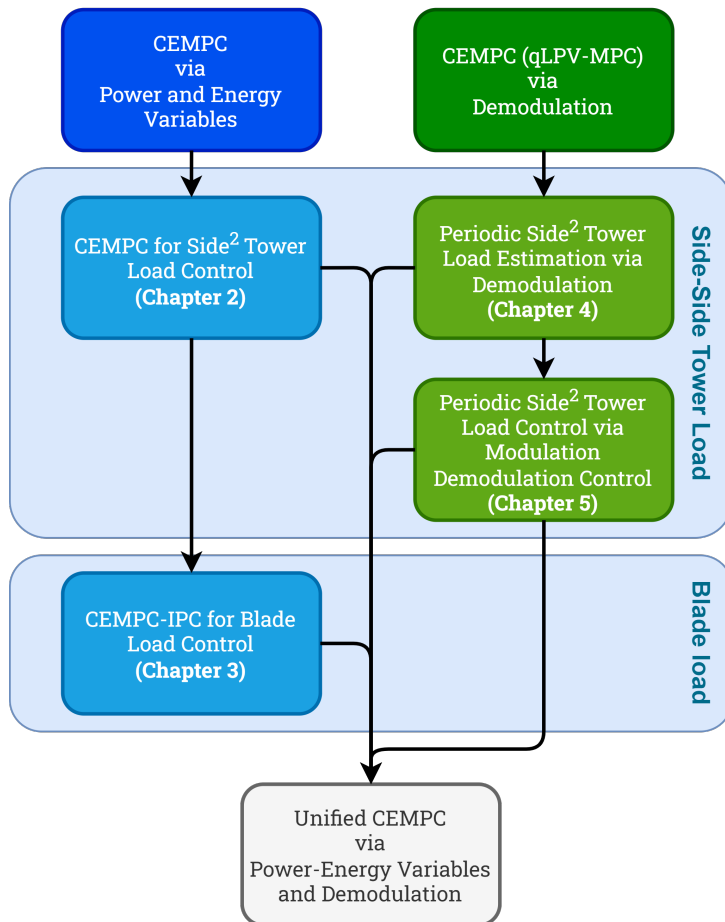


Figure 1.5: The organization of this thesis, along with the envisioned end objective (gray box).

2

2

Individual Pitch Control by Convex Economic Model Predictive Control for Wind Turbine Side-Side Tower Load Alleviation

The wind turbine side-side tower motion is known to be lightly damped. One viable active damping solution is realized by deploying individual pitch control (IPC) such that counter-acting blade forces are created to alleviate the tower fatigue loading caused by this motion. Existing IPC methods for side-side tower damping in the literature, such as linear quadratic regulators and lead-lag controllers, cannot accommodate direct optimization and trade-off tunings of the wind turbine economic performance. In this work, a novel side-side tower damping IPC strategy under a convex economic model predictive control (CEMPC) framework is therefore developed to address these challenges. The main idea of the framework lies in the variable transformation in power and energy terms to obtain linear dynamics and convex constraints, over which the economic performance of the wind turbine is maximized with a globally optimal solution in a receding horizon manner. The effectiveness of the proposed method is showcased in a high-fidelity simulation environment under both steady and turbulent wind cases. Lower fatigue damage on the side-side tower bending moment is attained with an acceptable level of pitch activities, negligible impact on the blade loads, and minor improvement on the power production.

2.1 Introduction

Wind turbines are manufactured in record-breaking sizes to further decrease the leveled cost of energy by harnessing more power from the wind [59]. As wind turbine towers become ever taller, their wall thickness is typically decreased to maintain the cost of energy low, which consequently aggravates the fatigue loadings due to the increased structural flexibility [14]. From the control engineering perspective, this implies that load mitigation objectives are of even higher importance to ensure prolonged wind turbine operation—urging advanced control methods to be deployed.

Among the most prominent loads is that of the side-side tower since it is lightly damped. In addition, only negligible effects of the so-called aerodynamic damping are experienced, in contrast to the fore-aft motion [60]. In recent years, the most common control strategy used to mitigate prolonged side-side tower oscillation is the active damping by generator torque, such as the work done by Mulders, et al. [53] and references therein. Although proven to be effective, power production can be affected as a side product of the load reduction activity, as demonstrated by Mulders, et al.

Alternatively, one may resort to the individual pitch control (IPC) to manipulate the blade in-plane forces' horizontal component; resulting in the side-side tower-top force counteracting the structural excitation [34]. The literature shows that the industry has been adopting this approach since nearly two decades ago [61]. Several academic studies emerged afterward, for instance, the work of Stol, et al. [33], which incorporates a linear quadratic regulation approach and Duckwitz and Geyler [34], where a conventional lead-lag controller was designed. These methods, however, do not accommodate direct optimization and trade-off tunings of the wind turbine economic performance, such as power capture maximization, structural fatigue mitigation, and actuator activities penalization.

One of the state-of-the-art control methods capable of handling such requirements is the economic model predictive control (EMPC) [51, 52, 62]. EMPC operates by generating control inputs to maximize a system's economic performance formalized in the so-called optimal control problem (OCP) up to certain time steps in the future in a receding horizon manner. In wind turbine applications, however, EMPC often suffers from nonlinearities, such as those coming from the aerodynamics. This renders the OCP harder to solve, not to mention that a globally optimal solution cannot be guaranteed. To address these challenges, a novel convex economic model predictive control (CEMPC) strategy has been developed by Hovgaard, et al. [51] with the main goal to enable smooth power delivery to the grid. In this work, a power-and-energy-based variable transformation is conducted to allow linear dynamics and convex constraints to be incorporated into the CEMPC. Shaltout, et al. [52] have successfully integrated tower fore-aft damping objective into the framework and thereby exhibit the applicability of CEMPC for load mitigation. Unfortunately, to the best of our knowledge, the side-side tower load mitigation and individual pitching potentials of this framework have received little to no attention in the literature.

Therefore, our main focus in this study was to formulate an extension to the CEMPC framework of Hovgaard, et al. [51], accounting for the aforementioned side-side tower fatigue load reduction by means of IPC. In detail, this extension is made possible by augmenting a second-order wind turbine tower model with the tower-top force formulated in terms of aerodynamic powers and rotational kinetic energy to obtain linear tower dynamics.

The remainder of this chapter proceeds as follows. In Section 2.2, the nominal wind turbine model is introduced, which is then reformulated in power and energy terms in Section 2.3. Section 2.4 elaborates on the CEMPC implementation, including the OCP design and a brief discussion regarding the complementary state estimators. Simulation results and discussions are provided in Section 2.5. In Section 2.6, the conclusions of this work are given.

2.2 Nominal Wind Turbine Model

This section presents the derivation of the nominal wind turbine dynamical model comprised of the drivetrain and the side-side tower motion. To model the drivetrain dynamics, a one-mass model torque balance equation in continuous time t is employed as follows

$$J_{\text{hss}} \dot{\omega}_{\text{g}}(t) = T_{\text{r}}(t)/G - T_{\text{g}}(t), \quad (2.1)$$

with the high-speed shaft equivalent inertia denoted by J_{hss} and the gearbox ratio by G . The generator speed ω_{g} and the generator torque T_{g} are operated within the following limits

$$\omega_{\text{g},\text{min}} \leq \omega_{\text{g}}(t) \leq \omega_{\text{g},\text{max}}, \quad (2.2)$$

$$0 \leq T_{\text{g}}(t) \leq T_{\text{g},\text{max}}, \quad (2.3)$$

where the subscripts ‘min’ and ‘max’ indicate the lower and upper bounds of the specified quantities.

The rotor aerodynamic torque T_{r} in (2.1) is defined as the total torque contribution of the individual blades [34, 63] as shown below

$$T_{\text{r}}(t) = \sum_{i=1}^B T_{\text{r},i}(t), \quad (2.4)$$

where i is the blade index and $B = 3$ is the number of blades of the wind turbine under study. The individual blade aerodynamic torque $T_{\text{r},i}$ is related to the individual aerodynamic power $P_{\text{r},i}$ by the following expression

$$T_{\text{r},i}(t) = P_{\text{r},i}(t)/\omega_{\text{r}}(t), \quad (2.5)$$

in which

$$P_{\text{r},i}(t) = (1/(2B))\rho AC_{\text{p}}(\beta_i(t), \lambda_i(t))v_i(t)^3, \quad (2.6)$$

where ρ and A are the air density and the rotor area, respectively. The power coefficient C_{p} is a function of the individual pitch angle β_i , limited under the following bounds

$$\beta_{\text{min}} \leq \beta_i(t) \leq \beta_{\text{max}}, \quad i \in \{1, 2, 3\}, \quad (2.7)$$

and the tip-speed ratio $\lambda_i(t) = \omega_{\text{r}}(t)R/v_i(t)$, with $\omega_{\text{r}}(t) = \omega_{\text{g}}(t)/G$ as the rotor speed, R as the rotor radius, and v_i as the blade-effective wind speed. This power coefficient is often represented as a look-up table whose values can be derived either numerical- or empirically.

At the generator side of the drivetrain, the generated power is obtained as the product of the generator speed and torque, taking into account the efficiency factor $\eta_g \in [0, 1]$, as follows

$$P_g(t) = \eta_g \omega_g(t) T_g(t), \quad (2.8)$$

which is restricted by the constraints

$$0 \leq P_g(t) \leq P_{g,\max}. \quad (2.9)$$

To model the support structure, a second-order cantilever beam is employed to approximate the wind turbine side-side tower dynamics, where an acting force on its top is considered

$$M\ddot{x}_{ss}(t) + D\dot{x}_{ss}(t) + Kx_{ss}(t) = F_{ss}(t). \quad (2.10)$$

The quantities \ddot{x}_{ss} , \dot{x}_{ss} , and x_{ss} in the above equation refer to the tower acceleration, velocity, and displacement, respectively, and the symbols M , D , and K are designated as the first tower modal mass, damping, and stiffness coefficients. The side-side tower-top force F_{ss} is considered as the sum of its individual components $F_{ss,i}$, defined as the horizontal projection of the in-plane blade force $F_{ip,i}$. This mapping is formulated in the following equation

$$F_{ss}(t) = \sum_{i=1}^B F_{ss,i}(t) = \sum_{i=1}^B -F_{ip,i}(t) \cos(\psi_i(t)), \quad (2.11)$$

where the i -th blade azimuth position is denoted by $\psi_i(t) = \psi(t) + 2\pi(i-1)/3$ with $\psi(t) = \omega_r(t)t^1$ as the first blade azimuth position. The zero value of ψ is defined at its vertically upward position and increments in the clockwise direction as illustrated in Figure 2.1. Note that due to this convention, a negative sign precedes $F_{ip,i}$ in (2.11) due to the sign difference between the side-side force and the tower motion.

The in-plane force acts perpendicularly to the corresponding blade at $s_c R$ distance away from the rotor center to produce the individual aerodynamic torque $T_{r,i}$, with $s_c = 1/2$ for a uniformly distributed force along the blade [63], formulated as

$$F_{ip,i}(t) = T_{r,i}(t)/s_c R. \quad (2.12)$$

Having the nominal model and constraints derived above, the following remarks are laid out. First, the aerodynamic power, defined in (2.6), is a nonlinear function of the state ω_g , control input β_i , and disturbance v_i , and appears in both the dynamics of the drivetrain in (2.1) and tower in (2.10). Moreover, the generated power output formulated in (2.8) is a bilinear function of the state ω_g and control input T_g . Thus, it can be inferred that the nominal wind turbine model possesses dynamics and constraints nonlinear/nonconvex in its variables, the former of which can be represented as the following nonlinear state-space

$$\begin{cases} \dot{\mathbf{x}}(t) = f(\mathbf{x}(t), \mathbf{u}(t), \mathbf{d}(t)) \\ \mathbf{y}(t) = g(\mathbf{x}(t), \mathbf{u}(t), \mathbf{d}(t)) \end{cases}. \quad (2.13)$$

The states, inputs, disturbances, and outputs of the above equation are $\mathbf{x}(t) = [\omega_g(t), \dot{x}_{ss}(t), x_{ss}(t)]^\top$, $\mathbf{u}(t) = [\beta_1(t), \beta_2(t), \beta_3(t), T_g(t)]^\top$, $\mathbf{d}(t) = [v_1(t), v_2(t), v_3(t)]^\top$,

¹Under the assumption of slowly-varying rotor speed as considered in Section 2.3 (in kinetic energy term).

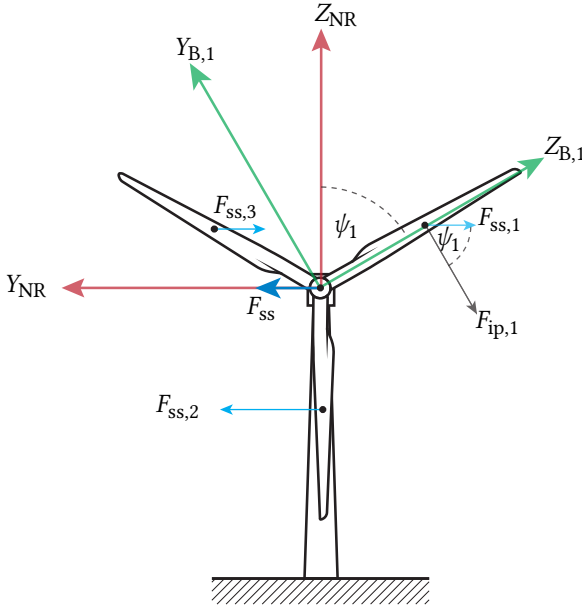


Figure 2.1: The in-plane force $F_{ip,i}$, only shown for the first blade, is perpendicular to the blade and acts at a $s_c R$ distance away from the rotor center. Its horizontal component $F_{ss,i}$ is mapped by the azimuth ψ_i , which is created by the angular difference between the non-rotating (red arrows) and rotating (green arrows) reference systems. The side-side force F_{ss} , resulting from the summation of the individual horizontal blade forces, is shown to act on the tower top.

and $\mathbf{y}(t) = [\omega_g(t), P_g(t), \ddot{x}_{ss}(t)]^\top$, respectively. Such nonlinear-/nonconvexity will pose additional challenges to model predictive control designs. One possible solution to tackle such an issue is by reformulating the dynamics and constraints linear/convex in their variable, e.g., by linearization. Alternatively, one may present a different set of variables such that the dynamics and constraints are linear/convex. The latter approach is taken into account in this work and treated in the next section.

2.3 Transformed Wind Turbine Model

In the model predictive control design of Hovgaard, et al. [51], the nonlinearity/nonconvexity issues of incorporating the nominal wind turbine dynamics are tackled by introducing the following variable transformations:

$$\begin{cases} \mathbf{x}(t) = [\omega_g(t), \dot{x}_{ss}(t), x_{ss}(t)]^\top \\ \mathbf{u}(t) = [\beta_1(t), \beta_2(t), \beta_3(t), T_g(t)]^\top \\ \mathbf{d}(t) = [v_1(t), v_2(t), v_3(t)]^\top \\ \mathbf{y}(t) = [\omega_g(t), P_g(t), \ddot{x}_{ss}(t)]^\top \end{cases} \rightarrow \begin{cases} \mathbf{x}_t(t) = [K_g(t), \dot{x}_{ss}(t), x_{ss}(t)]^\top \\ \mathbf{u}_t(t) = [P_{r,1}(t), P_{r,2}(t), P_{r,3}(t), P_g(t)]^\top \\ \mathbf{d}_t(t) = [v_1(t), v_2(t), v_3(t)]^\top \\ \mathbf{y}_t(t) = [K_g(t), P_g(t), \ddot{x}_{ss}(t)]^\top \end{cases}, \quad (2.14)$$

where power and energy terms are used, such that linear dynamics and convex constraints are obtained. The derivation of these dynamics and constraints is presented below.

Here, $K_g(t) = (J_{\text{hss}}/2)\omega_g(t)^2$ is the rotational kinetic energy of the generator constrained by

$$(J_{\text{hss}}/2)\omega_{g,\min}^2 \leq K_g(t) \leq (J_{\text{hss}}/2)\omega_{g,\max}^2, \quad (2.15)$$

derived straightforwardly from (2.2). The rate-of-change (ROC) of K_g is obtained by taking its first time-derivative and yields the following linear dynamics, substituting that of the drivetrain

$$\dot{K}_g(t) = J_{\text{hss}}\dot{\omega}_g(t)\omega_g(t) = \left(\sum_{i=1}^B T_{r,i}(t)/G - T_g(t) \right) \omega_g(t) = \sum_{i=1}^B P_{r,i}(t) - P_g(t)/\eta_g, \quad (2.16)$$

which are linear in their inputs.

The aerodynamic power $P_{r,i}$ is constrained by

$$0 \leq P_{r,i}(t) \leq \hat{P}_{\text{av},i}(v_i(t), K_g(t)), \quad i = \{1, 2, 3\}, \quad (2.17)$$

with

$$\hat{P}_{\text{av},i}(v_i(t), K_g(t)) = \min\{a_1 K_g(t) + b_1, \dots, a_j K_g(t) + b_j\} v_i(t)^3, \quad (2.18)$$

as the piecewise linear (PWL) function approximation of the available power in the wind $P_{\text{av},i}(v_i(t), K_g(t)) = \max_{\beta_{\min} \leq \beta_i(t) \leq \beta_{\max}} (1/(2B))\rho A C_p(\beta_i(t), \lambda_i(t)) v_i(t)^3$, where a_m and b_m , with $m \in \{1, \dots, j\}$, are the PWL function coefficients. It is important to note that the pitch limits in (2.7), as well as the wind speed information v_i , are now embedded in the above constraints.

To express the generated power bounds convex in the new variables, the constraints in (2.9) are rewritten as follows [52]

$$0 \leq P_g(t) \leq \underbrace{\min\left(\eta_g \sqrt{2K_g(t)/J_{\text{hss}}} T_{g,\max}, P_{g,\text{rated}}\right)}_{P_{g,\max}}, \quad (2.19)$$

which is convex in P_g and concave in K_g .

Regarding the side-side tower dynamics, the tower-top force F_{ss} defined in (2.11) now needs to be reformulated as a function of the new variables. This is done firstly by substituting (2.5) into the in-plane force calculation (2.12) such that $F_{\text{ip},i}(t) = P_{r,i}(t)/s_c \omega_r(t)R$. With $\omega_r(t) = \sqrt{2K_g(t)/J_{\text{hss}}}/G$, further substituting $F_{\text{ip},i}$ into (2.11) results in the new expression for the side-side force as follows

$$F_{\text{ss}}(t) = \sum_{i=1}^B - \frac{P_{r,i}(t)}{s_c \left(\sqrt{2K_g(t)/J_{\text{hss}}}/G \right) R} \cos(\psi_i(t)). \quad (2.20)$$

It can be noticed directly that F_{ss} contains the $1/\sqrt{K_g}$ and $\cos(\psi_i)$ terms, which are nonconvex in K_g . These terms will result in nonlinear tower dynamics, causing the OCP harder to solve. Nonetheless, it can be assumed that ω_g varies slowly over time, such that K_g and ψ_i of the previous time instant, denoted \tilde{K}_g and $\tilde{\psi}_i$, are employed and do not act as

decision variables of the CEMPC. Based on this assumption, the nominal side-side tower model in (2.10) is thus altered into the following linear dynamics

$$M\ddot{x}_{ss}(t) + D\dot{x}_{ss}(t) + Kx_{ss}(t) = \sum_{i=1}^B \frac{-P_{r,i}(t)}{s_c \left(\sqrt{2\tilde{K}_g(t)/J_{hss}} / G \right) R} \cos(\tilde{\psi}_i(t)), \quad (2.21)$$

which finalizes the model transformation for the proposed control design.

2.4 Convex Economic Model Predictive Control Formulation

Model predictive controllers work by calculating an optimal input trajectory such that the objectives of the plant's operation up to a certain time horizon in the future are minimized/maximized under the OCP. The first element of the generated input sequence is then fed into the plant, after which a new optimization is conducted to generate the next time step's optimal input trajectory based on new measurements—a routine known as the “receding horizon”.

To formulate the objective function of the proposed CEMPC, the following requirements are considered: (i) maximize power production, (ii) alleviate structural loads, and (iii) maintain acceptable actuator activities. These requirements are thus formalized into the following economic objective function

$$\mathcal{J}_{\text{OCP}}(k) = w_1 P_g(k) + w_2 \sum_{i=1}^B \hat{P}_{\text{av},i}(v_i(k), K_g(k)) - w_3 K_{\text{slack}}(k)^2 - w_4 \sum_{i=1}^B \dot{P}_{r,i}(k)^2 - w_5 \dot{P}_g(k)^2 - w_6 \dot{x}_{ss}(k)^2, \quad (2.22)$$

which are convex in the new variables, where k denotes the discrete time notation and w_l , with $l \in \{1, \dots, 6\}$ being the weights on the six different objectives explained as follows. The first and second terms represent the objectives to maximize the generated power and the available aerodynamic power. The third term denotes the penalty on the rotor over-speeding with respect to the rated value by enforcing the following constraint

$$K_g(t) \leq (J_{hss}/2)\omega_{g,\text{rated}}^2 + K_{\text{slack}}(t), \quad \text{with} \quad K_{\text{slack}}(t) \geq 0. \quad (2.23)$$

The fourth and fifth terms are the ROC penalties on the aerodynamic powers and the generated power and are, respectively, translated as the blade pitch and generator torque ROCs penalization. To minimize the side-side tower fatigue load, the velocity of the tower motion is penalized in the sixth term, which determines the amount of individual pitch activities to create the side-side tower force.

With the formulated linear dynamics, convex constraints, and previously-described

objective function, the OCP of the CEMPC is now given by

$$\max_{\mathbf{u}_t(\cdot)} \sum_{k=0}^{N_p-1} \mathcal{J}_{\text{OCP}}(k), \quad (2.24a)$$

$$\text{s.t.} \quad \mathbf{x}_t(k+1) = \mathbf{A}_d \mathbf{x}_t(k) + \mathbf{B}_d \mathbf{u}_t(k), \quad (2.24b)$$

$$\mathbf{x}_t(0) = \mathbf{x}_{t,0}, \quad (2.24c)$$

$$(2.15), (2.17), (2.19), (2.23), \quad (2.24d)$$

with \mathbf{A}_d and \mathbf{B}_d as the discretized state and input matrices of the transformed wind turbine dynamics. The optimal inputs generated by the OCP, namely $P_{r,i}^*$ and P_g^* need to be translated back into the original variables $\beta_i^* = \Psi(v_i, K_g^*, P_{r,i}^*)$ and $T_g^* = P_g^* / \left(\sqrt{2K_g^*(t)/J_{\text{hss}}} \right)$, respectively, to be implementable by the wind turbine, where $\Psi(\cdot)$ denotes the pitch look-up table [51].

The initial states of the internal model in (2.24c) are given by either the measurements or state estimators. For this particular case, the kinetic energy value is derived from the measured generator speed while the tower states are provided by a Luenberger estimator [64] incorporating the nominal tower dynamics (2.10). More specifically, the side-side force estimate \hat{F}_{ss} , calculated based on the wind speed, pitch angles, and rotor speed information, is fed into the Luenberger estimator together with the measured \hat{x}_{ss} , from which the tower state estimates, \hat{x}_{ss} and \hat{x}_{ss} , are obtained.

Regarding the wind speed information, it is assumed that a rotor-effective wind speed (REWS) estimate \hat{v}_{RE} is sufficient as a substitute to the blade-effective wind speeds, i.e., $v_i(k) = \hat{v}_{\text{RE}}(k)$ for $i \in \{1, 2, 3\}$, and hence, the Immersion-and-Invariance (I&I) REWS estimator is employed. The reader interested in the detailed description of the I&I estimator is referred to [65]. For a more advanced IPC purpose, such as used for blade load mitigation, blade-effective wind speed estimates, representing more accurate spatial variability information of the wind, might be necessary [66].

2.5 Simulation Results and Discussions

In this section, the effectiveness of the proposed CEMPC method for the side-side tower damping is demonstrated by utilizing a high-fidelity simulation environment FAST [67], with a sampling time of 0.01 s. MOSEK optimization software [68] is employed as the numerical solver for the CEMPC, in which the prediction horizon $N_p = 100$ and 0.2 s of update rate are applied. To represent modern multi-megawatt wind turbines, NREL 5 MW reference turbine [25] is incorporated as both FAST and CEMPC (internal) models. The simulation setup comprising the wind turbine, proposed CEMPC, as well as wind speed and state estimators, as explained in the previous section, are depicted in Figure 2.2.

Two cases were considered in this work: steady and turbulent wind conditions. The former is dedicated to studying the trade-off of the conflicting economic objectives of the CEMPC present in the objective function (2.22) and hence several sets of weights are applied and their closed-loop behaviors are compared. In the latter, the performance of the CEMPC without and with active damping by IPC is studied, where the fatigue load mitigation and the pitch actuation are evaluated by investigation of the spectral content

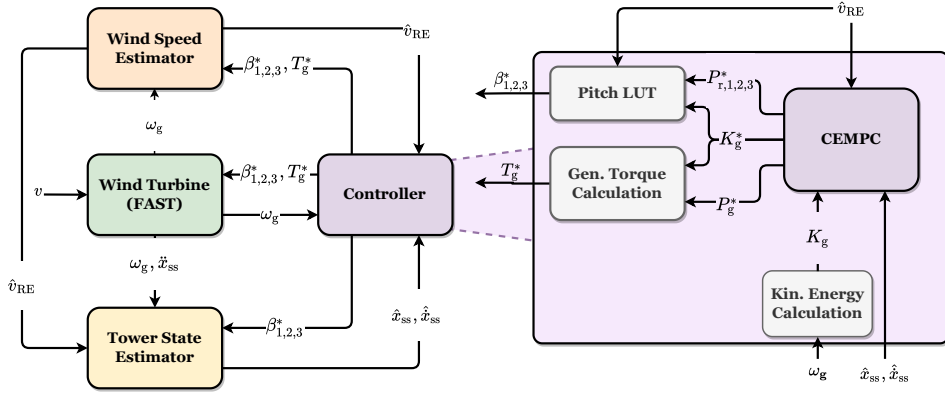


Figure 2.2: Convex economic model predictive control high-fidelity simulation setup.

of the measured side-side tower bending moment and pitch angle. Moreover, damage equivalent loads (DELs) of the blade bending moments, apart from that of the tower, are computed to study the effect of the proposed damping strategy on the blade loads. Finally, the impact on power production is discussed.

For both cases, only above-rated wind speeds are considered since at below-rated, maximum power production is the main goal. This means that the aerodynamic powers $P_{r,i}$ seek to reach their upper bounds in this region, i.e., $P_{r,i} = P_{av,i}$ and therefore, the capability to vary the side-side force becomes limited and for the remainder of this section, the evaluation at this region is not considered.

2.5.1 Steady Wind Case

From the objective function \mathcal{J}_{OCF} in (2.22), one may have realized that some objectives are conflicting with each other. For the side-side tower damping by IPC, as considered in this work, higher damping is related to higher pitch activities, which can be detrimental to the actuators' lifetime. Hence, it can be inferred that the fourth (aerodynamic powers ROC penalty) and sixth (tower velocity penalty) terms of \mathcal{J}_{OCF} have some trade-offs. Several combinations of these weights, as summarized in Table 2.1², were considered and then tested under a steady wind simulation with $v = 16$ m/s to demonstrate the above points. Figure 2.3 depicts the closed-loop performance result of the different CEMPC weights.

Compared with the benchmark, the first weight configuration results in an active individual pitching. The CEMPC attempts to manipulate the in-plane blade forces such that side-side tower-top force F_{ss} is created to counteract the tower excitation, reflected in a faster damping rate of the tower acceleration measurement \dot{x}_{ss} . When w_6 is increased, as is the case in the second configuration, the pitch becomes increasingly active, generating more F_{ss} , and even quicker damping of \dot{x}_{ss} . The third configuration, which uses less aerodynamic powers ROC penalty, creates better damping with respect to the previous

²It should be noted that the weight units in Table 2.1 differ with each other due to normalization of some objectives for numerical stability ($w_1 - w_5$), ROC penalization objectives (w_4 and w_5), and inversion of the squared acceleration unit (w_6).

Table 2.1: Tuning weight configurations for steady wind speed simulation.

| Configuration | w_1 (-) | w_2 (-) | w_3 (-) | w_4 (s ²) | w_5 (s ²) | w_6 (s ⁴ /m ²) |
|---------------|-----------|-----------|-----------|-------------------------|-------------------------|---|
| Benchmark | 1 | 1 | 5 | 30 | 25 | 0 |
| 1 | 1 | 1 | 5 | 30 | 25 | 5 |
| 2 | 1 | 1 | 5 | 30 | 25 | 10 |
| 3 | 1 | 1 | 5 | 15 | 25 | 10 |

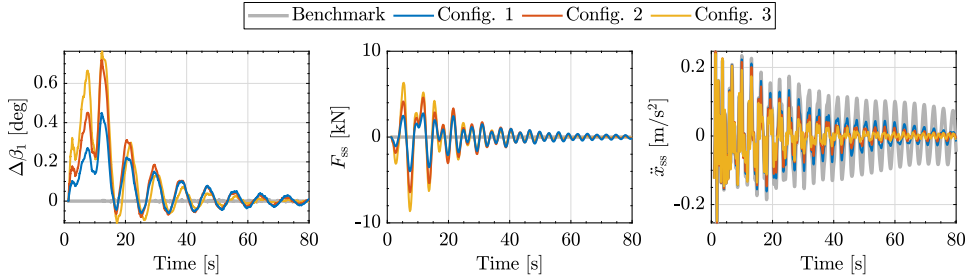


Figure 2.3: Time series result of steady wind speed case at $v = 16$ m/s, demonstrating the performance of the proposed convex economic model predictive control (CEMPC) under different weights (see Table 2.1). The left plot demonstrates the first pitch activities, only shown as its deviation from the collective component for clarity, i.e., $\Delta\beta_1 = \beta_{\text{col}} - \beta_1$. The middle plot depicts the tower-top force F_{ss} calculated by the CEMPC's internal model and the right plot shows the tower acceleration \ddot{x}_{ss} measured from FAST.

configuration at the cost of more pitch activities. The key takeaway of this observation is that two conflicting economic objectives of the CEMPC for side-side tower damping by IPC have been identified and confirmed, which may aid in controller tuning decisions.

2.5.2 Turbulent Wind Case

In this case, a realistic, extreme turbulent wind is considered with $v = 16$ m/s of mean wind speed and 14% of turbulence intensity. The simulation was run for $t = 660$ s, in which the first 60 s were trimmed to remove the computational transients from the evaluation. The CEMPC without and with active damping, in this case, re-implement the benchmark and the third configuration of Table 2.1, respectively, with w_6 increased to 20 s⁴/m² for the latter.

Figure 2.4 demonstrates the effectiveness of the active damping by IPC, where the side-side tower bending moment signal M_{ss} time series are shown alongside the blade pitch measurements. Significant reduction in the M_{ss} is evident thanks to the active damping by individual pitching. It can be observed that the individual pitch angles β_i , $i \in \{1, 2, 3\}$, create both steady-state offsets as well as a slowly-varying component in order to damp the tower vibration, which is made more evident from the spectral analysis in the following.

In Figure 2.5, the power spectral density (PSD) of the tower bending moment and pitch measurements are presented. Compared with the benchmark case, the CEMPC with active damping shows reduced frequency content of the former at the tower's first eigenfrequency, which is $f_{\text{tWT}} = 0.32$ Hz for NREL 5 MW wind turbine. The latter, in turn, has an increased steady-state as well as $f_{\text{tWT}} - f_{1\text{P}}$ frequency contents, where $f_{1\text{P}} \approx 0.2$ Hz at above-

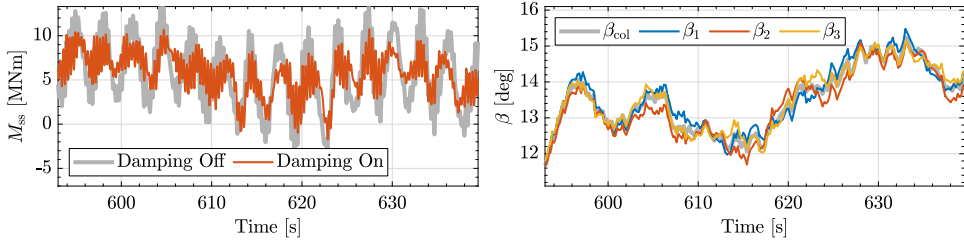


Figure 2.4: Time series of the side-side tower bending moment M_{ss} (left) and pitch activities (right) during the turbulent wind case.

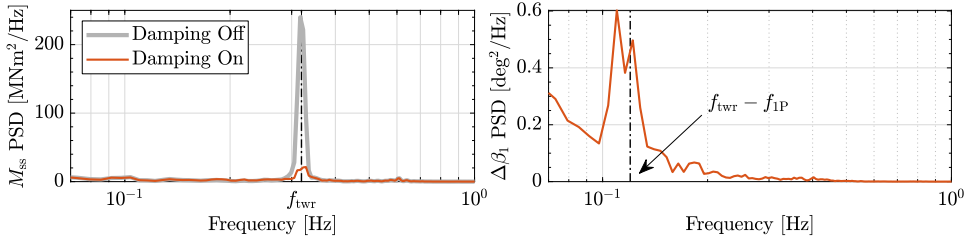


Figure 2.5: Power spectral density (PSD) plots of side-side tower bending moment M_{ss} (left) and first blade pitch offset from its collective component $\Delta\beta_1$ (right) for the turbulent wind case.

rated, which confirms the time-series observation. In theory, an increase in the $f_{twr} + f_{IP}$ frequency component should also be observed in the PSD of the individual pitch [34]. The reason why this is currently not the case is possibly due to the relatively high aerodynamic powers ROC penalty which hinders higher-frequency pitch signals from playing a role. Nevertheless, since fast pitch actuation might accelerate the actuator's wear, this absence could be an advantage of the current approach.

It is also of interest to assess the fatigue damage experienced by the wind turbine components by calculating their DELs. Mainly, it is compelling to investigate not only the DEL of the side-side tower bending moment but also those of the blades as they could be impacted by the pitching activities. For the respective tower and blade materials, steel and composite are assumed; therefore, Wöhler exponent of 4 is selected for the former and 10 for the latter in DEL computation using MLife [69]. In Figure 2.6, the computed DELs of M_{ss} , as well as flapwise ($M_{fl,1}$) and edgewise ($M_{ed,1}$) bending moments of the first blade are depicted—normalized with respect to the benchmark results. Compared with the benchmark case, 21.633% lower DEL of M_{ss} is obtained by the implementation of CEMPC with active damping. As for the blade, the computed DEL of $M_{fl,1}$ results in only 0.1755% higher value, while 0.11% lower DEL is observed for $M_{ed,1}$, with respect to the benchmark. Such little influence by the proposed method on the blade fatigue loads is likely caused by the minimum pitch activities at frequencies where these loads are dominant, i.e., at f_{IP} and its harmonics [15] (see Figure 2.5).

In terms of power production, 4.9827 MW of mean power is generated with 37.5088 kW of standard deviation under the CEMPC without active damping. When the damping feature of the CEMPC is turned on, a slightly higher mean power of 4.9831 MW is

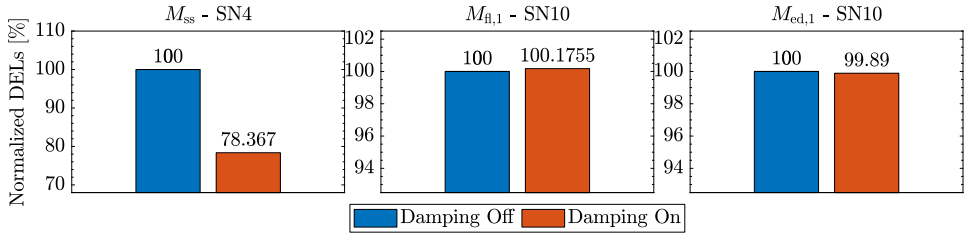


Figure 2.6: Normalized DELs of the side-side tower bending moment M_{ss} (left) and the flapwise (middle) and edgewise (right) bending moments of the first blade, $M_{fl,1}$ and $M_{ed,1}$, respectively.

generated with a lower standard deviation of 36.4958 kW. Although the proposed method demonstrates better power production quality, the extent to which such improvement can be made needs further study.

2.6 Conclusions

In this chapter, the CEMPC framework by Hovgaard, et al. [51] has been extended with IPC to mitigate the side-side tower fatigue loads of wind turbines. A variable transformation based on power and energy terms has been conducted to obtain linear dynamics and convex constraints, which enables a convex OCP to be employed. The effectiveness of the proposed method has been demonstrated in a high-fidelity simulation environment FAST at the above-rated region. The conflicting economic objectives of the active tower damping, namely the tower motion and pitch actuation penalties, have been identified and validated in a steady wind case. In a turbulent wind case, the proposed method has been shown to reduce the spectral content of the side-side tower base bending moment at the tower's first eigenfrequency, while the pitch spectral content at the steady-state and $f_{twr} - f_{1P}$ frequencies are increased with respect to the undamped case. Fatigue assessment of the side-side tower bending moment under active damping has shown considerable reduction in terms of DEL with negligible effects on those of the blade bending moments. Minor improvements in the power production aspect have also been observed when the IPC is active. Future work will include a comparison with a conventional baseline controller, augmentation of further load reduction objectives, such as tower fore-aft damping and blade load mitigation, and multi-objective controller assessment.

3

3

Convex Economic Model Predictive Control for Blade Loads Mitigation on Wind Turbines

Economic model predictive control (EMPC) has received increasing attention in the wind energy community due to its ability to trade off economic objectives with ease. However, for wind turbine applications, inherent nonlinearities, such as from aerodynamics, pose difficulties in attaining a convex optimal control problem (OCP), by which real-time deployment is not only possible but also a globally optimal solution is guaranteed. A variable transformation can be utilized to obtain a convex OCP, where nominal variables, such as rotational speed, pitch angle, and torque, are exchanged with an alternative set in terms of power and energy. The ensuing convex EMPC (CEMPC) possesses linear dynamics, convex constraints, and concave economic objectives and has been successfully employed to address power control and tower fatigue alleviation. This work focuses on extending the blade loads mitigation aspect of the CEMPC framework by exploiting its individual pitch control (IPC) capabilities, resulting in a novel CEMPC-IPC technique. This extension is made possible by reformulating static blade and rotor moments in terms of individual blade aerodynamic powers and rotational kinetic energy of the drivetrain. The effectiveness of the proposed method is showcased in a mid-fidelity wind turbine simulation environment in various wind cases, in which comparisons with a basic CEMPC without load mitigation capability and a baseline IPC are made.

3.1 Introduction

Horizontal axis wind turbine rotor sizes have been consistently increased to improve nameplate power ratings [13]. However, being ever longer and more flexible, wind turbine blades experience exacerbated asymmetric loadings due to the greater influence of turbulence, wind shear, tower shadow, and yaw misalignment [15]. Such wind spatio-temporal variability gives rise to the spectral contents of the blade loads at once-per-rotation (1P) frequency and its higher harmonics (2P, 3P, etc.), which are reflected as 0P, 3P, 6P, and so on at the fixed support structure for three-bladed turbines [39]. These fatigue loadings, accumulated over time, may eventually lead to irreversible damage—impeding economic benefits of power generation from being attained as wind turbine lifetime becomes shorter. Hence, the importance of advanced control strategies with the capabilities to handle fatigue load minimization alongside power production maximization becomes higher than ever.

Individual pitch control (IPC), by which wind turbine blades are individually actuated in response to measured out-of-plane (OoP) blade root bending moments, has played a pivotal role in alleviating the aforementioned asymmetric loads. In conventional IPC, these blade load signals in the rotating frame, containing dominant 1P frequency, are projected by an azimuth-dependent Coleman transformation [39] onto tilt and yaw axes in the fixed frame. On these orthogonal axes, a pair of identical single-input single-output (SISO) controllers, such as proportional-integral (PI) compensators [15] or simple integrators [70], is then designed for canceling the static (0P) tilt and yaw loads to create blade pitch commands on each axis. A reverse Coleman transformation subsequently projects the blade pitch signals back into the rotating frame to obtain 1P individual pitch actions, thus reducing the 1P and 0P load components in the respective rotating and fixed parts of the turbine [15, 70].

Aside from PI and other loop-shaping methods alike, different approaches to realize blade loads mitigation are also present in the literature. Optimal state-feedback methods, such as linear quadratic regulator [33] and linear quadratic Gaussian [15, 63, 71] were considered, in which state regulation and control input penalization trade-off tuning are accommodated. Others investigated H_∞ -based approaches [72–74], which are capable of handling multivariable systems as well as accounting for uncertainties in the model and measurements. In spite of their advantages, these classes of controllers are not able to altogether (1) take into account system constraints, (2) address multivariable systems with ease, (3) provide convenient trade-offs between different control objectives, and (4) predict the future behavior of the system given current (or preview) information, several properties of which are inherent in model predictive control (MPC) designs [48].

MPC is a model-based control algorithm that optimizes a system's inputs to attain certain control objectives over a finite prediction horizon in the future while adhering to the system's constraints [75]. In the vast majority of MPC implementations, tracking objectives are employed within its optimization control problem (OCP) formulation to steer a system to certain precalculated steady-state references, known as the tracking MPC (TMPC). Several studies have demonstrated the potential of TMPC for wind turbine applications, such as for power control, tower damping, blade loads mitigation, and combinations thereof [64, 76–80]. Regardless of the demonstrated good performance, TMPC is somewhat lacking in terms of the straightforward connection between its track-

ing objective and the actual objective of wind turbine operation, namely economic performance [81]. On top of that, a common assumption that tracking steady-state references bring the most profit may not necessarily be true, particularly during transients [62]. Fortunately, these predicaments can be tackled by the incorporation of economic objectives in place of reference tracking ones, resulting in the economic MPC (EMPC).

Early work on EMPC for wind turbine control focused on the power maximization aspect and development of ‘turnpike’¹ correction, which has hindered short time horizon implementation of EMPC [81], with an extension followed, in which tower fatigue mitigation and trade-off tuning by Pareto front are accounted for [82]. In these works, quasi-convex OCPs are employed, where the convexity of the formulated OCPs holds in a certain operating region. A number of studies incorporating convex EMPC (CEMPC) methods, by which a globally optimal solution is ensured and real-time implementation is made possible, have been investigated. As an instance, CEMPC has been employed for preventing soft-soft tower resonance in the presence of rotor imbalance at the below-rated region by frequency-skipping [53]. The convexity of the OCP in this framework owes to the property of the wind turbine dynamics incorporated therein, cast as that of quasi-linear parameter-varying by a model demodulation transformation technique. Another OCP convexification strategy in the literature is realized by transforming nominal wind turbine variables into power and energy terms such as rotational kinetic energy, aerodynamic power, and generator power to obtain concave objectives (to be maximized), linear dynamics, and convex constraints. The optimal control inputs resulting from the optimization routine then undergo a reverse variable transformation to obtain implementable wind turbine signals in the nominal variables, such as blade pitch and generator torque demands. Such a CEMPC concept was initially introduced with the goal of ensuring the smoothness of grid power delivery with an integrated local storage system [51].

Some research efforts followed afterward, extending the latter CEMPC framework to account for fore-aft [52, 83] and side-side [84] tower fatigue loads mitigation. Of particular interest is the latter extension since an individual pitching strategy was favored over the more conventional approach by generator torque control in order to lessen the variation of the generated power as a by-product of the damping activities. The decomposition of a single aerodynamic power acting on the rotor into multiple components, referring to those of the blades, has become a key to realizing individual pitching within the framework. By reformulation of the side-side blade forces in terms of these aerodynamic powers and rotational kinetic energy, a tower-top force counteracting tower vibrations can be created by CEMPC. Yet, little to no attention is paid to the augmentation of a blade loads mitigation objective, exploiting further the IPC potential of the CEMPC framework.

This chapter thus aimed to fill the knowledge gap by incorporating an individual pitching mechanism for blade loads alleviation into the CEMPC framework by the authors [51, 84]. In detail, this extension includes OoP blade root bending moments and rotor tilt and yaw moments as parts of the wind turbine model description. By recasting these moments, alongside simplified drivetrain dynamics and relevant constraints, into their equivalence in terms of individual aerodynamic powers and rotational kinetic energy, linear dynamics and convex constraints are obtained. On top of that, employing concave

¹In this case, it is the total absorption of rotor kinetic energy for power generation, resulting in an entirely stopped rotor.

objective functions (to be maximized) results in a convex OCP, by which not only globally optimal control inputs (with respect to the internal model and available information through measurement and estimation data) are guaranteed but also real-time implementation is made possible. Furthermore, the benefit of EMPC, in terms of convenient trade-off tuning capability between different economic objectives, can also be performed. For the remaining parts of this chapter, this novel method is referred to as the “CEMPC-IPC.” The contributions of this work are now in order as follows:

3

1. Establishing linear wind turbine dynamics and convex constraints suitable for blade loads mitigation by individual pitching, by application of a variable transformation in power and energy terms to a nominal wind turbine model description;
2. Formalizing a convex OCP by incorporation of concave economic objective functions (to be maximized), which cater for the penalization of rotor tilt and yaw moments, on top of the linear dynamics and convex constraints;
3. Integrating the Coleman blade-effective wind speed estimator [66], as well as an unscented Kalman filter for rotor tilt and yaw moment biases estimation, to supply the proposed CEMPC-IPC with unknown and unmeasurable quantities;
4. Showcasing the performance of the CEMPC-IPC in a mid-fidelity wind turbine simulation environment under artificial and realistic wind profiles, including comparisons with a basic CEMPC and a conventional IPC.

The remainder of this chapter proceeds as follows. Section 3.2 describes a nonlinear reduced-order wind turbine dynamical model along with their constraints in the nominal wind turbine variables. Section 3.3 elaborates on the derivation of the linear wind turbine dynamics and convex constraints by a transformation of variables in power and energy terms. The formulation of the convex economic OCP of the proposed CEMPC-IPC is laid out in Section 3.4, where the required estimator designs are also discussed. In Section 3.5, the effectiveness of the CEMPC-IPC is demonstrated in a mid-fidelity computer-aided wind turbine simulation setup FAST (Fatigue, Aerodynamics, Structures, and Turbulence) [67] by the National Renewable Energy Laboratory (NREL). Finally, in Section 3.6, the concluding remarks of this work are given.

3.2 Wind Turbine Model

In model-based control methods such as MPC, obtaining a system’s dynamic model is a critical first design step. To prevent a too high computational burden, a reduced-order model with the ability to capture the most relevant dynamics according to the control objectives is preferable over high-order ones. In this section, the first-principles derivation of the nominal wind turbine model comprising of drivetrain dynamics and static blade and rotor moments is conducted in Sections 3.2.1 and 3.2.2, respectively. In Section 3.2.3, several remarks regarding potential nonconvexity ensuing from model nonlinearities, motivating the adoption of variable transformation in the power and energy terms, are laid out.

3.2.1 Drivetrain Dynamics

To model a wind turbine drivetrain, a single mass representation of the drivetrain dynamics on the high-speed shaft (HSS) side is considered, which is governed by the following equation [51]

$$J_{\text{hss}}\dot{\omega}_g(t) = T_r(t)/G - T_g(t), \quad (3.1)$$

with t being the continuous time notation. The HSS equivalent inertia is denoted by $J_{\text{hss}} = J_g + J_r/G^2$, with J_g , J_r , and $G \geq 1$ as the generator inertia, rotor inertia, and gearbox ratio, respectively. The notation ω_g represents the generator rotational speed, being a system's state, operated within the range

$$0 \leq \omega_g(t) \leq \omega_{g,\text{max}}, \quad (3.2)$$

where $\omega_{g,\text{max}}$ is the maximum allowable speed for the generator, chosen to be 130% of the rated value $\omega_{g,\text{rated}}$. The generator torque T_g is a control input constrained by

$$0 \leq T_g(t) \leq T_{g,\text{rated}}, \quad (3.3)$$

with $T_{g,\text{rated}}$ defined as the rated generator torque producing wind turbine nameplate power rating $P_{g,\text{rated}}$ at $\omega_{g,\text{rated}}$, taking into account the generator efficiency.

The aerodynamic torque T_r is often modeled as a single quantity affecting the entire rotor disk, including in the original CEMPC work [51]. Nevertheless, it can also be thought of as the sum of multiple blade-effective quantities [63, 84] $T_{r,i}$, with $i \in \{1, 2, 3\}$ for three-bladed wind turbines, which is especially beneficial for IPC formulations, as considered in this work. This accumulation of individual blade torques is expressed by the following relation

$$T_r(t) = \sum_{i=1}^3 T_{r,i}(t). \quad (3.4)$$

As the blades rotate under the same rotor speed $\omega_r = \omega_g/G$ altogether, their extracted aerodynamic powers from the wind contribute to that of the rotor disk P_r as

$$P_r(t) = \omega_r(t) \sum_{i=1}^3 T_{r,i}(t) = \sum_{i=1}^3 P_{r,i}(t), \quad (3.5)$$

in which

$$P_{r,i}(t) = \frac{1}{6} \rho A C_p(\omega_r(t), \beta_i(t), v_i(t)) v_i(t)^3. \quad (3.6)$$

The air density, considered to be 1.225 kg/m^3 , and the rotor area are denoted respectively by ρ and $A = \pi R^2$, with R being the radius of the rotor. The notation C_p refers to the aerodynamic power coefficient, being a function of ω_r , the blade-effective wind speed (BEWS) v_i , and the individual blade pitch β_i , constrained by

$$\beta_{\text{min}} \leq \beta_i(t) \leq \beta_{\text{max}}. \quad (3.7)$$

Such a coefficient is commonly provided in the form of a look-up table, the data of which are collected from simulations at different operating points.

The main output of the drivetrain operation is the generated power, computed as follows

$$P_g(t) = \eta_g \omega_g(t) T_g(t), \quad (3.8)$$

with the efficiency factor $\eta_g \in (0, 1]$ accounting for losses due to the mechano-electrical power conversion. The produced power is subjected to the following constraints

$$0 \leq P_g(t) \leq P_{g,\max}(t), \quad (3.9)$$

with the maximum generated power defined as [52]

$$P_{g,\max}(t) = \min(\eta_g \omega_g(t) T_{g,\text{rated}}, P_{g,\text{rated}}), \quad (3.10)$$

which varies based on the current ω_g and holds P_g constant at $P_{g,\text{rated}}$ when ω_g excurses above $\omega_{g,\text{rated}}$ to prevent generator overloading.

3.2.2 Static Blade and Rotor Moments Formulation

To incorporate blade loads mitigation aspects into the proposed CEMPC-IPC, additional differential equations may be employed to model the dynamics of the blades [76, 85] at the expense of increased model order and thus computational demand. An alternative path is to employ static blade moments based on the blade-element momentum (BEM) theory [63, 86] such as adopted in this chapter.

As briefly mentioned in Section 3.1, the OoP blade root bending moment $M_{\text{op},i}$ suffers from severe 1P fatigue loading from the spatial and temporal variations in the wind over the rotor disk and hence subject of mitigation by the proposed CEMPC-IPC. As illustrated in Figure 3.1, such a moment is built by a thrust or normal force $F_{t,i}$ acting on a particular distance from the rotor center

$$M_{\text{op},i}(t) = s_c F_{t,i}(t) R, \quad (3.11)$$

where the scaling factor $s_c = 2/3$ for a linearly increasing force distribution along the blade span [63]. The individual blade thrust force in the above expression is defined as

$$F_{t,i}(t) = F_{\text{dyn},i}(t) C_t(\omega_r(t), \beta_i(t), v_i(t)), \quad (3.12)$$

with

$$F_{\text{dyn},i}(t) = \frac{1}{6} \rho A v_i(t)^2, \quad (3.13)$$

being the dynamic force. The aerodynamic thrust coefficient C_t , similar to C_p , is a function dependent on ω_r , β_i , and v_i .

As depicted in Figure 3.1, the loads experienced by $M_{\text{op},i}$ are also transferred to the support structure in tilt and yaw (or horizontal and vertical) directions, therefore designing controllers on these axes to mitigate both load components are of interest. This requires the projection $M_{\text{op},i}$ from the rotating frame onto the nonrotating tilt and yaw axes,

$$M_{\text{tilt}}(t) = \frac{2}{3} \sum_{i=1}^3 M_{\text{op},i}(t) \cos(\psi_i(t)), \quad (3.14)$$

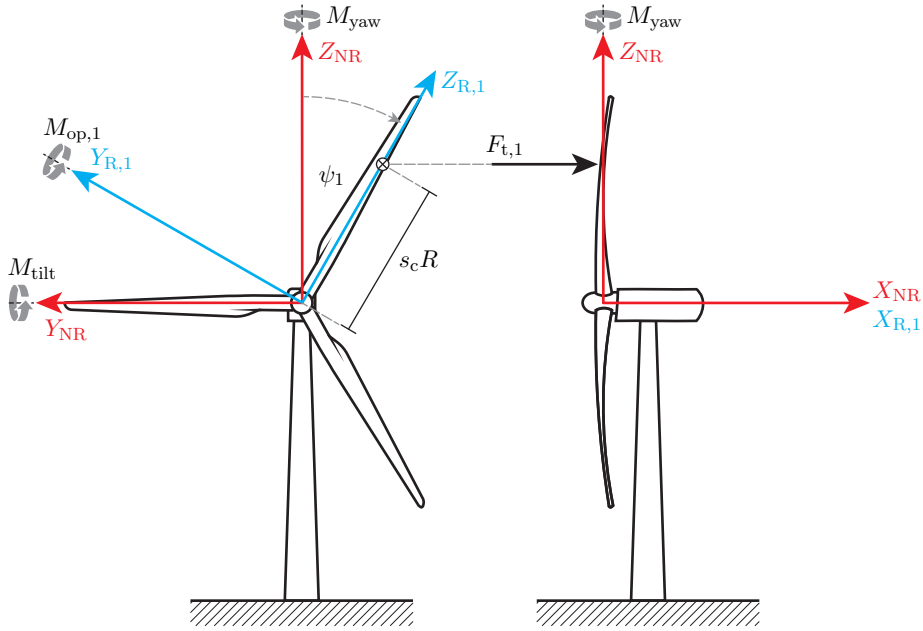


Figure 3.1: First blade thrust force $F_{t,1}$, shown to act at $s_c R$ from the rotor center, with s_c being a scaling factor and R the rotor radius. Subsequently, the out-of-plane blade root bending moment $M_{op,1}$ is created in the rotating reference frame (blue axes). The projections of $M_{op,i}$, $i \in \{1, 2, 3\}$, in the nonrotating reference frame (red axes), that is, the tilt (M_{tilt}) and yaw moments (M_{yaw}), are obtained by means of the azimuth-dependent forward Coleman transformation, where the first blade azimuth is indicated by ψ_1 . Note that the origins of both reference frames are situated at the rotor apex with their X axes directed toward the downwind direction.

and

$$M_{yaw}(t) = \frac{2}{3} \sum_{i=1}^3 M_{op,i}(t) \sin(\psi_i(t)), \quad (3.15)$$

respectively, which is known as the forward Coleman transformation. The azimuth angle of the i -th blade $\psi_i = \int \omega_t dt + 2\pi(i-1)/3$ is considered to be 0° at vertically upward position and increases in the clockwise direction. The original Coleman transformation also involves the computation of the collective component of $M_{op,i}$; however, as this component serves little to no relevance for IPC designs, it is often disregarded.

3.2.3 Potential Nonconvexity and Related Challenges for CEMPC-IPC Design

Several remarks need to be made regarding the formulated wind turbine model in Sections 3.2.1 and 3.2.2, which can also be expressed as the following general state space representation

$$\begin{cases} \dot{\mathbf{x}}(t) = \mathbf{f}(\mathbf{x}(t), \mathbf{u}(t), \mathbf{d}(t)) \\ \mathbf{y}(t) = \mathbf{g}(\mathbf{x}(t), \mathbf{u}(t), \mathbf{d}(t)) \end{cases}, \quad (3.16)$$

with the respective state, inputs, disturbances, and outputs as follows

$$\begin{cases} \mathbf{x}(t) = \omega_g(t) \\ \mathbf{u}(t) = [\beta_1(t), \beta_2(t), \beta_3(t), T_g(t)]^\top \\ \mathbf{d}(t) = [v_1(t), v_2(t), v_3(t)]^\top \\ \mathbf{y}(t) = [\omega_g(t), P_g(t), M_{\text{tilt}}(t), M_{\text{yaw}}(t)]^\top \end{cases} \quad (3.17)$$

In particular, the nonlinearities contained in (3.16) in the variables (3.17) may result in nonconvexity during the economic model predictive controller design phase. These nonlinearities are highlighted hereunder:

1. The coefficient C_p is a nonlinear function in the above-mentioned variables, particularly ω_g , β_i , and v_i , which, combined with the cube of the wind speed v_i^3 , render $P_{r,i}$ also nonlinear in these variables. As $T_{r,i}$ carries over such nonlinearities through the relation (3.5), the drivetrain dynamics (3.1) or, similarly, \dot{x} in (3.16), are thus nonlinear in nature;
2. The generated power P_g is bilinear in ω_g and T_g as shown in (3.8), which is another form of nonlinearity contained in the model, in particular in the output vector \mathbf{y} ;
3. Similar to C_p , the coefficient C_t contained in $F_{t,i}$ is nonlinear in ω_g , β_i , and v_i . Together with the squared wind speed v_i^2 , $F_{t,i}$ becomes nonlinear in the variables (3.17). This is carried over to $M_{\text{op},i}$ as expressed in (3.11) and subsequently to \mathbf{y} by M_{tilt} and M_{yaw} as shown in relations (3.14) and (3.15).

The above existing nonlinearities may ensue in a nonconvex OCP formulation of EMPC. Such an OCP promotes the utilization of nonconvex programming methodologies, in which a globally optimal solution is not guaranteed to be found, not to mention the resulting higher computational complexities. A possible solution to this challenge is by applying first-order Taylor expansion to the nonlinear quantities so as to obtain their Jacobian matrices, which are linear in their variables. One may also opt for variable transformation capable of rendering the dynamics and constraints suitable for convex optimization algorithms [51, 84]. The latter approach is adopted in this study and discussed in the next section.

3.3 Transformed Wind Turbine Model

Being nonlinear in its variables, the wind turbine model derived in Section 3.2 needs to be recast into an alternative one suitable for CEMPC-IPC deployment. The main idea is to substitute a number of variables in (3.17), specifically ω_g , β_i , and T_g with rotational kinetic energy K_g , $P_{r,i}$, and P_g , respectively, which results in the following new set of variables

$$\begin{cases} x_t(t) = K_g(t) \\ \mathbf{u}_t(t) = [P_{r,1}(t), P_{r,2}(t), P_{r,3}(t), P_g(t)]^\top \\ \mathbf{d}_t(t) = [v_1(t), v_2(t), v_3(t)]^\top \\ \mathbf{y}_t(t) = [K_g(t), P_g(t), M_{\text{tilt}}(t), M_{\text{yaw}}(t)]^\top \end{cases} \quad (3.18)$$

Accordingly, the change of the system's state from x to x_i above necessitates the drivetrain dynamics (3.1) and the corresponding system constraints, namely (3.2), (3.3), (3.7), and (3.9), to be re-expressed in the new terms. Since such a dynamics reformulation has been treated in the previous CEMPC works [51, 84], only brief summary of its derivation is presented in Section 3.3.1. Moreover, despite being kept as outputs in (3.18), the rotor moments M_{tilt} and M_{yaw} are still functions of the nominal variables (3.17) such that their equivalence in power and energy variables is yet to be established. This reformulation constitutes one of the main contributions of this study and is treated in Section 3.3.2.

3.3.1 Kinetic Energy Dynamics

Following the introduction of the new variables (3.18), the drivetrain dynamics previously described as a torque balance equation are now rewritten as the rate-of-change (ROC) of the stored rotational kinetic energy $K_g = (J_{\text{hss}}/2)\omega_g^2$, namely,

$$\dot{K}_g(t) = J_{\text{hss}}\dot{\omega}_g(t)\omega_g(t) = \left(\sum_{i=1}^3 T_{r,i}(t)/G - T_g(t) \right) \omega_g(t) = \sum_{i=1}^3 P_{r,i}(t) - P_g(t)/\eta_g. \quad (3.19)$$

This expression enables a new perspective to see the drivetrain dynamics as a power balance equation and is linear in their inputs. It is thus subject to the bounds on K_g , which are readily obtained by calculating the kinetic energies of $\omega_{g,\min}$ and $\omega_{g,\max}$ in (3.2)

$$(J_{\text{hss}}/2)\omega_{g,\min}^2 \leq K_g(t) \leq (J_{\text{hss}}/2)\omega_{g,\max}^2, \quad (3.20)$$

and to the constraints of the inputs $P_{r,i}$ and P_g explained in the following.

The ability provided by $P_{r,i}$ to store energy in the rotating system (3.19) is limited by the rotor aerodynamic characteristics embodied in C_p , which is not only dependent on $\omega_r = \sqrt{2K_g/J_{\text{hss}}}/G$ and v_i , but also on the freedom in the pitching of the blades within the allowed range (3.7). Such a limit is known as the ‘‘available wind power,’’ which is formulated below

$$P_{\text{av},i}(K_g(t), v_i(t)) = \max_{\beta_{\min} \leq \beta_i(t) \leq \beta_{\max}} \frac{1}{6} \rho A C_p \left(\sqrt{2K_g(t)/J_{\text{hss}}}/G, \beta_i(t), v_i(t) \right) v_i(t)^3. \quad (3.21)$$

The above expression is still nonconcave of K_g , which motivates its concave approximation, in the form of piecewise linear (PWL) functions, to be formulated [51] as follows

$$\check{P}_{\text{av},i}(K_g(t), v_i(t)) = \min\{a_1 K_g(t) + b_1, \dots, a_j K_g(t) + b_j\} v_i(t)^3, \quad (3.22)$$

where a_m and b_m , with $m \in \{1, \dots, j\}$, are the PWL functions' coefficients. Therefore, the constraints for $P_{r,i}$ are formalized as follows:

$$0 \leq P_{r,i}(t) \leq \check{P}_{\text{av},i}(K_g(t), v_i(t)), \quad (3.23)$$

which is concave in K_g . The reader interested in the detailed derivation of the above constraints is referred to the work of Hovgaard et al. [51]

Remark 1 A note must be taken that in (3.21), β_{\min} is considered the minimum pitch angle before reaching the stall region. As this minimum angle differs for different combinations of K_g and v_i , the coefficient table C_p is preprocessed accordingly before reformulated into $P_{\text{av},i}$.

As for P_g , its bounds in (3.9) can be rewritten in terms of K_g as follows [52]:

$$0 \leq P_g(t) \leq \min\left(\eta_g \sqrt{2K_g(t)/J_{hss}} T_{g,\text{rated}}, P_{g,\text{rated}}\right), \quad (3.24)$$

which are convex in P_g and concave in K_g . It is important to note the use of P_g directly as a variable is advantageous in that linearization of (3.9) about $P_{g,\text{rated}}$ (due to the bilinearity in ω_g and T_g as pointed out in Section 3.2.3) is precluded. Such linearization introduces a certain degree of conservativeness since $P_{g,\text{rated}}$ may not always be reached when ω_g deviates too far from the linearization point [87].

3

3.3.2 Static Blade and Rotor Moments in Power and Energy Terms

In a previous work [84], individual pitching for mitigating side-side tower excitation within the same CEMPC framework was developed. Therein, the inclusion of IPC into the framework is made possible by virtue of lateral blade force transformation to power and energy variables. In the current chapter, a similar idea of enabling IPC for blade loads reduction is adopted in the framework. It is realized by rewriting $F_{t,i}$ in the new variables, followed by its substitutions into the blade moment $M_{\text{op},i}$ and, afterward, rotor moments M_{tilt} and M_{yaw} .

To this end, the following relation between power and torque coefficients $C_p = \lambda_i C_q$ is considered, with $\lambda_i = \sqrt{2K_g/J_{hss}} R/G v_i$ being the tip-speed ratio expressed in the new variables. The individual aerodynamic power equation (3.6) now becomes

$$P_{r,i}(t) = \frac{1}{6} \underbrace{\rho A v_i(t)^2}_{F_{\text{dyn},i}(t)} \left(\sqrt{2K_g(t)/J_{hss}} / G \right) R C_q \left(\sqrt{2K_g(t)/J_{hss}} / G, \beta_i(t), v_i(t) \right),$$

which contains $F_{\text{dyn},i}$ from (3.13) as indicated. The above realization paves the way for $F_{\text{dyn},i}$ to be rewritten in terms of power and energy as follows

$$F_{\text{dyn},i}(t) = \frac{P_{r,i}(t)}{\left(\sqrt{2K_g(t)/J_{hss}} / G \right) R C_q \left(\sqrt{2K_g(t)/J_{hss}} / G, \beta_i(t), v_i(t) \right)}.$$

By application of the above definition of $F_{\text{dyn},i}$ into (3.12), the individual blade thrust force can be readily recast into

$$F_{t,i}(t) = \frac{P_{r,i}(t)}{\left(\sqrt{2K_g(t)/J_{hss}} / G \right) R} C_{t/q} \left(\sqrt{2K_g(t)/J_{hss}} / G, \beta_i(t), v_i(t) \right), \quad (3.25)$$

with $C_{t/q}$ as the shorthand notation for C_t/C_q . Note that the inverse square root of the kinetic energy $1/\sqrt{K_g}$ contained in (3.25) is nonconvex in K_g . In addition, the coefficient $C_{t/q}$ is nonlinear in the variables K_g , β_i , and v_i , with β_i being one of the nominal variables. To tackle these additional complexities in rendering $F_{t,i}$ convex in its variables, several assumptions are thus needed.

Assumption 1 *It is assumed that K_g varies slowly over time, such that in the implementation of CEMPC-IPC later on in Section 3.4, it can be considered constant based on the current turbine measurements for the computations of $F_{t,i}$.*

Assumption 2 The calculation of $C_{t/q}$ takes constant K_g as indicated in Assumption 1, β_i of the previous CEMPC-IPC solution, and constant v_i based on the current wind speed information. This effectively leaves $P_{r,i}$ as the only decision variable for determining $F_{t,i}$.

The ensuing OoP blade root bending moment in power and energy terms is obtained straightforwardly by substitution of (3.25) into (3.11) that results in

$$M_{\text{op},i}(P_{r,i}(t)) = s_c \frac{P_{r,i}(t)}{\left(\sqrt{2\tilde{K}_g(t)/J_{\text{hss}}/G}\right)} C_{t/q} \left(\sqrt{2\tilde{K}_g(t)/J_{\text{hss}}/G}, \tilde{\beta}_i(t), \tilde{v}_i(t)\right) R, \quad (3.26)$$

where the quantities in which Assumptions 1 and 2 hold are indicated by tilde ($\tilde{\cdot}$) notations. The following and the last step in the static blade forces and moments derivation in power and energy terms is the application of forward Coleman transformation to (3.26). However, note that the use of trigonometric functions $\cos(\psi_i)$ and $\sin(\psi_i)$, with $\psi_i = \int (\sqrt{2K_g/J_{\text{hss}}/G}) dt + 2\pi(i-1)/3$, in (3.14) and (3.15) indicates additional nonconvexities in K_g , for which the following additional assumption is required.

Assumption 3 The azimuth ψ_i is taken from the measurements, which is also forward-propagated for the entire prediction horizon of the CEMPC-IPC given the measurements of ω_r .

Taking Assumption 3 into account, rotor tilt and yaw moments previously defined in (3.14) and (3.15) are now rewritten as

$$M_{\text{tilt}}(t) = \frac{2}{3} \sum_{i=1}^3 M_{\text{op},i}(P_{r,i}(t)) \cos(\tilde{\psi}_i(t)), \quad (3.27)$$

and

$$M_{\text{yaw}}(t) = \frac{2}{3} \sum_{i=1}^3 M_{\text{op},i}(P_{r,i}(t)) \sin(\tilde{\psi}_i(t)), \quad (3.28)$$

with $\tilde{\psi}$ denoting the measured/forward-propagated azimuth position.

3.4 Convex Economic Model Predictive Control Setup

An OCP is at the heart of every model predictive controller design, including the CEMPC-IPC proposed in this work. Comprising the system dynamics, constraints, and objective functions, it is solved to optimize the prediction of a system's behavior up to a finite time horizon in the future. The product of such optimization is an optimal input trajectory, the first element of which is applied to the system. The measured response due to the application of the optimal input is thus taken by CEMPC-IPC to restart the optimization so as to produce the subsequent optimal input trajectory with a one-step-ahead roll in the horizon.

In Section 3.4.1, the OCP formulation for the proposed CEMPC-IPC is discussed, in which several economic objective functions are presented and incorporated with the transformed wind turbine dynamics and constraints derived previously in Section 3.3. Moreover, as not all quantities needed to begin the optimization routine are available from the measurements, state estimators need to be integrated, which are explained in Section 3.4.2. Figure 3.2 illustrates the diagram showing the interconnection of these subsystems.

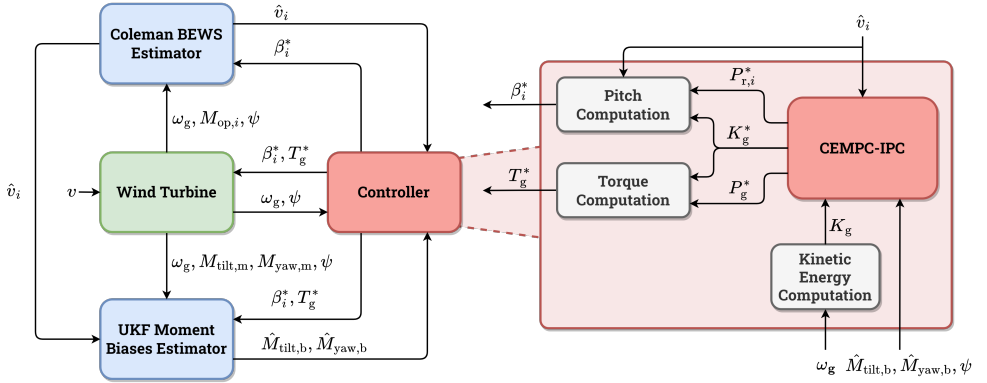


Figure 3.2: Convex EMPC (CEMPC)-individual pitch control (IPC) implementation setup. A blade-effective wind speed (BEWS) and moment biases estimator via unscented Kalman filtering (UKF) are included for providing unknown information to the controller.

3.4.1 Optimal Control Problem Formulation

As a subclass of EMPC, CEMPC inherits its feature in the sense that a system's economic performance, manifested in concave objective functions, is maximized instead of targeting the system to reach steady-state references, as done in TMPC. In the previous works [51, 84], power production maximization, reduction of overspeeding duration, and minimization of excessive actuation aspects of the wind turbine economic performance have been addressed, which are also taken into consideration here. Moreover, as an extension of these works, this study now accounts for the blade loads alleviation aspect, thereby extending the structural loads mitigation capability of the framework. Thus, for the purpose of realizing CEMPC-IPC, the following economic objective functional concave in the new variables (3.18) is proposed

$$\begin{aligned} \mathcal{J}_{\text{OCP}}(t) = & w_1 P_g(t) + w_2 \sum_{i=1}^3 \check{P}_{\text{av},i}(v_i(t), K_g(t)) - w_3 K_{g,\text{slack}}(t)^2 - w_4 \sum_{i=1}^3 \dot{P}_{r,i}(t)^2 - w_5 \dot{P}_g(t)^2 \\ & - w_6 M_{\text{tilt}}(t)^2 - w_7 M_{\text{yaw}}(t)^2, \end{aligned} \quad (3.29)$$

where w_l , $l \in \{1, \dots, 7\}$ is the corresponding weight of each term. The interpretation of each objective is explained below.

The first term of (3.29) refers to the main objective of the power control, that is, to achieve maximum generated power. To push the upper bound of the operable $P_{r,i}$ (as shown in (3.22)) higher such that the maximum available power in the wind can be extracted, the second term is included. The third term corresponds to the overspeeding penalization for reducing the duration in which K_g excurses from its rated value $K_{g,\text{rated}} = (J_{\text{hss}}/2)\omega_{g,\text{rated}}^2$ by enforcement of the following constraints

$$K_g(t) \leq K_{g,\text{rated}} + K_{g,\text{slack}}(t), \quad \text{with} \quad K_{g,\text{slack}}(t) \geq 0, \quad (3.30)$$

where $K_{g,\text{slack}}$ is a slack variable, which is realized by collective pitching to prevent $P_{r,i}$

from transferring more power to the drivetrain than the generator is able to cope with. To prevent aggressive actuators activities of β_i and T_g , penalties on the ROC of the aerodynamic power $\hat{P}_{r,i}$ and generated power \hat{P}_g are incorporated in the respective fourth and fifth terms. The sixth and seventh terms play a central role in the blade loads mitigation aspect of CEMPC-IPC as these represent the objectives to minimize the asymmetric loadings over the rotor area reflected in M_{tilt} and M_{yaw} .

Having the linear dynamics, convex constraints, and concave objective functions formulated, the convex OCP of the proposed CEMPC-IPC for blade loads mitigation can now be formalized as the following equation

$$\max_{\mathbf{U}_t} \sum_{k=0}^{N_p-1} \mathcal{F}_{\text{OCP}}(k), \quad (3.31a)$$

$$\text{s.t.} \quad \mathbf{x}_t(k+1) = \mathbf{A}_d \mathbf{x}_t(k) + \mathbf{B}_d \mathbf{u}_t(k), \quad (3.31b)$$

$$\mathbf{x}_t(0) = \mathbf{x}_{t,0}, \quad (3.31c)$$

$$(3.20), (3.23), (3.24), (3.30), \quad (3.31d)$$

with k and N_p being the discrete time notation and prediction horizon of the controller. The notations \mathbf{A}_d and \mathbf{B}_d in (3.31b) designate the respective discrete state and input matrices of the transformed wind turbine dynamics (3.19)—by which the turbine state is predicted, discretized using the Tustin/trapezoidal method [88] under the sampling time T_s . To initialize the prediction, the internal state of the controller $\mathbf{x}_t(0)$ is taken from the measurement $\mathbf{x}_{t,0}$, in (3.31c), after which the optimization adhering to the convex constraints (3.31d) is conducted.

At each time step, the OCP (3.31) outputs a globally optimal input trajectory

$$\mathbf{U}_t^* = [\mathbf{u}_t^*(0)^\top, \dots, \mathbf{u}_t^*(N_p - 1)^\top]^\top,$$

where

$$\mathbf{u}_t^{*\top} = [P_{r,1}^*, P_{r,2}^*, P_{r,3}^*, P_g^*]^\top,$$

is applied to the wind turbine, in which \mathbf{u}_t is a shorthand notation of $\mathbf{u}_t(0)$ with the asterisk symbol (*) indicating the optimal inputs. One may directly notice that \mathbf{u}_t is not directly usable for wind turbine control; therefore its equivalence in terms of the original variables

$$\mathbf{u}^{*\top} = [\beta_1^*, \beta_2^*, \beta_3^*, T_g^*]^\top,$$

must be retrieved by the following reverse transformations

$$\beta_i^* = \Psi(K_g^*, P_{r,i}^*, \hat{v}_i), \quad (3.32)$$

$$T_g^* = \frac{P_g^*}{\eta_g \left(\sqrt{2K_g^* / J_{\text{hss}}} \right)}, \quad (3.33)$$

where Ψ denotes the pitch look-up table [51] and K_g^* , with a slight abuse of notation, the prediction of the state K_g at $k = 1$.

Remark 2 *It is important to keep in mind that due to the model-plant mismatches from the model simplifications, limited data to construct coefficient tables, and mathematical manipulations for the convexification purposes, as described in the previous sections, the optimal solution resulting from solving the convex OCP (3.31) may not necessarily coincide with the global optimum of the real-world system. Still, it can be considered that the global optimality of the convex OCP with respect to the considered internal model and available measurement and estimation data is valid.*

3

3.4.2 Estimator Designs

With regard to supplying the proposed controller with important but unknown and unmeasurable information, two estimators are designed. Firstly, the BEWS v_i , needed for constructing the aerodynamic power constraints (3.23), is not typically known from the measurements. However, load-sensing technologies are available from the literature, in which the BEWS estimate \hat{v}_i can be acquired from blade loads measurements [66, 89]. In Section 3.4.2.1, the Coleman BEWS estimator design for such a purpose is described [66]. Secondly, discrepancies between the measured OoP blade root bending moments and that of the internal CEMPC-IPC model might deteriorate the performance of the blade loads mitigation in that low-frequent biases in the rotor tilt and yaw moments may appear and need to be compensated. Therefore, these unknown biases need to be estimated in which an unscented Kalman filtering approach is adopted and discussed in Section 3.4.2.2.

3.4.2.1 Coleman BEWS Estimator

To estimate v_i , a recently developed load-sensing method, namely the Coleman BEWS estimator, is employed [66] and briefly summarized hereunder. This estimation framework relies on the minimization of the error between the measured $M_{\text{op},i}$ and its estimate $\hat{M}_{\text{op},i}$ (with the hat symbol ($\hat{\cdot}$) indicating estimated values)

$$\epsilon_i(t) = M_{\text{op},i}(t) - \hat{M}_{\text{op},i}(t), \quad (3.34)$$

in which

$$\hat{M}_{\text{op},i}(t) = \frac{1}{2} \rho \text{ARC}_m(\omega_r(t), \beta_i(t), \hat{v}_i(t), \psi_i(t)) \hat{v}_i^2, \quad (3.35)$$

with C_m as the azimuth-dependent cone coefficient table. Similar to C_p and C_t , the values of C_m are collected from simulations using steady wind after the steady state is reached.

In this estimation scheme, ϵ_i is transformed into the fixed frame by a forward Coleman transformation, including the collective component $\epsilon_{\text{col}} = 1/3 \sum_{i=1}^3 \epsilon_i$, aside from the projection in the cosine and sine directions $\epsilon_{\text{tilt}} = 2/3 \sum_{i=1}^3 \epsilon_i \cos(\psi_i)$ and $\epsilon_{\text{yaw}} = 2/3 \sum_{i=1}^3 \epsilon_i \sin(\psi_i)$, respectively. The next step is to map these errors into the collective, tilt, and yaw components of the wind speed, \hat{v}_{col} , \hat{v}_{tilt} , and \hat{v}_{yaw} , respectively, by

means of integration as follows

$$\hat{v}_{\text{col}}(t) = \mathcal{K}_{\text{col}} \int_0^t \epsilon_{\text{col}}(\tau) d\tau, \quad (3.36a)$$

$$\hat{v}_{\text{tilt}}(t) = \mathcal{K}_{\text{tilt}} \int_0^t \epsilon_{\text{tilt}}(\tau) d\tau, \quad (3.36b)$$

$$\hat{v}_{\text{yaw}}(t) = \mathcal{K}_{\text{yaw}} \int_0^t \epsilon_{\text{yaw}}(\tau) d\tau, \quad (3.36c)$$

where the constants \mathcal{K}_{col} and $\mathcal{K}_{\text{tilt}} = \mathcal{K}_{\text{yaw}}$ are the corresponding integrator gains.

Following (3.36), a reverse Coleman transformation is utilized in order to project \hat{v}_{col} , \hat{v}_{tilt} , and \hat{v}_{yaw} back into the rotating domain \hat{v}_i as follows

$$\hat{v}_i(t) = \hat{v}_{\text{col}}(t) + \hat{v}_{\text{tilt}}(t) \cos(\psi_i(t)) + \hat{v}_{\text{yaw}}(t) \sin(\psi_i(t)). \quad (3.37)$$

By feeding the above wind speed estimate (along with the measurements of ω_r , β_i , and ψ_i) into (3.35), $\hat{M}_{\text{op},i}$ is obtained and a feedback interconnection is created. Subsequently, due to the integrations in (3.36), the moment estimation errors are minimized, implying that \hat{v}_i has been estimated. The interested reader is referred to the work of Liu et al. [66] for more elaborated explanations and derivations on the BEWS estimator.

3.4.2.2 Biases Estimation by Unscented Kalman Filtering

The utilization of the static modeling method as used in this study, in which aerodynamic coefficient tables are relied upon, may become one source of mismatches between the internal CEMPC-IPC model and the actual system. In addition, Assumptions 1-3 introduced earlier, as well as the differences between moment calculations in (3.11) and (3.35), may contribute further to these mismatches.

For the purpose of blade loads alleviation by the proposed method, the accuracy in the computations of M_{tilt} and M_{yaw} within the controller's internal model is of high importance. As the goal of the CEMPC-IPC is to mitigate blade loads, which is reflected predominantly as the 0P components in the rotor moments, it must be ensured that minimum static biases are exhibited with respect to the actual measurements, $M_{\text{tilt,m}}$ and $M_{\text{yaw,m}}$. Therefore, (3.27) and (3.28) need to be revised by including the corresponding biases $M_{\text{tilt,b}}$ and $M_{\text{yaw,b}}$ as follows

$$M_{\text{tilt,m}}(t) = M_{\text{tilt}}(t) + M_{\text{tilt,b}}(t), \quad (3.38a)$$

$$M_{\text{yaw,m}}(t) = M_{\text{yaw}}(t) + M_{\text{yaw,b}}(t), \quad (3.38b)$$

with the information about these unknown biases to be provided by a state estimator. To this end, a recursive estimation routine by unscented Kalman filtering (UKF) [90] is considered, where the following random-walk model for estimating the unknown parameters is augmented to the original system dynamics (3.1)

$$M_{\text{tilt,b}}(k+1) = M_{\text{tilt,b}}(k) + q_{\text{tilt,b}}(k), \quad (3.39a)$$

$$M_{\text{yaw,b}}(k+1) = M_{\text{yaw,b}}(k) + q_{\text{yaw,b}}(k), \quad (3.39b)$$

with $q_{\text{tilt,b}}$ and $q_{\text{yaw,b}}$ being the process noises of the biases.

The nonlinear state and output equations internal of the UKF are defined as follows

$$\begin{cases} \mathbf{x}_{\text{ukf}}(k+1) &= f_{\text{ukf}}(\mathbf{x}_{\text{ukf}}(k), \mathbf{u}_{\text{ukf}}(k)) + \mathbf{q}_{\text{ukf}}(k) \\ \mathbf{y}_{\text{ukf}}(k) &= h_{\text{ukf}}(\mathbf{x}_{\text{ukf}}(k), \mathbf{u}_{\text{ukf}}(k)) + \mathbf{r}_{\text{ukf}}(k) \end{cases}, \quad (3.40)$$

with

$$\begin{aligned} \mathbf{x}_{\text{ukf}}(k) &= [\omega_g(k), M_{\text{tilt,b}}(k), M_{\text{yaw,b}}(k)]^\top, \\ \mathbf{u}_{\text{ukf}}(k) &= [\beta_1(k), \beta_2(k), \beta_3(k), \hat{v}_1(k), \hat{v}_2(k), \hat{v}_3(k), T_g(k), \psi_1(k), \psi_2(k), \psi_3(k)]^\top, \\ \mathbf{y}_{\text{ukf}}(k) &= [\omega_g(k), M_{\text{tilt,m}}(k), M_{\text{yaw,m}}(k)]^\top, \\ \mathbf{q}_{\text{ukf}}(k) &= [q_{\omega_g}(k), q_{\text{tilt,b}}(k), q_{\text{yaw,b}}(k)]^\top, \\ \mathbf{r}_{\text{ukf}}(k) &= [r_{\omega_g}(k), r_{\text{tilt,m}}(k), r_{\text{yaw,m}}(k)]^\top, \end{aligned}$$

being the respective augmented state, input, output, process noise, and measurement noise vectors. Here, the noise terms are assumed to be zero-mean Gaussian random variables with covariances

$$\mathbf{Q}_{\text{ukf}} = \text{diag}(\sigma^2(q_{\omega_g}), \sigma^2(q_{\text{tilt,b}}), \sigma^2(q_{\text{yaw,b}})), \quad (3.41a)$$

$$\mathbf{R}_{\text{ukf}} = \text{diag}(\sigma^2(r_{\omega_g}), \sigma^2(r_{\text{tilt,m}}), \sigma^2(r_{\text{yaw,m}})), \quad (3.41b)$$

where σ represents the standard deviation of the indicated signal. The reader interested in the detailed procedure of UKF is referred to the literature [90].

3.5 Simulation Results and Discussions

In this section, the main results of the proposed CEMPC-IPC design are exhibited in the aero-servo-elastic mid-fidelity wind turbine simulation environment NREL FAST v8.16 [67]. As a representation of modern onshore wind turbines, the NREL-5 MW [25] reference turbine is chosen in this work, the main specifications of which are listed in Table 3.1². Nine degrees of freedom (DOFs) are activated in FAST, including the generator DOF, drivetrain rotational-flexibility DOF, two fore-aft tower bending mode DOFs, two side-side tower bending mode DOFs, two flapwise blade bending mode DOFs, and the first edgewise blade bending mode DOF.

The CEMPC-IPC optimization is implemented using YALMIP modeling interface [92], in which MOSEK [68] is incorporated as the numerical solver. For all of the simulations done for this section, the prediction horizon of $N_p = 100$ steps is considered with $T_s = 0.2$ s step size, such that 20 s of horizon length is obtained. For obtaining the required information on the BEWS and rotor moment biases, the Coleman estimator and UKF briefly explained in Section 3.4 are tuned appropriately. The values of the Coleman BEWS estimator's integrator gains are set such that \hat{v}_i can be obtained fast enough while maintaining a stable response as follows:

$$\mathcal{K}_{\text{col}} = 8.5 \cdot 10^{-7} (\text{Ns})^{-1}, \quad \mathcal{K}_{\text{tilt}} = 10^{-6} (\text{Ns})^{-1}, \quad \mathcal{K}_{\text{yaw}} = 10^{-6} (\text{Ns})^{-1}.$$

²The NREL-5 MW wind turbine used here is based on that included within FASTTool software package [91]; thus some parameters differ from the original version released by NREL.

Table 3.1: NREL 5-MW key specifications.

| Description | Notation | Value | Unit |
|-------------------------|--|-------------------------------|-------------------|
| Rated generator power | $P_{g,\text{rated}}$ | 5 | MW |
| Cut-in wind speed | v_{in} | 4 | m/s |
| Rated wind speed | v_{rated} | 11.4 | m/s |
| Cut-out wind speed | v_{out} | 25 | m/s |
| Rotor radius | R | 63 | m |
| Rotor area | A | 12,468.98 | m ² |
| Hub height | - | 90 | m |
| Optimal tip-speed ratio | λ^* | 7 | - |
| Max. power coefficient | C_p^* | 0.458 | - |
| Generator efficiency | η_g | 0.944 | - |
| Gearbox ratio | G | 97 | - |
| Generator inertia | J_g | 534.116 | kg/m ² |
| Rotor inertia | J_r | 35,776,753 | kg/m ² |
| HSS equivalent inertia | J_{hss} | 4,336.512 | kg/m ² |
| Rated generator speed | $\omega_{g,\text{rated}}$ | 1,173.7 | rpm |
| Max. generator speed | $\omega_{g,\text{max}}$ | 1.3 $\omega_{g,\text{rated}}$ | rpm |
| Rated generator torque | $T_{g,\text{rated}}$ | 43,093.55 | Nm |
| Min. pitch angle | β_{min} | 0 | ° |
| Max. pitch angle | β_{max} | 25 | ° |
| Max./min. pitch rate | $\dot{\beta}_{\text{max}} = -\dot{\beta}_{\text{min}}$ | 8 | °/s |

The tuning parameters of the UKF, being the individual process and measurement noise covariances within the matrices \mathbf{Q}_{ukf} and \mathbf{R}_{ukf} , are selected below

$$\begin{aligned} \sigma^2(q_{\omega_g}) &= 10^{-2} \quad (\text{rad/s})^2, & \sigma^2(q_{\text{tilt},b}) &= 10^{-2} \quad (\text{Nm})^2, & \sigma^2(q_{\text{yaw},b}) &= 10^{-2} \quad (\text{Nm})^2, \\ \sigma^2(r_{\omega_g}) &= 10^{-3} \quad (\text{rad/s})^2, & \sigma^2(r_{\text{tilt},m}) &= 10 \quad (\text{Nm})^2, & \sigma^2(r_{\text{yaw},m}) &= 10 \quad (\text{Nm})^2, \end{aligned}$$

such that the estimate signals $\hat{M}_{\text{tilt},b}$ and $\hat{M}_{\text{yaw},b}$ contain only slow-frequent components.

A number of deterministic and stochastic wind conditions are taken into consideration for studying the behavior and performance of the proposed controller, as well as comparison with the baseline controller. In Section 3.5.1, the former wind condition is chosen as a steady, stepped wind speed case to showcase the performance and differences of the CEMPC-IPC with respect to a basic CEMPC without any blade loads mitigation aspects. Then in Section 3.5.2, several turbulent wind conditions representing those of real-world scenarios are considered, in which its load reduction performance, as well as blade pitching activities, is assessed with respect to a baseline conventional IPC.

3.5.1 Step Wind

For the stepped wind case studied in this section, hub height wind speeds ranging between $v = 14$ and 20 m/s, with 2 m/s increment every 60 s, is employed, totaling in a simulation duration of 300 s. The first few seconds of the simulation data commonly contain computational transients of FAST, and hence, the actual simulation duration is prolonged by 1 min such that these effects can be later removed during evaluation. To induce periodic $M_{\text{op},i}$ at the $1P$ frequency, which lies about $\omega_{r,\text{rated}} = \omega_{g,\text{rated}}/G = 12.1$ rpm or 0.2 Hz, wind shear power law [13] with 0.2 exponent value and tower shadow effect are taken into ac-

Table 3.2: CEMPC-IPC weight configurations for step wind case.

| Configuration | w_1 | w_2 | w_3 | w_4 | w_5 | w_6 | w_7 |
|-----------------|-------|-------|-------|------------|-------|------------|------------|
| 1 (Basic CEMPC) | 100 | 50 | 10 | 50 | 50 | 0 | 0 |
| 2 | 100 | 50 | 10 | 50 | 50 | 100 | 100 |
| 3 | 100 | 50 | 10 | 100 | 50 | 10 | 10 |
| 4 | 100 | 50 | 10 | 25 | 50 | 10 | 10 |

Note: Weights description: w_1 : generator power maximization; w_2 : available power maximization; w_3 : overspeeding penalty; w_4 : aerodynamic power rate-of-change penalty; w_5 : generator power rate-of-change penalty; w_6 : tilt moment penalty; w_7 : yaw moment penalty. Bold numbers indicate varied weights. Abbreviations: CEMPC, convex EMPC; IPC, individual pitch control.

count in the FAST's setting. This periodic signal is reflected predominantly as static rotor moments in the tilt and yaw directions in the nonrotating frame, as indicated previously. Below-rated condition is disregarded from this simulation as operations in this region to avoid unnecessary acceleration in pitch motors wear and tear.

Several weight configurations, listed in Table 3.2, are considered to understand the behavior of the CEMPC-IPC under different prioritizations of economic objectives. Not all weights are relevant for load reduction, namely, $w_1 - w_3$ and w_5 ; thus, their values are fixed, whereas w_4 , w_6 , and w_7 are subject to changes later on in Sections 3.5.1.1 and 3.5.1.2. For all configurations, $w_1 = 100$, $w_2 = 50$, $w_3 = 10$, and $w_5 = 50$ are set. The weight w_1 is set to enforce the production of $P_g = P_{g,\text{rated}}$ during the operation at above-rated. The $\dot{P}_{\text{av},i}$ maximization weight w_2 is chosen to push the upper bound of (3.23), thereby expanding the range within which the decision variable $P_{r,i}$ may find its optimal value. As for w_3 , the chosen value is sufficient to regulate K_g whenever the generator excurses to kinetic energies higher than $K_{g,\text{rated}}$ by lowering P_r (see (3.5)), which is realized by increasing the collective pitch component of the blades. Under these weights for power control and speed regulation, comparisons between the proposed CEMPC-IPC and a basic CEMPC, as well as demonstrations of CEMPC-IPC behaviors under different w_4 , w_6 , and w_7 tuning are conducted in the subsequent subsections.

3.5.1.1 CEMPC-IPC and Basic CEMPC Comparison

In this subsection, the behavior of the proposed controller without and with load reduction is compared. The former resembles that of the original CEMPC [51], with the exception that neither local storage nor grid power delivery is considered for the sake of simplicity, which is obtained by a slight modification of the latter. The main modification is in the replacement of the v_i into rotor-effective wind speed (REWS) estimate $\hat{v}_{\text{RE}} = \sum_{i=1}^3 \hat{v}_i/3$. This is required to enforce equal $P_{r,i}$ for all blades, which, after variable conversion into β_i by the reverse pitch LUT Ψ in (3.32), results in collective pitching. No penalties on M_{tilt} and M_{yaw} are imposed in the CEMPC setting, that is, $w_6 = w_7 = 0$, to prevent individual pitching of this controller despite the use of \hat{v}_{RE} , since it is still possible to induce modest individual pitch activities as done for side-side tower damping [84]. As for the CEMPC-IPC, \hat{v}_i is re-utilized and the load mitigation weights for penalizing M_{tilt} and M_{yaw} are set to $w_6 = w_7 = 100$ so that $P_{r,i}$ can now actively steer these moments closer to 0 Nm. For both CEMPC and CEMPC-IPC, listed as Configuration 1 and Configuration 2 in Table 3.2, respectively, a fixed penalty on $\dot{P}_{r,i}$, that is, $w_4 = 50$ is selected. Figure 3.3 depicts the time-

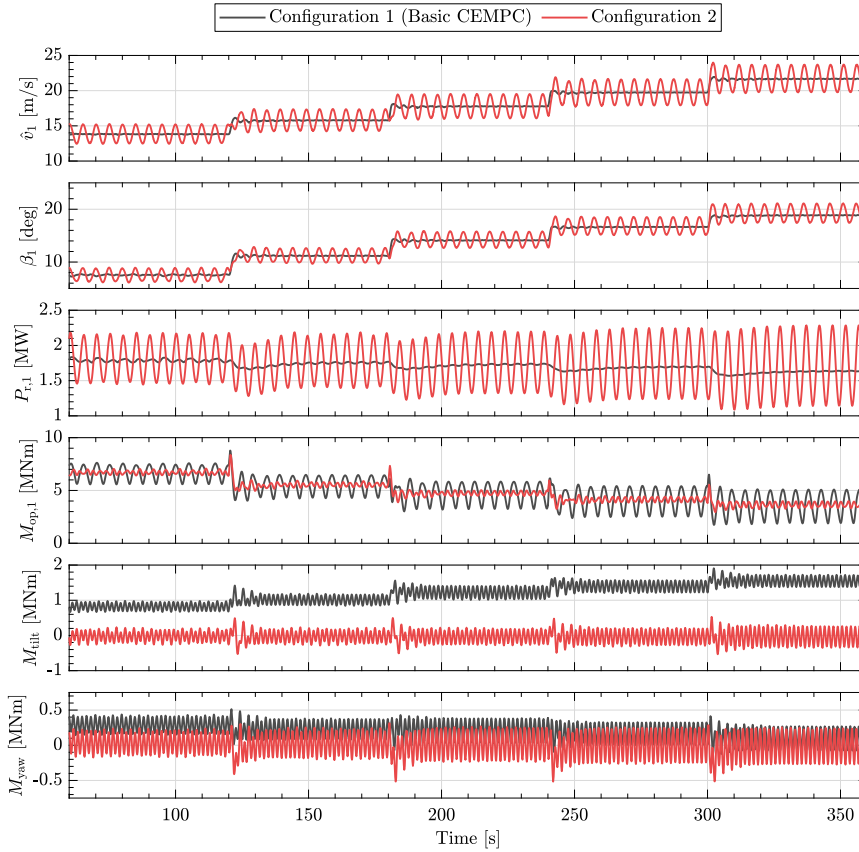


Figure 3.3: Step wind case time-marching simulation results of basic convex EMPC (CEMPC) under Configuration 1 and CEMPC-individual pitch control (IPC) under Configuration 2.

marching results of both the basic CEMPC (black lines) and CEMPC-IPC (red lines) under these configurations, with all blade-effective quantities only shown for the first blade, for the sake of clarity.

As shown in the figure, the basic CEMPC under Configuration 1 does not perform any individual pitching, as β_1 acts collectively with β_2 and β_3 only for speed regulation due to zero weights on w_6 and w_7 , as well as the utilization of v_{RE} . Also depicted is $P_{r,1}$ of the basic CEMPC, which appears to maintain its value of about 1.65–1.8 MW as a realization of an active overspeeding penalty. Under this benchmark configuration, the first OoP blade root bending moment $M_{op,1}$ experiences severe 1P loading in the rotating reference frame due to the wind shear and tower shadow effects, which, as the wind becomes faster, becomes more significant. Considerable deviation of the static components of M_{tilt} and M_{yaw} from 0 Nm is thus observed in the fixed frame as a consequence of this 1P load in the rotating frame. In comparison with CEMPC-IPC under Configuration 2, improvements in terms of fatigue load reduction are evident from the measurements of $M_{op,1}$, where fewer

1P oscillations are experienced. Consequently, M_{tilt} and M_{yaw} exhibit much less static loading compared to the previous configuration.

3.5.1.2 CEMPC-IPC Behavior under Different Aerodynamic Power Rate Penalties

Another aspect worth paying attention to is the CEMPC-IPC load reduction behavior under different penalties on $\dot{P}_{r,i}$, which is considered in this subsection. In a previous work [84], penalizing $\dot{P}_{r,i}$ was shown as a way to prevent excessive individual pitching, which consequently results in less tower load mitigation activity. To study how the penalization of $\dot{P}_{r,i}$ is affecting the blade loads in the current work, additional step wind simulations are performed, in which two different weight configurations for CEMPC-IPC are set, that is, Configuration 3 and Configuration 4. In the former and latter configurations, respectively, $w_4 = 100$ and $w_4 = 25$ are selected, representing high and low penalties on the $\dot{P}_{r,i}$, with the tilt and yaw moment penalties are set equally to $w_6 = w_7 = 10$. Figure 3.4 depicts the time-marching simulation results for both cases, where for the sake of clarity, only an excerpt of the measurements at $t = 175 - 275$ s is shown.

In the figure, CEMPC-IPC with Configuration 4 (red lines) clearly shows more active $P_{r,i}$ than Configuration 3 (black lines). This behavior is anticipated since w_4 is decreased in the former configuration, which enables $P_{r,i}$ to vary with higher magnitude. This results in β_i with slightly smaller oscillation but with reduced $M_{\text{op},i}$. The reduction in the blade loads is, again, reflected as a reduction in the static components of M_{tilt} and M_{yaw} , as evident in the figure. Such an observation might be counterintuitive as one might expect that decreased w_4 would give more aggressive pitching, as was demonstrated in the previous work [84]. Under constant \hat{v}_i (in that it does not vary periodically in 1P frequency) and constant K_g at above-rated, as considered in the previous work, one may find that a high $P_{r,i}$ variation also translates to a high variation of β_i computed by Ψ . This is not the case here since \hat{v}_i , being a varying signal at 1P due to the wind shear and tower shadow, has more influence on the computation of β_i , along with $P_{r,i}$ and K_g , which in the end creates lower β_i variation. Having the knowledge of such behavior at hand, trade-off tuning between pitch activities and load mitigation, being parts of the economic objectives of CEMPC-IPC, can thus be applied appropriately for other conditions, such as the following turbulence cases.

3.5.2 Turbulent Wind

In this case, several turbulent wind fields generated by NREL TurbSim [93] with the Kaimal turbulence model defined in the IEC 61400-3 standard [94] are employed, including wind shear and tower shadow as used previously. Two mean wind speeds at hub height are considered, namely $v_0 = 16$ m/s and $v_0 = 20$ m/s, where, for each mean speed, turbulence levels of $I_T = \{4, 8, 12, 16\}\%$ are simulated, making up of eight turbulence cases in total. For each turbulence case, a 660 s long simulation is run, from which only the last 600 s is evaluated such that FAST computational transients are not accounted for.

The tuning weights of the CEMPC-IPC in the current performance study are set on a case-per-case basis, taking into account the trade-off between loads reduction and pitch activities according to the observations from the previous wind case. These weights, tuned accordingly for each wind speed and turbulence condition, are provided in Table 3.3.

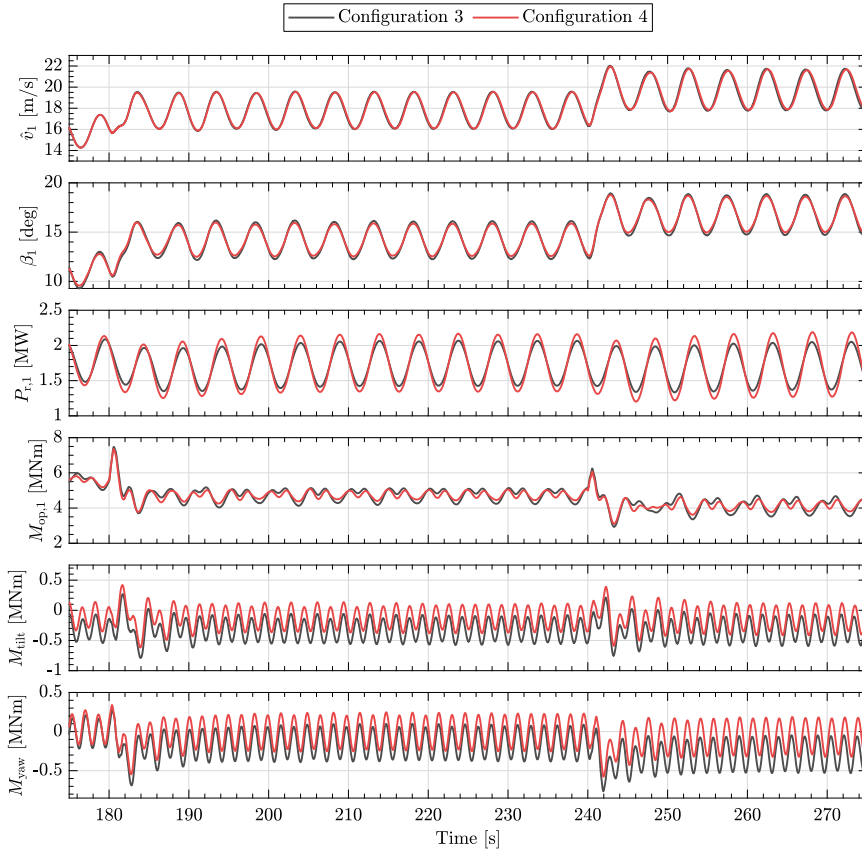


Figure 3.4: Step wind case time-marching simulation results of convex EMPC (CEMPC)-individual pitch control (IPC) under Configuration 3 and Configuration 4.

Table 3.3: CEMPC-IPC weight configurations for turbulent wind cases.

| Configuration | Turbulence case | w_1 | w_2 | w_3 | w_4 | w_5 | w_6 | w_7 |
|---------------|--|-------|-------|-------|------------|-------|-----------|-----------|
| 1 | $v_0 = 20$ m/s, $I_T = 16\%$ | 100 | 50 | 10 | 100 | 50 | 50 | 50 |
| 2 | $v_0 = 20$ m/s, $I_T = 8\%$ | 100 | 50 | 10 | 50 | 50 | 75 | 75 |
| 3 | $v_0 = 16$ m/s, $I_T = \{12, 16\}\%$ and $v_0 = 20$ m/s, $I_T = 12\%$ | 100 | 50 | 10 | 20 | 50 | 90 | 90 |
| 4 | $v_0 = 16$ m/s, $I_T = \{4, 8\}\%$ and $v_0 = 20$ m/s, $I_T = 4\%$ | 100 | 50 | 10 | 10 | 50 | 95 | 95 |

Weights description: w_1 : generator power maximization; w_2 : available power maximization; w_3 : overspeeding penalty; w_4 : aerodynamic power rate-of-change penalty; w_5 : generator power rate-of-change penalty; w_6 : tilt moment penalty; w_7 : yaw moment penalty. Bold numbers indicate varied weights.

Abbreviations: CEMPC, convex EMPC; IPC, individual pitch control.

The performance of CEMPC-IPC in the current turbulent scenarios is compared with a baseline conventional Coleman-based IPC [15, 70], operating alongside a standard K-omega-squared controller and gain-scheduled collective pitch control (CPC)

for torque control and rotational speed regulation, respectively [26]. The conventional IPC employed in this work is a pair of pure integrators with equal gains $K_{I,\text{tilt}} = K_{I,\text{yaw}} = 2.6604 \cdot 10^{-9}$ rad/Nm, for canceling out the static components of rotor moments M_{tilt} and M_{yaw} , as computed in (3.14) and (3.15). The gains are chosen based on the frequency domain loop-shaping method so as to obtain 0.15 rad/s crossover frequency. The pitch demands β_{tilt} and β_{yaw} generated by these integrators in the fixed frame, together with the collective pitch signal β_{col} used in CPC, are reconstructed into β_i , by the following reverse Coleman transformation

$$\beta_i(t) = \beta_{\text{col}}(t) + \beta_{\text{tilt}}(t) \cos(\psi_i(t) + \psi_{\text{off}}) + \beta_{\text{yaw}}(t) \sin(\psi_i(t) + \psi_{\text{off}}), \quad (3.42)$$

with ψ_{off} being an azimuth offset to compensate for the coupling between the tilt and yaw axes. For the considered operating points, $\psi_{\text{off}} = 17.5^\circ$ is chosen such that the cross-coupling between the tilt and yaw axes is minimized. As the integrator gains needed to reach the aforementioned crossover frequency, as well as the azimuth offset for decoupling both fixed axes, do not vary too much at the above-rated, a gain-scheduling strategy is deemed unnecessary. The reader interested in the detailed implementation of the baseline IPC with azimuth offset inclusion as a decoupling strategy is referred to the work of Mulders et al [70].

A number of performance indicators are used for assessing the load reduction quality and also blade pitching activities for the baseline controller, without and with IPC, and the designed CEMPC-IPC as follows

1. Mean standard deviation of OoP blade root bending moments

$$\sigma_{M_{\text{op},123}} = \sum_{i=1}^3 \sigma(M_{\text{op},i})/3,$$

2. Standard deviation of the low-speed-shaft (LSS) bending moment in the rotating frame

$$\sigma_{M_{\text{lss}}} = \sigma(M_{\text{lss}}),$$

3. Standard deviation of the yaw bearing yaw moment in the fixed frame

$$\sigma_{M_{\text{yb}}} = \sigma(M_{\text{yb}}),$$

4. Cumulative pitch distance traveled by the blades [95]

$$\beta_{\text{tot}} = \sum_k \sum_{i=1}^3 |\Delta\beta_i(k)|,$$

where $\Delta\beta_i(k) = \beta_i(k) - \beta_i(k-1)$.

The moments considered in the standard deviations represent those of the actual wind turbine components, where load sensors are installed in the field [15, 40, 95], in contrast to M_{tilt} and M_{yaw} , which are projections of $M_{\text{op},i}$ and not from actual components. Note

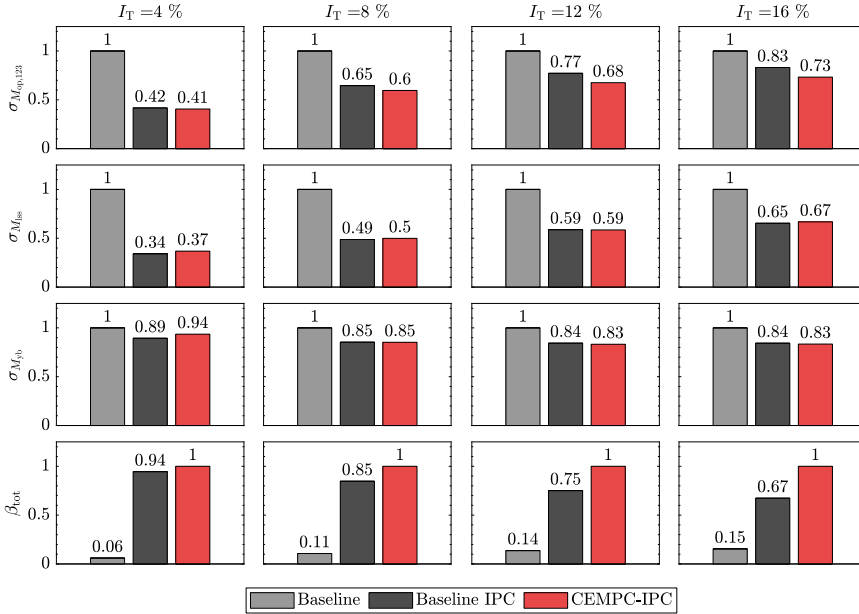


Figure 3.5: Normalized bending moments standard deviations of multiple wind turbine components and cumulative pitch travel for turbulence cases for mean hub height wind speed $v_0 = 16$ m/s.

that since simulation data of only 10 min for each turbulence case are considered, therefore, standard deviations of load measurements are preferred to evaluate the damage reduction of different wind turbine components³.

The performance indicators data computed for all of the turbulence cases are collected in Table A.1 in Appendix A, where, for convenience, their normalized values are depicted as comparative bar graphs in Figure 3.5 for $v_0 = 16$ m/s. In the figure, the standard deviations of the aforementioned bending moments and β_{tot} are normalized with respect to either the baseline controller without IPC or CEMPC-IPC, where appropriate, for better readability of the bar heights. Since similar conclusions can be drawn for turbulent cases of $v_0 = 20$ m/s, their bar graphs are not presented for brevity.

In Figure 3.5, some trends in the load reduction performance of the CEMPC-IPC at $v_0 = 16$ m/s can be observed. It is apparent that, generally, similar performance in the reduction of the $\sigma_{M_{ss}}$ and $\sigma_{M_{yb}}$ with respect to the baseline IPC is attained by the CEMPC-IPC for all turbulence intensities. More interestingly, as the turbulence intensity goes higher, the proposed controller performs better than the baseline IPC in terms of reduction in $\sigma_{M_{op,123}}$, from only 1% lower at $I_T = 4\%$ to 10% lower at $I_T = 16\%$. These improvements are linked with the increase in the pitch activities indicated by β_{tot} ranging from 6% to 33% higher than the baseline IPC.

Excerpts of time series results for both $v_0 = 16$ m/s and $v_0 = 20$ m/s wind speeds are pro-

³For a more accurate assessment, damage equivalent load may also be employed; however, this requires more simulation data, thus, for simplicity is not considered in the current work.

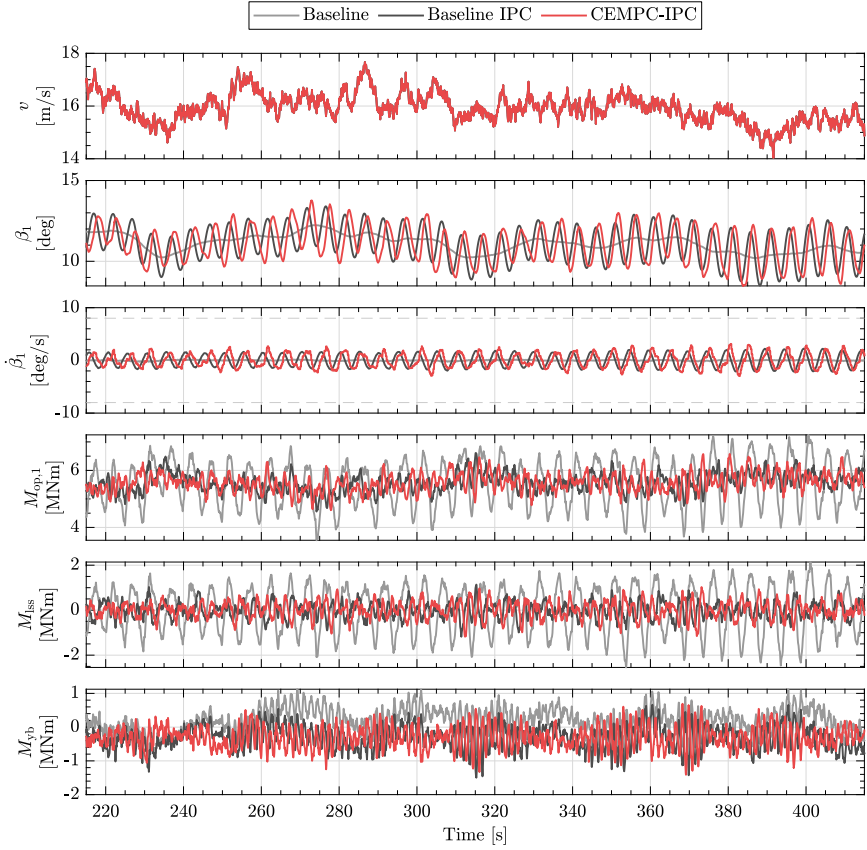


Figure 3.6: Excerpt of the time series simulation results of $v_0 = 16$ m/s for $I_T = 4\%$ for $t = 215 - 415$ s.

vided, in which the records of v at hub height, β_1 , $\dot{\beta}_1$, $M_{op,1}$, M_{1ss} , and M_{yb} measurements are shown. In Figure 3.6, results from the scenario $v_0 = 16$ m/s under a low-turbulence case of $I_T = 4\%$ are depicted. It is shown that both the proposed CEMPC-IPC (red lines) and baseline IPC (black lines) are able to significantly reduce the fatigue loads $M_{op,1}$, M_{1ss} , and M_{yb} experience with respect to those of by the baseline controller (gray lines). Similar pitching activities are seen between both IPC controllers, with slightly higher $\dot{\beta}_1$ for CEMPC-IPC, which shows consistency with β_{tot} evaluation indicated by the bar graphs in Figure 3.5. Also shown are the pitch rate limits $\dot{\beta}_{max} = -\dot{\beta}_{min} = 8^\circ/s$ as straight, dashed gray lines, which are not exceeded by both IPC controllers.

In Figure 3.7, the power spectral density (PSD) results of β_1 , $M_{op,1}$, M_{1ss} , and M_{yb} from the same turbulence case are presented, which are obtained based of Welch's power spectrum estimation method [96]. From the figure, a visible reduction in the 1P component of $M_{op,1}$ at 0.2 Hz can be clearly seen for both the CEMPC-IPC and baseline IPC, with the former method also resulting in a reduction at lower frequencies. In the measurements of the rotating M_{1ss} , the 1P component in the signals can be better observed due to the

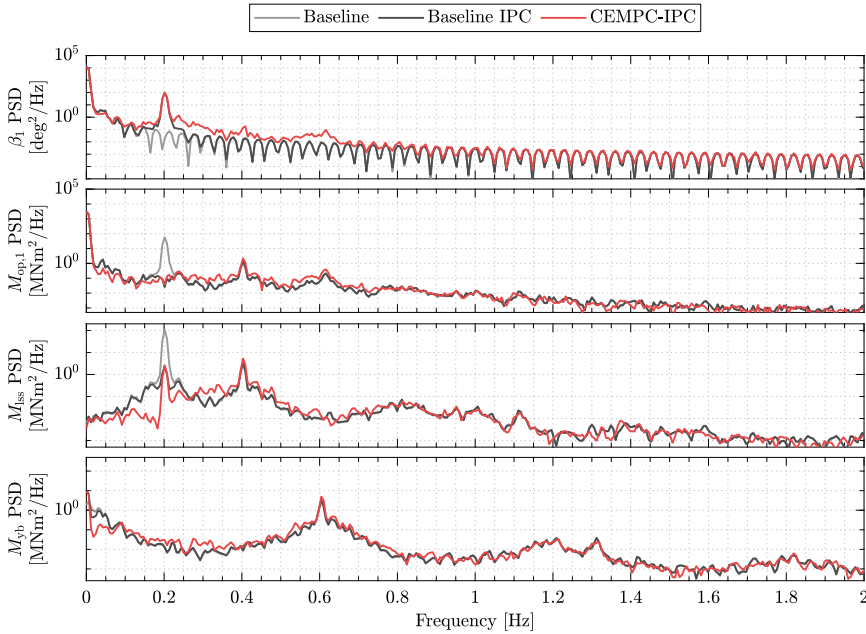


Figure 3.7: Power spectral density results for various wind turbine components of $v_0 = 16$ m/s for $I_T = 4\%$.

low-frequent load components of the blades canceling each other out. Here, the reduction of the 1P loads is more evident, with the low-frequency contents between 0.1-0.2 Hz being further lowered by the CEMPC-IPC. However, the increase in the spectral densities at frequencies surrounding 0.3 Hz counterbalances the reduction obtained at the lower frequencies, which may explain why $\sigma_{M_{ss}}$ of this controller is close to that of the baseline IPC, as shown in Figure 3.5. The PSD results of β_1 indicate consistency with β_{tot} evaluated previously, in the sense that CEMPC-IPC exercises higher pitching activities with respect to the baseline IPC, particularly between 1P and 0.65 Hz.

In Figure 3.8, time domain signals for the case $v_0 = 20$ m/s with $I_T = 16\%$ are depicted. Here, the CEMPC-IPC again showcases its capability in reducing the loads experienced by $M_{op,1}$, as well as M_{ss} and M_{yb} , for instance, at $t = 200 - 220$ s and $t = 300 - 320$ s. The pitch system of the proposed controller is also more active as the turbulence level becomes higher. At times, β_i might violate the pitch rate limits as shown between $t = 300$ and 310 s, since the current implementation of the CEMPC-IPC does not take into account explicitly pitch rate constraints; thus, room for future improvement.

Figure 3.9 illustrates the PSDs of the simulation results for the same turbulence case, from which a conclusion similar to that of the previous case's PSDs can be drawn. One noticeable difference is in the increase of the spectral content of β_1 for frequencies of about 0.1 Hz until approximately 1 Hz. This can be explained as follows. The increase in turbulence level is reflected as an increase in the overall frequency components in the wind. This information is carried over into the CEMPC-IPC via \hat{v}_i , which is also utilized by Ψ to obtain the optimal pitch angles, thereby giving rise to the pitch spectral content.

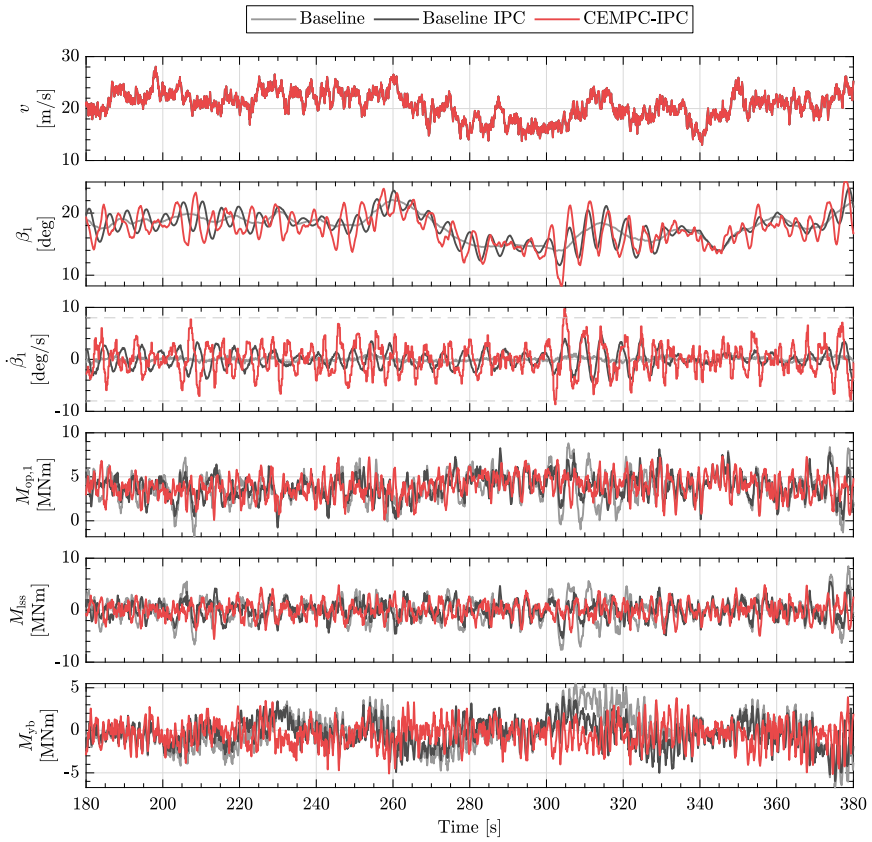


Figure 3.8: Excerpt of the time series simulation results of $v_0 = 20$ m/s for $I_T = 16\%$ for $t = 180 - 380$ s.

This might also explain the necessity to use different weight combinations for different turbulence levels to obtain comparable results with respect to the baseline IPC. Investigating further the effects of different Coleman BEWS tuning parameters on the CEMPC-IPC weighting may be of interest for future study.

In light of the presented results, the CEMPC-IPC appears to perform comparably to the baseline IPC. However, this work is preliminary and mainly aimed at extending the fatigue loads mitigation capability of the CEMPC framework [51, 84], with a focus on blade loads. Improvements to maximize the potential of CEMPC-IPC may be achieved in future work, for instance, by augmenting a more accurate internal model and including a preview wind information so that better predictive capability of the controller can be attained. Another aspect worth looking for is the inclusion of pitch rate constraints to have better handling of the pitch drive mechanism.

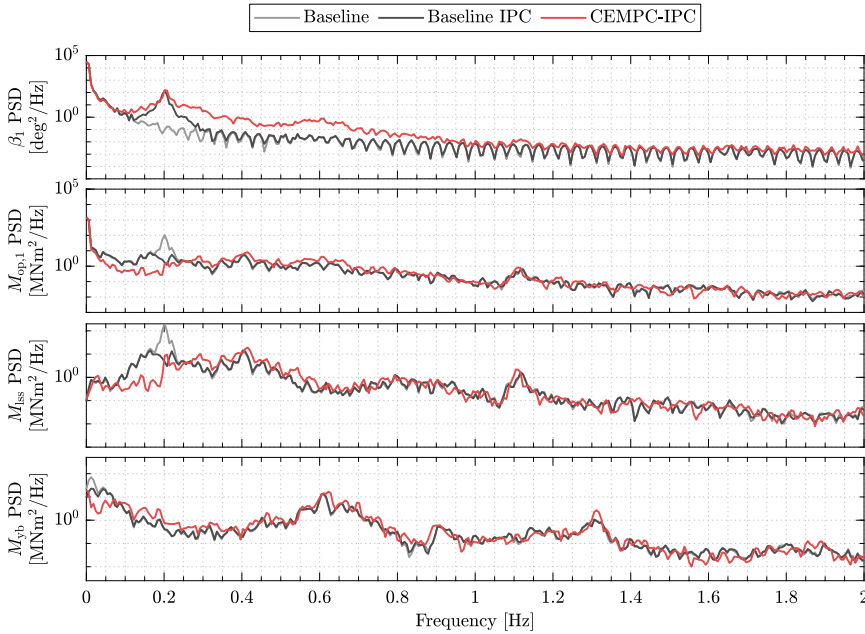


Figure 3.9: Power spectral density results for various wind turbine components of $v_0 = 20$ m/s for $I_T = 16\%$.

3.6 Conclusions

In this chapter, a novel CEMPC-IPC method has been developed with blade loads alleviation capability, thereby extending the family of CEMPC controllers for wind turbine applications. The convexity of the proposed controller is made possible by the reformulation of a simplified wind turbine model in terms of power and energy flows, such that linear dynamics, convex constraints, and concave objective functions (to be maximized), embodied in an OCP, are obtained. Having such a convex OCP formulated, a globally optimal solution (with respect to the internal model and available measurement and estimation data) is guaranteed and real-time deployment becomes possible. The individual pitching capability of this framework is unlocked by the utilization of multiple aerodynamic powers—each representing that of an individual blade, in contrast to employing a single, rotor-effective quantity. Such individual aerodynamic powers are then used to substitute nominal turbine variables in the static blade forces and moments formulation. By including moment penalizations as part of the OCP's economic objectives, the pitching movement of the individual blades can now be controlled to mitigate wind turbine blade loads. Moreover, the proposed framework allows for trade-off tuning between different economic objectives with ease. For supplying unknown and unmeasurable information into the CEMPC-IPC, the load-sensing Coleman BEWS estimator and UKF moment biases estimator have been incorporated. Numerical simulations under the mid-fidelity NREL FAST environment have been conducted, both in step wind and turbulent wind cases, in which the performance of the CEMPC-IPC has been evaluated. Compared with a conventional IPC, the proposed method has been shown to yield similar performance in terms

of mitigating OoP blade root bending moments, as well as rotating LSS and fixed yaw bearing yaw moments. The load-reducing capability of the proposed CEMPC-IPC thus, in conclusion, has shown the potential to prolong wind turbine lifetime, such that further economic benefit from its power-generating operations can be gained. To push the limit of the novel CEMPC-IPC, future work may consider improvements in internal model accuracy, incorporation of preview wind information, and incorporation of pitch rate constraints for better handling of pitching activities.

4

Periodic Load Estimation of a Wind Turbine Tower using a Model Demodulation Transformation

4

The ever-increasing power capacities of wind turbines promote the use of tall and slender turbine towers. This poses a challenge from a fatigue loading perspective by the relocation of the first and lightly-damped tower side-side natural frequency into the turbine operating regime, promoting its excitation during nominal operation. The excitation of this resonance can be aggravated by periodic loading in the presence of rotor mass and/or aerodynamic imbalance. Earlier work already presented a method to prevent the side-side excitation using a combination of model demodulation and quasi-linear parameter varying model predictive control techniques. However, the method does not incorporate features for active control for side-side load mitigations. Because the information of the beforementioned periodic side-side loading is unknown and unmeasurable in practical scenarios, this chapter presents a Kalman filtering method for its estimation in a demodulated fashion. The Kalman filter employs an extended demodulated wind turbine model augmented with random walk models of the periodic load. The simulation result demonstrates the effectiveness of the proposed method in estimating the periodic load components along with unmeasurable tower states in their demodulated form. These estimates pose an opportunity for use in future advanced controller designs for active load reductions.

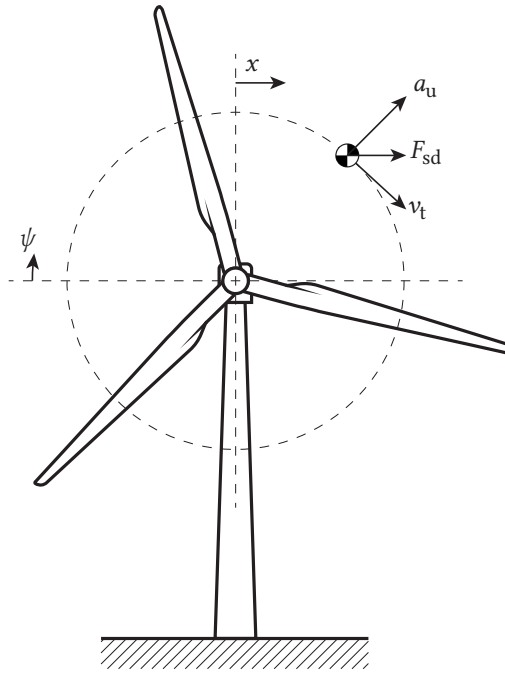


Figure 4.1: A wind turbine excited at the side-side direction by a periodic load due to the rotor imbalance $F_{sd}(t) = a_u \cos(\psi(t))$ at the 1P frequency. The tangential speed of the periodic load is indicated by v_t , and x denotes tower top displacement in the horizontal direction.

4

4.1 Introduction

A prevalent strategy to achieve cost-competitive wind energy generation systems is to upscale wind turbine sizes. Having taller tower and longer blade designs allows wind turbines to, respectively, access higher wind speeds and have a greater rotor swept area, such that more wind energy can be harnessed [13].

Taller turbine towers are typically more flexible due to decreased wall thickness, which could impose fatigue loading challenges [14]. Such towers can be excited more easily and severely as their first natural frequency may enter the rotor operating regime. The risk of resonance by the once-per-revolution (1P) frequency (i.e., the rotor rotational frequency) is thus becoming more prominent, particularly in the side-side direction as the aerodynamic damping is negligible [13]. Fig. 4.1 shows that a rotor mass and/or aerodynamic imbalance can form a persistent *periodic load/disturbance*, possibly exciting and exacerbating the side-side resonance [35].

To prevent prolonged operation at the tower resonant frequency, a possible solution is to implement the so-called *frequency skipping* logic in the controller design by manipulation of generator torque [30, 35]. However, implementing such a rotational speed exclusion method has no convenient and inherent way of tuning and can therefore significantly affect power production. This problem advocates the use of an advanced control method that can cater for the power maximization and fatigue load minimization trade-off.

Recently, such an advanced and novel quasi-linear parameter varying (qLPV) control framework has been developed incorporating the aforementioned frequency skipping strategy with the capability to address the power-fatigue trade-off [53]. In this framework, a *model demodulation transformation*, brought from the field of precision mechatronics [54], is used to extract a slow-varying content of a signal from its higher-frequency *carrier*. In the previous work, the model demodulation method is applied to transform the wind turbine tower dynamics, so as to obtain an affine qLPV model scheduled on the rotor rotational frequency. The result enabled the use of a computationally attractive qLPV model predictive control (MPC) algorithm [55] by virtue of the obtained convex optimal control problem.

Frequency-skipping control prevents operation in a critical rotational speed range for extended periods of time. Still, load mitigation capabilities could be further enhanced by incorporating active damping features in the same qLPV-MPC framework, thus rejecting the periodic load. The estimation of the periodic disturbance via demodulation would benefit the realization of such an active load control framework. The development of an unknown input observer to estimate the demodulated load is the main contribution of this chapter.

To aid the former mentioned estimation of demodulated disturbance, a demodulated system description of the tower side-side dynamics, extended from [53], is provided in this work. Specifically, the extended model description now includes (i) both the slowly-varying periodic excitation amplitude and phase offset; (ii) the effect of the generator torque on the tower motion; and (iii) the demodulated tower acceleration in the output equation. Based on this model, we propose a Kalman filter (KF) design, in which *random walk* models of the unknown periodic load components are augmented to the state equation. This allows their estimates to be obtained alongside the unmeasurable tower states, such as velocity and displacement, in a demodulated manner. Future control methods may benefit from the estimates by active load mitigations induced by the periodic disturbance, e.g., in the predictive framework of [53].

The remainder of this chapter is structured as follows. Section 4.2 describes the nominal wind turbine dynamics, comprising that of the tower side-side motion and the drivetrain. Section 4.3 revisits the demodulated wind turbine model derivation along with its extension. The proposed KF design is elaborated upon in Section 4.4, the performance of which is examined in several case studies in Section 4.5 along with the validation of the extended model. Finally, in Section 4.6, conclusions are drawn and future prospects for active damping control purposes are given.

4.2 Nominal Wind Turbine Model

The dynamics of a wind turbine tower are often described as a second-order mass-spring-damper system with a forcing term, and are given by the following state equation

$$\begin{bmatrix} \dot{x}_1(t) \\ \dot{x}_2(t) \end{bmatrix} = \begin{bmatrix} -d/m & -k/m \\ 1 & 0 \end{bmatrix} \begin{bmatrix} x_1(t) \\ x_2(t) \end{bmatrix} + \begin{bmatrix} 1/m \\ 0 \end{bmatrix} F_{sd}(t), \quad (4.1)$$

where m , d , and k , are the (first) modal mass, damping, and stiffness of the tower in the side-side direction, respectively. The tower top velocity and displacement are respectively

represented by x_1 and x_2 . The symbol t denotes the quantities of the fast-varying time scale as explained in the next section, and the $(\dot{\cdot})$ -notation indicates the first time-derivative of the specified signal.

The side-side force F_{sd} in (4.1) (and Fig. 4.1) is originally considered to be purely affected by a centrifugal force in the work of Mulders, et al. [53] and modeled as the following periodic signal

$$F_{sd}(t) = a_u \cos(\psi(t)), \quad (4.2)$$

with a_u as the (constant) magnitude of the excitation. The rotor azimuth ψ is defined as the angular travel of the first blade with respect to its vertically upward position. Note that the relation $\psi(t) = \int \omega_r(t) dt$ holds, with ω_r as the angular velocity of the rotor, which determines the frequency of the periodic excitation.

4

Remark 3 *Although F_{sd} in (4.2) only contains a periodic load, this does not imply that other forcing effects, such as those static in nature, cannot be accounted for. That is, F_{sd} is considered as a generic force throughout this work.*

Remark 4 *The tower states x_1 and x_2 , as well as their time derivatives, can be decomposed into their slow- and fast-varying components, as will be made clearer in the next section. The former exhibits quasi-steady-state behavior, whereas this is not the case with the latter, especially if persistent periodic loading affects the system.*

The tower dynamics are augmented with the following simplified representation of the complete drivetrain dynamics

$$\dot{\omega}_r(t) = \frac{T_a(t) - GT_g(t)}{J_r}, \quad (4.3)$$

where J_r , G , and T_g are the low-speed-shaft (LSS) equivalent inertia, gearbox ratio (≥ 1) and generator torque, respectively. The aerodynamic torque is defined as

$$T_a(t) = \frac{1}{2} \rho_a \pi R^3 C_q(\omega_r(t), v(t), \beta(t)) v(t)^2,$$

with ρ_a , R , C_q , v , and β as the air density, rotor radius, aerodynamic torque coefficient, wind speed, and pitch angle, respectively.

Assumption 4 *Throughout this study, the perfect knowledge of the aerodynamic torque T_a and wind speed v is assumed since this chapter focuses on estimating the unknown periodic disturbance; in realistic scenarios, these quantities can be estimated by an observer [65].*

4.3 Extended Demodulated Model

The concept of model demodulation transformation was originally formulated to overcome the challenges surrounding the derivation of transient dynamic model of cantilevers in tapping mode atomic force microscopy (TM-AFM) [54]. The transformation is able to separate the slow- and fast-varying components of the states in a standard state-space form, thereby facilitating (model-based) controller design. The reader is referred to the

work of Keyvani, et al. [54] for an extensive explanation and derivation of the model demodulation technique with an application to TM-AFM.

The technique was subsequently adopted by Mulders, et al. [53] to model the wind turbine tower dynamics in a demodulated fashion, enabling frequency skipping control capabilities in a predictive control framework. This section first revisits the model demodulation transformation, and secondly proposes extensions by the inclusion of generator torque signal affecting the tower side-side motion, and derives an output equation incorporating tower acceleration components and rotor speed.

The following key assumption underlies model demodulation [54].

Assumption 5 *The changes in the amplitude and phase of the system's response are much slower than a single oscillation cycle $T_r \triangleq 2\pi/\omega_r$. Accordingly, signals of slow time-varying time scale are indicated with the notation τ , whereas its fast-varying counterpart with t .*

As per the above assumption, variables belonging to the slow time scale can be treated as constant over T_r such that

$$\int_0^{T_r} f(\tau)g(t) dt = f(\tau) \int_0^{T_r} g(t) dt,$$

f and g being generic variables at different time scales.

Using Euler's formula $e^{j\sigma} = \cos(\sigma) + j \sin(\sigma)$, the state variables of the wind turbine can be written as

$$\begin{aligned} x_i(t) &= a_i(\tau) \cos(\omega_r(\tau)t + \phi_i(\tau)), \\ \Leftrightarrow x_i(t) &= \Re\{X_i(\tau)e^{j\omega_r(\tau)t}\}, \end{aligned} \quad (4.4)$$

with $X_i(\tau) = a_i(\tau)e^{j\phi_i(\tau)} \in \mathbb{C}$, where the subscript i is an index. The $\Re\{\cdot\}$ -notation corresponds to the real component of the considered variable, while the $\Im\{\cdot\}$ -notation refers to that of the imaginary part, as used later on in the derivation. Note that to reconstruct the signal's amplitude and phase offset, the following relations are used respectively

$$a_i(\tau) = \sqrt{\Re\{X_i(\tau)\}^2 + \Im\{X_i(\tau)\}^2}, \quad (4.5)$$

$$\phi_i(\tau) = \arctan(\Im\{X_i(\tau)\}/\Re\{X_i(\tau)\}). \quad (4.6)$$

The first time-derivative of (4.4) is given by

$$\dot{x}_i(t) = \Re\left\{\left(\dot{X}_i(\tau) + j\omega_r(\tau)X_i(\tau)\right) e^{j\omega_r(\tau)t}\right\}. \quad (4.7)$$

The side-side force in (4.2) is extended to include an unknown slow time-varying phase offset of the periodic load ϕ_u since, in reality, the load might not be in-phase with the rotor azimuth. Moreover, a_u is now considered to be slowly-varying rather than a constant; further generalizing the periodic load characteristic. By adding the contribution of T_g in the form of a static contribution to the tower dynamics, the side-side force becomes

$$F_{sd,ext}(t) = a_u(\tau) \cos(\omega_r(\tau)t + \phi_u(\tau)) + c T_g(t), \quad (4.8)$$

thereby extending the side-side force as formulated in [53]. The scaling factor $c = 3/2H$ represents the ratio between angular and translational displacement of the tower motion, here assumed as a prismatic beam [63], with H being the tower height.

The demodulation of the side-side force is performed by considering it as a *semi-periodic signal*, i.e., a harmonic signal with slowly varying amplitude and phase. Broken down into its *semi-harmonic components* in a similar fashion as (4.4), (4.8) can be rewritten as follows

$$F_{\text{sd,ext}}(t) = \Re \left\{ A_{\text{u}}(\tau) e^{j\omega_r(\tau)t} + c \sum_{n=0}^{\infty} T_{\text{g}}^{(n)}(\tau) e^{jn\omega_r(\tau)t} \right\}, \quad (4.9)$$

with $A_{\text{u}}(\tau) = a_{\text{u}}(\tau) e^{j\phi_{\text{u}}(\tau)} \in \mathbb{C}$ representing the slow-varying component of the periodic load signal. The amplitude and phase of the n -th harmonic component of the generator torque signal is denoted by $T_{\text{g}}^{(n)}(\tau) \in \mathbb{C}$.

Substituting (4.4), (4.7), and (4.9) into (4.1) yields the relations

$$\Re \left\{ \left(\dot{X}_1(\tau) + j\omega_r(\tau)X_1(\tau) + \frac{d}{m}X_1(\tau) + \frac{k}{m}X_2(\tau) - \frac{1}{m}A_{\text{u}}(\tau) \right) e^{j\omega_r(\tau)t} - \frac{c}{m} \sum_{n=0}^{\infty} T_{\text{g}}^{(n)}(\tau) e^{jn\omega_r(\tau)t} \right\} = 0, \quad (4.10)$$

and

$$\Re \left\{ (\dot{X}_2(\tau) + j\omega_r(\tau)X_2(\tau) - X_1(\tau)) e^{j\omega_r(\tau)t} \right\} = 0. \quad (4.11)$$

Multiplying both sides of (4.10) and (4.11) with $e^{j\omega_r(\tau)t}$ and integrating over an oscillation period $\int_0^{T_r} (\cdot) e^{j\omega_r(\tau)t} dt$ results in the following projections into the space of the first harmonic component

$$\int_0^{T_r} \Re \left\{ \left(\dot{X}_1(\tau) + j\omega_r(\tau)X_1(\tau) + \frac{d}{m}X_1(\tau) + \frac{k}{m}X_2(\tau) - \frac{1}{m}A_{\text{u}}(\tau) - \frac{c}{m}T_{\text{g}}^{(1)}(\tau) \right) e^{j\omega_r(\tau)t} \right\} e^{j\omega_r(\tau)t} dt = 0, \quad (4.12)$$

and

$$\int_0^{T_r} \Re \left\{ (\dot{X}_2(\tau) + j\omega_r(\tau)X_2(\tau) - X_1(\tau)) e^{j\omega_r(\tau)t} \right\} e^{j\omega_r(\tau)t} dt = 0. \quad (4.13)$$

It is important to note that in (4.12), due to the following orthogonality property of harmonic functions

$$\int_0^{2\pi} \Re \{ \gamma e^{jn\theta} \} e^{j\theta} d\theta = 0, \quad \forall n \neq 1, \quad (4.14)$$

only the first harmonic of $T_{\text{g}}^{(n)}$, that is $T_{\text{g}}^{(1)}$, is left in the equation while those corresponding to zeroth and higher harmonics are cancelled.

Another orthogonality property of harmonic functions which can be exploited is

$$\int_0^{2\pi} \Re \{ \gamma e^{j\theta} \} e^{j\theta} d\theta = 0, \quad \text{iff } \gamma \in \mathbb{C} = 0, \quad (4.15)$$

by which the following state equation is obtained

$$\begin{bmatrix} \dot{X}_1 \\ \dot{X}_2 \end{bmatrix} = \begin{bmatrix} -j\omega_r - \frac{d}{m} & -\frac{k}{m} \\ 1 & -j\omega_r \end{bmatrix} \begin{bmatrix} X_1 \\ X_2 \end{bmatrix} + \begin{bmatrix} \frac{1}{m} & \frac{c}{m} \\ 0 & 0 \end{bmatrix} \begin{bmatrix} A_u \\ T_g^{(1)} \end{bmatrix}, \quad (4.16)$$

with ω_r as the scheduling variable. For the sake of simplicity, the notation τ is dropped in the above equation and for the remainder of this chapter.

4.3.1 Extended Demodulated State Equation

As a step toward obtaining a qLPV representation of the combined drivetrain and demodulated tower dynamics, (4.16) is augmented with (4.3). However, it is important to realize that this equation contains several complex terms, hindering it from being directly usable for control system designs. Therefore, the equation is rewritten by separating the real or imaginary parts by defining the new states $q_1 = \Re\{X_1\} \in \mathbb{R}$, $q_2 = \Im\{X_1\} \in \mathbb{R}$, $q_3 = \Re\{X_2\} \in \mathbb{R}$, and $q_4 = \Im\{X_2\} \in \mathbb{R}$, forming the following extension of the demodulated state equation with respect to that of Mulders, et al. [53]

$$\underbrace{\begin{bmatrix} \dot{q}_1 \\ \dot{q}_2 \\ \dot{q}_3 \\ \dot{q}_4 \\ \dot{\omega}_r \end{bmatrix}}_{\dot{\mathbf{x}}} = \underbrace{\begin{bmatrix} -\frac{d}{m} & \omega_r & -\frac{k}{m} & 0 & 0 \\ -\omega_r & -\frac{d}{m} & 0 & -\frac{k}{m} & 0 \\ 1 & 0 & 0 & \omega_r & 0 \\ 0 & 1 & -\omega_r & 0 & 0 \\ 0 & 0 & 0 & 0 & 0 \end{bmatrix}}_{\mathbf{A}(\rho)} \underbrace{\begin{bmatrix} q_1 \\ q_2 \\ q_3 \\ q_4 \\ \omega_r \end{bmatrix}}_{\mathbf{x}} + \underbrace{\begin{bmatrix} \frac{c}{m} & 0 & 0 \\ 0 & \frac{c}{m} & 0 \\ 0 & 0 & 0 \\ 0 & 0 & 0 \\ 0 & 0 & \frac{1}{J_r} \end{bmatrix}}_{\mathbf{B}_u} \underbrace{\begin{bmatrix} \Re\{T_g^{(1)}\} \\ \Im\{T_g^{(1)}\} \\ T_a - GT_g \end{bmatrix}}_{\mathbf{u}} + \underbrace{\begin{bmatrix} \frac{1}{m} & 0 \\ 0 & \frac{1}{m} \\ 0 & 0 \\ 0 & 0 \\ 0 & 0 \end{bmatrix}}_{\mathbf{B}_d} \underbrace{\begin{bmatrix} \Re\{A_u\} \\ \Im\{A_u\} \end{bmatrix}}_{\mathbf{d}}, \quad (4.17)$$

with the symbols \mathbf{x} , \mathbf{u} , and \mathbf{d} referring to the state, input, and disturbance vectors. $\mathbf{A}(\rho)$, \mathbf{B}_u , and \mathbf{B}_d are the (parameter-dependent) state, input, and disturbance matrices, respectively, with the scheduling variable $\rho = \omega_r$.

4.3.2 Output Equation Derivation

Following the derivation of the new state equation, the output of the demodulated wind turbine model may now be defined. In [53], the output was chosen as the displacement signal, following [54]. However, in reality, this signal is unavailable from the wind turbine measurements. In this work, a step toward obtaining a more realistic model is taken by defining the demodulated acceleration signal, which was not discussed in [53, 54], as the new output.

The acceleration signal in the demodulated fashion is calculated according to (4.7) for $i = 1$ as follows

$$q_a + jq_b = \dot{X}_1 + j\omega_r X_1, \quad (4.18)$$

with $q_a = \Re\{\dot{X}_1 + j\omega_r X_1\} \in \mathbb{R}$ and $q_b = \Im\{\dot{X}_1 + j\omega_r X_1\} \in \mathbb{R}$. By substitution of \dot{X}_1 from the state equation (4.16) into (4.18), the demodulated acceleration is obtained. Appending ω_r

as another output, the final output equation is thus

$$\underbrace{\begin{bmatrix} q_a \\ q_b \\ \omega_r \end{bmatrix}}_{\mathbf{y}} = \underbrace{\begin{bmatrix} -\frac{d}{m} & 0 & -\frac{k}{m} & 0 & 0 \\ 0 & -\frac{d}{m} & 0 & -\frac{k}{m} & 0 \\ 0 & 0 & 0 & 0 & 1 \end{bmatrix}}_{\mathbf{C}} \underbrace{\begin{bmatrix} q_1 \\ q_2 \\ q_3 \\ q_4 \\ \omega_r \end{bmatrix}}_{\mathbf{x}} + \underbrace{\begin{bmatrix} \frac{c}{m} & 0 & 0 \\ 0 & \frac{c}{m} & 0 \\ 0 & 0 & 0 \end{bmatrix}}_{\mathbf{D}_u} \underbrace{\begin{bmatrix} \Re\{T_g^{(1)}\} \\ \Im\{T_g^{(1)}\} \\ T_a - GT_g \end{bmatrix}}_{\mathbf{u}} + \underbrace{\begin{bmatrix} \frac{1}{m} & 0 \\ 0 & \frac{1}{m} \\ 0 & 0 \end{bmatrix}}_{\mathbf{D}_d} \underbrace{\begin{bmatrix} \Re\{A_u\} \\ \Im\{A_u\} \end{bmatrix}}_{\mathbf{d}}. \quad (4.19)$$

The output vector and matrix are denoted by \mathbf{y} and \mathbf{C} and the feedthrough matrices \mathbf{D}_u and \mathbf{D}_d correspond to that of the system's inputs and disturbances, respectively.

4.3.3 Measurement Signal Demodulation

In the real wind turbine system, measurement signals (e.g., tower acceleration), as well as control inputs, (e.g., generator torque), are not presented in their demodulated form. Hence, these signals need to be processed by a *measurement signal demodulation* (MSD) such that their 1P component can be obtained and used with the extended demodulated model derived in the preceding sections. Here, the method for demodulating measurement signal as presented by Bottasso, et al. [97] is employed and briefly summarized in the following. For further details, please consult [97].

The demodulation of a discrete signal $\hat{z}(t_k)$ with $t_k = k\Delta t$ over N_R revolutions is expressed as

$$\hat{z}(t_k) = \hat{z}(\psi(t_k)) \approx z_K^0 + \sum_{n=1}^{N_B} \left(z_{c,K}^{(n)} \cos(n\psi(t_k)) + z_{s,K}^{(n)} \sin(n\psi(t_k)) \right),$$

with N_B as harmonic bases, angular position $\psi(t_k) \in [\psi_K - 2\pi N_R, \psi_K]$, where $\psi_K = K\Delta\psi$ and the coefficients are calculated by the following integral operations

$$\begin{aligned} z_{c,K}^{(n)} &= \frac{1}{\pi N_R} \int_{\psi_K - 2\pi N_R}^{\psi_K} \hat{z}(\psi) \cos(n\psi) d\psi, \\ z_{s,K}^{(n)} &= \frac{1}{\pi N_R} \int_{\psi_K - 2\pi N_R}^{\psi_K} \hat{z}(\psi) \sin(n\psi) d\psi. \end{aligned} \quad (4.20)$$

which can be approximated, e.g., by using trapezoidal numerical integration. The $\hat{(\cdot)}$ -notation is used to represent the estimate of the specified signal. The azimuthal sampling (i.e., sampling at different azimuth positions) is represented by $\Delta\psi$, whose steps are indicated by K *spatial* steps. Meanwhile, Δt denotes sampling time whose *temporal* steps are indicated by k . In this chapter, note that only the first harmonic components of (4.20), referring to the 1P frequency, are used.

4.4 Kalman Filter Design

Kalman filtering is employed to retrieve information about the unknown periodic load, as well as the wind turbine states unavailable from the measurements. The KF is defined by

the following discretized state-space equation—augmented with the random walk models of the disturbance [98]

$$\underbrace{\begin{bmatrix} \mathbf{x}_{k+1} \\ \mathbf{d}_{k+1} \end{bmatrix}}_{\mathbf{x}_{\text{aug},k+1}} = \underbrace{\begin{bmatrix} \mathcal{A}(\rho_k) & \mathcal{B}_d \\ \mathbf{0} & \mathbf{I} \end{bmatrix}}_{\mathcal{A}_{\text{aug}}(\rho_k)} \underbrace{\begin{bmatrix} \mathbf{x}_k \\ \mathbf{d}_k \end{bmatrix}}_{\mathbf{x}_{\text{aug},k}} + \underbrace{\begin{bmatrix} \mathcal{B}_u \\ \mathbf{0} \end{bmatrix}}_{\mathcal{B}_{\text{aug}}} \mathbf{u}_k + \underbrace{\begin{bmatrix} \mathbf{w}_k \\ \mathbf{w}_{d,k} \end{bmatrix}}_{\mathbf{w}_{\text{aug},k}}, \quad (4.21)$$

$$\mathbf{y}_k = \underbrace{\begin{bmatrix} \mathbf{C} & \mathbf{D}_d \end{bmatrix}}_{\mathbf{C}_{\text{aug}}} \mathbf{x}_{\text{aug},k} + \mathbf{D}_u \mathbf{u}_k + \mathbf{v}_k, \quad (4.22)$$

with $\mathcal{A}(\rho_k)$, \mathcal{B}_u , and \mathcal{B}_d as the discretized state, input, and disturbance matrices, respectively. The quantities \mathbf{w} , \mathbf{w}_d , and \mathbf{v} are the uncorrelated process, random walk, and measurement white noise sequence, the covariance matrix of which is defined as

$$E \begin{bmatrix} \mathbf{w}_{\text{aug},k} \\ \mathbf{v}_k \end{bmatrix} \begin{bmatrix} \mathbf{w}_{\text{aug},k}^T & \mathbf{v}_k^T \end{bmatrix} = \text{diag}(\mathbf{Q}_{\text{aug}}, \mathbf{R}), \quad (4.23)$$

where the state covariance matrix \mathbf{Q}_{aug} and the measurement covariance matrix \mathbf{R} act as tuning variables for the KF. The operator E represents the expected value. The KF algorithm includes two steps: *a priori* state and error covariance matrix estimation, followed by *a posteriori* state and error covariance matrix correction. For the detailed recursive algorithm, the interested reader is referred to [98].

4.5 Case Study

Prior to assessing the performance of the designed KF, it is compelling to validate the derived extended demodulated wind turbine model, as represented by the state equation (4.17) and output equation (4.19). After that, the ability of the KF in estimating the unknown periodic load components, as well as the tower velocity and displacement, is illustrated.

As a demonstration, the reference NREL 5MW wind turbine model [25] is considered. Its first tower modal properties, specified in Table 4.1, are tuned such that its natural frequency $\omega_n = \sqrt{k/m}$ lies in the below-rated operating region; resembling slender, *soft-soft* towers [14]. In this case, a conventional $K - \omega^2$ generator torque control law [13] is employed. Since above-rated turbine operation is of no interest in this study, a staircase uniform wind profile in the $v = 4 - 10$ m/s range is considered with 1.5 m/s step increases every 100 s, for 500 s of total simulation time.

4.5.1 Model Validation

In this section, the response of the demodulated acceleration signal pair $\{q_a, q_b\}$ is demonstrated. In addition, the nominal model's measurement is demodulated using MSD, which yields the $\{q_c^{(1)}, q_s^{(1)}\}$ signals, i.e. the cosine and sine components of the first harmonic of the nominal tower acceleration signal. As depicted in Fig. 4.2, the amplitude of these signal pairs are calculated by taking their two-norms to show whether they follow the nominal model's amplitude. This is shown to be the case for both $\{q_a, q_b\}$ and $\{q_c^{(1)}, q_s^{(1)}\}$, although the latter shows a delayed response due to the integration in (4.20). Even though

Table 4.1: Parameters of the (modified) NREL-5MW reference wind turbine.

| Description | Symbol | Value | Unit |
|-------------------------|------------|----------------------|---------------------|
| Gearbox ratio | G | 97 | - |
| LSS equivalent inertia | J_r | 4.0802×10^7 | kg m^2 |
| Rotor radius | R | 63 | m |
| Tower height | H | 90 | m |
| Tower modal mass | m | 1000 | kg |
| Tower modal damping | d | 100 | kg s^{-1} |
| Tower modal stiffness | k | 500 | kg s^{-2} |
| Tower natural frequency | ω_n | 0.7071 | rad s^{-1} |

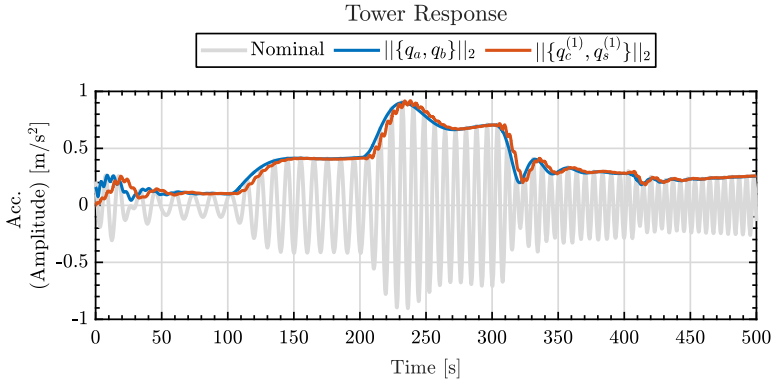


Figure 4.2: Comparison between the measured nominal wind turbine tower acceleration and the amplitude of both the extended demodulated model and MSD-demodulated signals, $\{q_a, q_b\}$ and $\{q_c^{(1)}, q_s^{(1)}\}$, respectively. The demodulated responses show accurate tracking of the periodic amplitude, whereas those of the MSD-method exhibit a slight delay as a result of integral operations of the measurements demodulation.

the phase information calculated from these pairs are not included in the figure, similar behavior is observed.

Hence, this result implies that the proposed extended demodulated model can be used in a more realistic situation as opposed to [53], where a demodulated second-order model is excited to provide tower displacement amplitude information. Moreover, the MSD method enables measurements to be demodulated and used together with the proposed model, such as for Kalman filtering in the following section.

4.5.2 Kalman Filter Performance Assessment

In the performance assessment of the proposed periodic load estimation method, the extended demodulated model is employed as the internal model of the KF after discretized with fourth-order Runge-Kutta method at 0.01 s of sampling time. The observer takes the tower acceleration and the generator torque input in their MSD-demodulated forms, whereas the rotor measurement is fed directly from the turbine, as illustrated in Fig. 4.3.

The periodic load $a_u \cos(\omega_r t + \phi_u)$ with slowly-varying a_u and ϕ_u is simulated by generating sinusoidal $\Re\{A_u\}$ and $\Im\{A_u\}$, with an amplitude of $75\sqrt{2} \pm 15$ N and a frequency

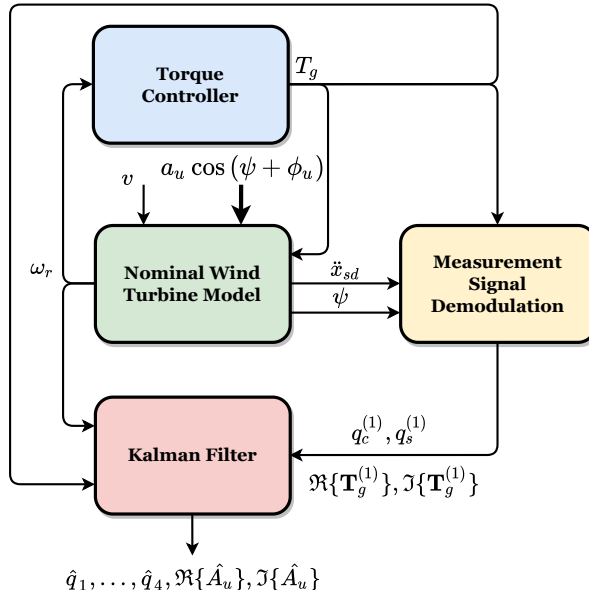


Figure 4.3: Implementation of the proposed KF based on the demodulated wind turbine and tower model. The KF estimates the demodulated periodic load components, as well as the unmeasurable tower states, and takes inputs from the torque controller and the (MSD-demodulated) nominal wind turbine model measurements.

of 0.025 rad/s. Imposing a phase offset of $\pi/2$ rad for $\Im\{A_u\}$ generates a varying ϕ_u . The parameters of the resulting periodic signal can thus be characterized as $a_u \in [135, 165]$ N and $\phi_u \in [39.25, 50.75]$ deg. For the specified simulation settings, the covariance matrices are selected to be $\mathbf{Q}_{\text{aug}} = \text{diag}(10^{-6}, \dots, 10^{-6}, 5 \cdot 10^{-2}, 5 \cdot 10^{-2})$ and $\mathbf{R} = \text{diag}(10^{-5}, 10^{-5}, 10^{-5})$.

The simulation results are shown in Fig. 4.4, demonstrating that the unknown wind turbine tower states $\hat{q}_1, \dots, \hat{q}_4$ are reconstructed with minimal discrepancies from the reference. Moreover, the periodic disturbance elements $\Re\{A_u\}$ and $\Im\{A_u\}$ are estimated, from which the slowly-varied amplitude and phase offset can be calculated. They show good tracking behavior with respect to the original signal. In Fig. 4.5a, the capability of the load amplitude estimate is compared with the original signal; demonstrating that the former is able to closely follow the latter's amplitude. Figure 4.5b shows another reconstruction of the unknown periodic load signal, in which the phase estimate information is incorporated¹.

Discrepancies are seen after every step in wind speed before the estimates converge back to the actual signal. The MSD-demodulated signals experience some delay due to the integral operations in (4.20), which are shown to be more sensitive toward large, abrupt changes in the tower acceleration. This appeared to be the case particularly during the transients near the critical tower excitation at $t = 200$ s and $t = 300$ s (see Fig. 4.2). It is also observed that the steady state estimation error of $\Re\{A_u\}$ varies for different wind speeds

¹Please note that in [99], where this work was originally published, only Fig. 4.5a is provided due to space limitation. This thesis includes Fig. 4.5b for completeness.

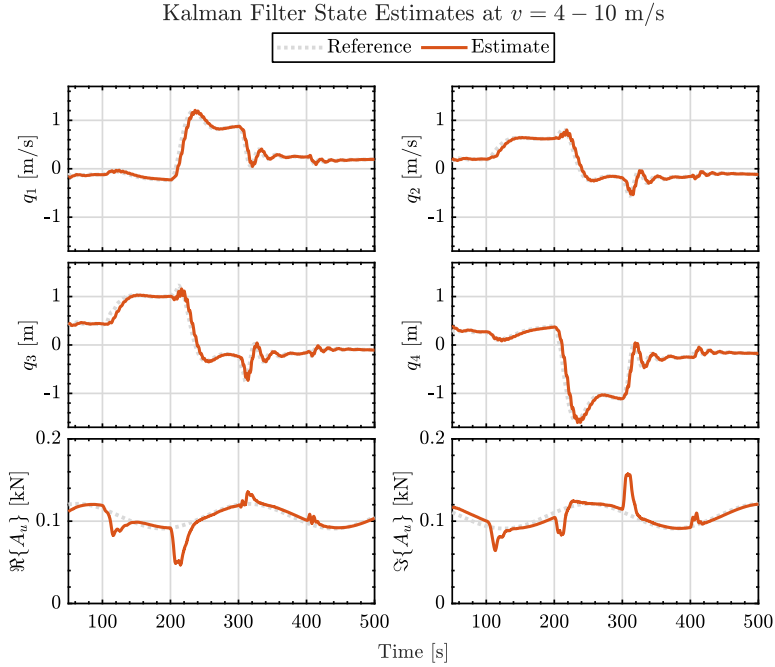
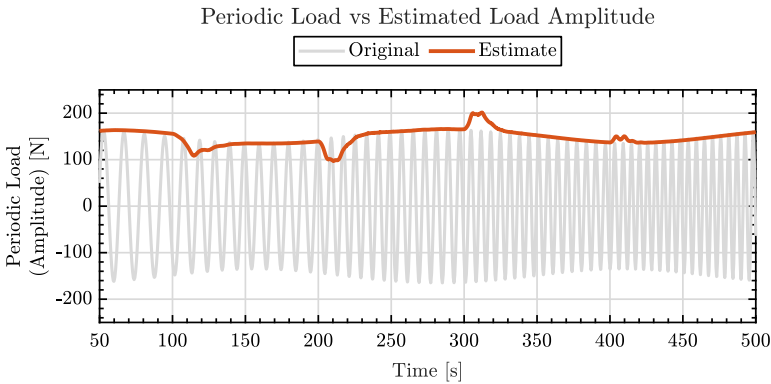
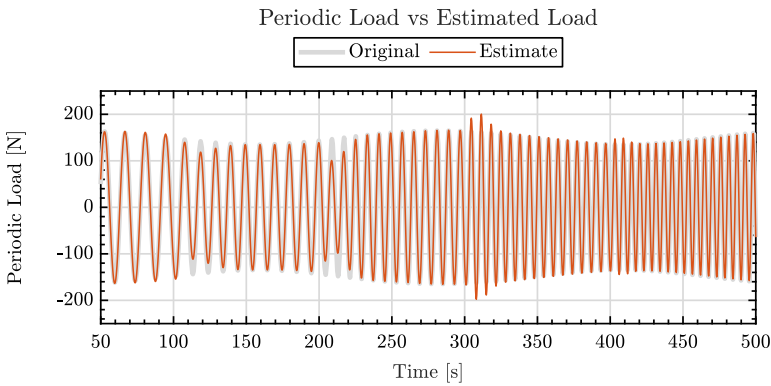


Figure 4.4: Kalman filtering result. Good tracking of the estimates with respect to the reference periodic load components and tower states is observed despite slightly delayed response, bias, and transient discrepancies after each wind step.

within $[0.5, 4.5]\%$ range whereas for $\Im\{A_u\}$ this value ranges between $[0.3, 5]\%$. Such performance limitations might suggest that a delay-proof mechanism needs to be incorporated for future KF design. Regardless, it has been shown that using the MSD-demodulated acceleration signals as the KF inputs, the unknown periodic disturbance and the remaining demodulated tower states could be reconstructed to a large extent. This allows strategies, such as feedforward control [63], to be employed together with the state-of-the-art qLPV-MPC algorithm [53] in future work for further load reductions.



(a)



(b)

Figure 4.5: Reconstruction of the periodic load from the KF estimation compared with the original signal. In (a) the unknown periodic load amplitude estimate is shown; in (b) reconstruction of the unknown periodic load incorporating phase estimate information is presented.

4.6 Conclusions

In this work, the extended demodulated wind turbine model has been derived, which incorporates slowly-varying periodic excitation's amplitude and phase offset, generator torque contribution to the tower motion, and a new output equation containing demodulated acceleration signal. The extended model's output has been evaluated against that of the nominal signal, in which the former has been shown to closely track the amplitude of the latter. Furthermore, a Kalman filter augmented with random walk models has been designed using the new model and assessed at the below-rated regime. It proved capable of estimating the periodic disturbance components and the unknown tower states, in good agreement with the respective disturbance and tower states references. Future work will comprise improvements on the delay tolerance aspect of the unknown input observer, as well as active tower damping control by qLPV-MPC, by means of the extended model.

5

On the Analysis and Synthesis of Wind Turbine Side-Side Tower Load Control via Demodulation

5

As wind turbine power capacities continue to rise, taller and more flexible tower designs are needed for support. These designs often have the tower's natural frequency in the turbine's operating regime, increasing the risk of resonance excitation and fatigue damage. Advanced load-reducing control methods are needed to enable flexible tower designs that consider the complex dynamics of flexible turbine towers during partial-load operation. This chapter proposes a novel modulation-demodulation control (MDC) strategy for side-side tower load reduction driven by the varying speed of the turbine. The MDC method demodulates the periodic content at the once-per-revolution (1P) frequency in the tower motion measurements into two orthogonal channels. The proposed scheme extends the conventional tower controller by augmentation of the MDC contribution to the generator torque signal. A linear analysis framework into the multivariable system in the demodulated domain reveals varying degrees of coupling at different rotational speeds and a gain sign flip. As a solution, a decoupling strategy has been developed, which simplifies the controller design process and allows for a straightforward (but highly effective) diagonal linear time-invariant controller design. The high-fidelity OpenFAST wind turbine software evaluates the proposed controller scheme, demonstrating effective reduction of the 1P periodic loading and the tower's natural frequency excitation in the side-side tower motion.

5.1 Introduction

The improvements in the cost-effectiveness of wind turbines can be traced back to the adoption of the upscaling strategy, in which the sizes of the turbine components are made larger [10]. Turbine rotors are made larger and can capture more energy by the increased swept area and towers are built taller to support such larger rotors. Moreover, at higher altitudes, the wind energy resource is of higher quality as the influence of surface friction is less prominent, resulting in more power production by a single machine.

Conventional tower upscaling, however, is not desirable as merely increasing tower heights and diameters while keeping the same wall thickness results in much heavier and more expensive structures. In addition, transportability constraints, e.g., on tower base diameter, limit the size of which the towers can be designed, especially for onshore installations [14]. While satisfying the transportability requirements, reducing the tower wall thickness is a compelling solution to lower the needed amount of mass and thus manufacturing costs of tall towers. In contrast to conventional *soft-stiff* tower designs, resulting *soft-soft* designs lower the tower's (first) natural frequency into the turbine operational range. Consequently, the risk of resonance by excitation of the time-varying rotor speed, also known as the once-per-revolution (1P) frequency, is thus becoming ever greater. Rotor imbalance could even further exacerbate this effect [36, 100]. Tower resonance excitation is even more concerning for the side-side tower oscillations than for the fore-aft due to the negligible contribution of the aerodynamic damping in the formerly mentioned direction [13]. So, reliable and advanced control solutions capable of fatigue load mitigation are of utmost importance to improve the viability of soft-soft tower designs.

Different control implementations have been made available in the literature for tower periodic load control and are generally classified as passive and active methods. Passive methods prevent prolonged turbine operation near the tower resonance frequency, usually by decreasing or increasing generator torque demand to accelerate or decelerate the rotor, depending on whether its speed is above or below the resonance frequency. This method is often referred to as frequency skipping by speed exclusion zones. Bossanyi introduced the approach for avoiding tower resonance by blade passing frequency at three-times-per-revolution (3P) for three-bladed wind turbines [30]. Licari et al. studied the effects of the speed exclusion zone's width tuning for 1P excitation in terms of load reduction and power quality [35]. Smilden and Sørensen later adopted this algorithm for preventing resonance of fore-aft tower motion by the 3P thrust oscillations [38]. However, such conventional implementations are non-trivial due to the intricate logic that needs to be incorporated, resulting in not knowing whether the control solution is dynamically optimal. Therefore, a state-of-the-art quasi-linear parameter varying model predictive control (qLPV-MPC) method was developed to tackle the shortcomings and challenges of conventional methods [53].

Active control methods, on the other hand, feed tower measurements into a controller to generate counteracting forces through provided actuators so as to dampen the tower vibration [30, 31]. The controller, typically an integrator when acceleration is measured, is designed to increase tower damping. Depending on whether the fore-aft [30, 31, 101] or side-side direction [31, 32] is targeted for damping, respectively, the collective pitch or generator torque demand is utilized as the control input. Such a conventional approach was originally devised to reduce tower vibration at its natural frequency. Nonetheless,

a tower load controller specifically aiming at the time-varying 1P periodic loading has received little to no attention in the literature and would be an attractive complement to the conventional method.

This chapter extends the conventional control method by a modulation-demodulation setup to further improve side-side tower load reduction performance. Such a controller design additionally provides a reduction of the rotational-speed-driven load and allows for comprehensive system analysis and controller synthesis. To the best of the authors' knowledge, such an approach has not yet received any attention in the wind turbine control literature.

In the control engineering field, an approach known as the modulation-demodulation control (MDC) is considered an effective solution to periodic disturbance cancellation problems [56–58]. MDC is able to adapt its control input's frequency to reject a time-varying disturbance frequency and can handle the changes in the dynamics of the plant due to the variation of the disturbance frequency. A large body of literature has been dedicated to further studying MDC's potential, which includes applications in diverse fields. For instance, [57] focuses on MDC tuning from the perspective of the frequency-domain loop-shaping method for the application of a diamond turning machine. The work of [102] analyses the feedback limitations of MDC by poles, zeros, and delays investigation. In [58], vibration control of flexible piezoelectric structures by MDC was conducted. Other applications include digital data storage system [103], helicopter [104], flexible web winding system [105], and tape system [106], just to mention a few.

The MDC control method bears similarities with a highly-anticipated and industrially applied periodic blade load alleviation technique known as individual pitch control (IPC) [15]. For most IPC implementations, the Coleman transformation [39] is employed to project measured individual blade moments containing periodic content from the rotating frame into a static nonrotating frame. The scheme can be thought of as a modulation-demodulation framework where structural analysis and controller design are simplified in the nonrotating domain. However, it has been known that larger and more flexible rotor structures create severe coupling of the considered multivariable system. Therefore, for single-input single-output (SISO) controller designs to be justified in the transformed domain, decoupling strategies must be taken into account [70, 107]. In MDC, identical and rather simple diagonal SISO controllers can also be designed onto low-frequency, orthogonal *quadrature* and *in-phase* channels resulting from the *demodulation* of the plant's measurements. This operation is similar to the forward Coleman transformation in the conventional IPC. The computed control actions on these orthogonal channels are then converted into the actual usable input at the disturbance frequency by the *modulation* operation, similar to the reverse Coleman transformation. Nevertheless, despite its demonstrated effectiveness in wide applications, little attention has been paid to adapting MDC for mitigating periodic loading affecting wind turbine side-side tower motion.

This chapter focuses on the development of MDC for the rejection of 1P periodic loading on wind turbine side-side tower motion. The proposed MDC results in a periodic generator torque control input with time-varying 1P frequency, which, given the measurements of the rotor speed, is able to track the disturbance's frequency. However, frequency-domain analysis of the demodulated system shows that the quadrature and in-phase channels are not fully decoupled. Moreover, changing rotational speed induces a gain sign flip,

which may cause instability in the closed-loop operation. Therefore, a decoupling strategy by phase offset inclusion, similar to that in the conventional IPC [70], is developed to arrive at fully decoupled quadrature and in-phase channels and simultaneously remove the gain sign flip.

The contribution of this work is four-fold:

1. Formulating MDC for the mitigation of periodic load affecting wind turbine side-side tower motion induced by the time-varying 1P rotor excitation;
2. Providing frequency domain frameworks for the analysis of the system coupling and controller behavior in their (de)modulated representations;
3. Decoupling the multivariable system and correcting the gain sign flip by the inclusion of a phase offset, as well as illustrating the offset's influence on the controller;
4. Showcasing the performance of MDC in both simplified and high-fidelity computer-aided wind turbine simulation environments along with a conventional active tower damper.

The remainder of this chapter is structured as follows. Section 5.2 describes the nominal wind turbine dynamics and conventional tower damping controller. In Section 5.3, the derivation of the proposed MDC framework in the frequency domain is presented. Section 5.4 elaborates on controller and system analysis in the MDC framework, in which the cross-coupling phenomenon and gain sign flip in the quadrature and in-phase MDC channels are discussed. Then, in Section 5.5, the phase offset inclusion for the channel decoupling and gain sign flip correction on the tower dynamics, as well as influence on the controller, is explained. In Section 5.6, the effectiveness of the proposed controller is demonstrated using low- and high-fidelity simulations. Concluding remarks are drawn in Section 5.7.

5.2 Wind Turbine Dynamics and Conventional Tower Damping Controller

To form the basis for controller design and analysis in this chapter, wind turbine aerodynamic and tower models are derived in Section 5.2.1. As the goal of this chapter is to augment the proposed controller to that of the conventional active tower damping controller, the latter's design is discussed in Section 5.2.2 and is combined with the tower dynamics. Section 5.2.3 derives the frequency domain representation of the combined tower dynamics for later uses in the MDC framework.

5.2.1 Tower and aerodynamic models

The model used for analysis and synthesis considered in this study consists of side-side tower dynamics and rotor aerodynamics. The tower dynamics are approximated as a second-order system, representing the first structural mode as follows:

$$\ddot{x}(t) = \frac{1}{m} \left(-d\dot{x}(t) - kx(t) + F_{sd}(t) + s_f(T_g(t) + \Delta T_{g,damp}(t) + \Delta T_g(t)) \right), \quad (5.1)$$

where m denotes the tower modal mass, d its damping, and k the modal stiffness. The notation t indicates a time-domain signal, which, for the sake of brevity, is omitted in the text unless necessary. Tower-top acceleration, velocity, and displacement are represented by \ddot{x} , \dot{x} , and x , respectively. The motion of the tower is affected by generator torque activities T_g , $\Delta T_{g,\text{damp}}$, and ΔT_g through the generator stator reaction, all of which are the considered control actions in this chapter. The torque T_g is used mainly in power production, whereas the additive torques $\Delta T_{g,\text{damp}}$ and ΔT_g are utilized to respectively increase the effective tower damping and mitigate the periodic loading F_{sd} . The factor $s_f = 1.5/H$, with H being the tower height, is the ratio between the rotational and translational displacements of the tower motion under the assumption that the tower is a prismatic beam [63].

The periodic loading aforementioned may develop on the rotor due to, e.g., a mass or aerodynamic imbalance and transferred to the fixed structure, which is modeled as the following sinusoidal force [99]

$$F_{\text{sd}}(t) = a_{\text{sd}} \cos(\omega_r(t)t + \phi_{\text{sd}}), \quad (5.2)$$

where its amplitude and phase offset are denoted as a_{sd} and ϕ_{sd} , respectively, in which the former can be considered a centrifugal force [35]. Figure 5.1 illustrates how this force affects the tower.

Remark 5 *Although the main focus of this work is on the side-side tower loading, the proposed method explained later in Section 5.3 can also be applied to fore-aft tower loading. This is done by replacing (5.1) with that of the fore-aft tower dynamics, where thrust force is acting on the tower top, manipulable by collective blade pitching.*

The frequency of F_{sd} varies in time as the rotor speed ω_r changes according to the following rotor aerodynamics, resembling a first-order rotational mass system

$$\dot{\omega}_r(t) = \frac{1}{J_r} T_a(t) - \frac{G}{J_r} (T_g(t) + \Delta T_{g,\text{damp}}(t) + \Delta T_g(t)). \quad (5.3)$$

In the above equation, J_r represents the equivalent inertia at the low-speed-shaft (LSS) side and G is the gearbox ratio. The aerodynamic torque is given by

$$T_a(t) = \frac{1}{2\omega_r(t)} \rho_a \pi R^2 C_p(\omega_r(t), v(t), \beta(t)) v(t)^3,$$

with the air density denoted by ρ_a , rotor radius R , and aerodynamic power coefficient C_p , being a function of ω_r , wind speed v and pitch angle β . To achieve maximum power extraction at the below-rated operating regime, as considered in this work, the so-called $K\omega_r^2$ control law [26] is employed for the torque controller

$$T_g(t) = \underbrace{\frac{1}{2\lambda^{*3}G} \rho_a \pi R^5 C_p^*}_{K} \omega_r(t)^2, \quad (5.4)$$

where K is the optimal gain, λ^* as the design tip-speed ratio corresponding to the optimal power coefficient C_p^* at fine pitch position. This work employs only a simple maximum power tracking controller, as load mitigation is the main focus. However, a more advanced method is available in the literature for the interested reader, e.g. [24].

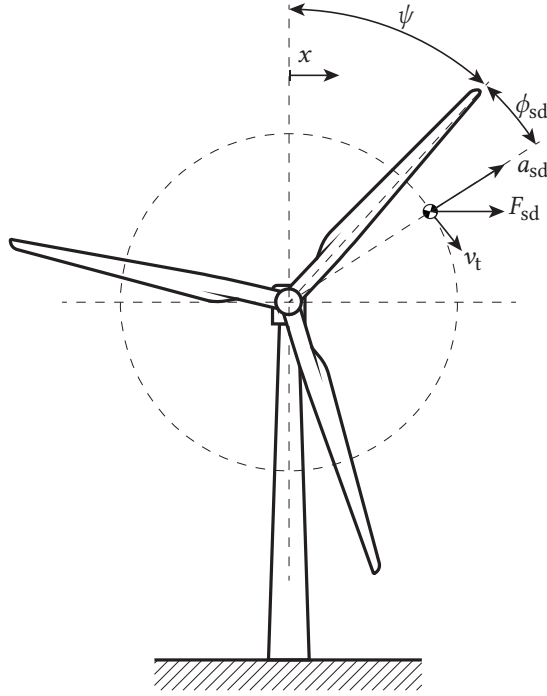


Figure 5.1: A wind turbine is excited at the side-side direction by a periodic load due to the rotor imbalance at the 1P frequency $F_{sd}(t) = a_{sd} \cos(\psi(t) + \phi_{sd})$, with the azimuth $\psi(t) = \omega_r(t)t$. The tangential speed of the periodic load is indicated by $v_t(t)$, and $x(t)$ denotes tower top displacement in the horizontal direction.

5.2.2 Conventional Active Tower Damping Controller

With the wind turbine model at hand, a side-side tower damping controller is added to obtain the nominal system considered in the remainder of this chapter. The wind turbine tower dynamics (5.1) commonly possess only negligible damping d such that additional damping is required to mitigate fatigue loads at the tower's natural frequency. Conventionally, for the side-side direction, the extra damping is created by additional generator torque demand, being negatively proportional to the tower-top velocity (also taking into account s_f) as follows [31]

$$\Delta T_{g,damp}(t) = -K_{conv}\dot{x}(t), \quad (5.5)$$

with

$$K_{conv} = \frac{d_{add}}{s_f}, \quad (5.6)$$

as a constant gain where d_{add} is the additional, desired modal damping. Note that since \ddot{x} is often measurable, it is necessary to perform integration of this signal to obtain \dot{x} ; thus, this controller is essentially an integral controller.

The increase in the effective modal damping coefficient is now evident by substituting

$\Delta T_{g,damp}$ in (5.1) with (5.5), such that the tower dynamics are rendered into

$$\ddot{x}(t) = \frac{1}{m} \left(-d_{\text{eff}} \dot{x}(t) - kx(t) + F_{\text{sd}}(t) + s_f(T_g(t) + \Delta T_g(t)) \right), \quad (5.7)$$

with $d_{\text{eff}} = d + d_{\text{add}}$ being the effective damping. However, the conventional tower damper does not focus on the mitigation of 1P periodic loading posed by F_{sd} . Later on in this chapter, the development of MDC for alleviating this rotor-speed-driven load is discussed further as an extension to this conventional controller, making use of (5.7).

5.2.3 Frequency Domain Representation

For a significant part of Sections 5.3-5.6, MDC design and analysis are done in the frequency domain. This requires the dynamics (5.7) to be expressed in this domain as well, where the transfer from ΔT_g to \dot{x} is considered. The Laplace transformation of the tower dynamics gives the following transfer function

$$G(s) = \frac{\dot{X}(s)}{\Delta T_g(s)} = \frac{s_f s}{ms^2 + d_{\text{eff}} s + k}, \quad (5.8)$$

where s is the Laplace operator. The notations $\dot{X}(s)$ and $\Delta T_g(s)$ are the tower-top velocity and additive generator torque in their frequency domain representation. Also useful is to define $N(s)$ and $D(s)$ to denote the numerator and denominator of $G(s)$.

5.3 Modulation-Demodulation Control Scheme

This section provides an elaboration on the MDC architecture, which is based on the approach proposed by [58]. The MDC architecture and accompanying analysis methods are utilized to provide a control-oriented analysis of the controller and wind turbine system. As a prerequisite for subsequent derivations, the following Laplace transforms of signal modulations at the disturbance frequency ω_r are defined

$$\mathcal{L}\{r(t) \cos(\omega_r t)\} = \frac{1}{2} (R(s_-) + R(s_+)), \quad (5.9a)$$

$$\mathcal{L}\{r(t) \sin(\omega_r t)\} = -\frac{j}{2} (R(s_-) - R(s_+)), \quad (5.9b)$$

with $r(t)$ as an arbitrary time-domain signal and $R(s)$ its Laplace-transformed analogue. For this linear analysis, ω_r is assumed to be constant over a single period. The notation $s_{\pm} = s \pm j\omega_r$ is introduced to indicate ω_r -shifted frequency content. Another useful relation for the derivations that follow is the following Euler's formula

$$e^{j\phi} = \cos(\phi) + j \sin(\phi), \quad (5.10)$$

with ϕ as an arbitrary angle.

The MDC methodology follows the depiction in Fig. 5.2, where modulation and demodulation involve signal multiplications with trigonometric functions at the disturbance frequency ω_r . In contrast to the work of [58], any filtering in the demodulation stage is omitted and is relocated to the controller block/stage for the sake of generalization.

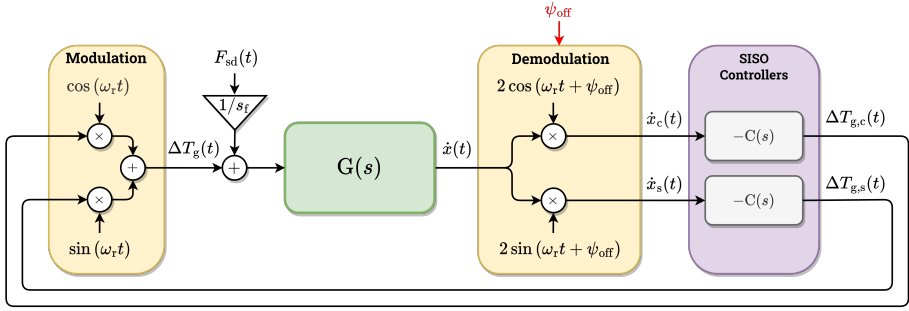


Figure 5.2: The modulated-demodulated control scheme for the cancellation of a side-side periodic load $F_{sd} = a_{sd} \cos(\omega_r t + \phi_{sd})$ affecting wind turbine tower $G(s)$. The demodulation operation is driven by the disturbance frequency ω_r and creates a separation of the output signal \dot{x} into quadrature and in-phase signals, \dot{x}_c and \dot{x}_s , respectively. On these channels, two identical SISO controllers $C(s)\mathbf{I}_{2 \times 2}$ are designed, generating the control inputs $\Delta T_{g,c}$ and $\Delta T_{g,s}$. Finally, modulation at ω_r combines these two control inputs into a single signal ΔT_g that is fed into $G(s)$ to alleviate the periodic loading. The phase offset ψ_{off} can be added to the demodulator to influence the system's behavior, such as channel decoupling. Note that the negative sign preceding $C(s)$ indicates the negative feedback convention used in the framework and the inverse of the scaling factor s_f follows F_{sd} for consistency with (5.7)-(5.8). This diagram only considers the proposed control solution with the tower dynamics $G(s)$; the complete wind turbine is also torque-controlled using the $K\omega_r^2$ controller strategy (5.4).

Demodulation is the first stage of the MDC scheme, where \dot{x} , being the output of the plant $G(s)$ perturbed by disturbance F_{sd} , is multiplied by cosine and sine of the disturbance frequency ω_r . The cosine and sine multiplication of \dot{x} results in

$$\begin{bmatrix} \dot{x}_c(t) \\ \dot{x}_s(t) \end{bmatrix} = \begin{bmatrix} 2 \cos(\omega_r t + \psi_{off}) \\ 2 \sin(\omega_r t + \psi_{off}) \end{bmatrix} \dot{x}(t), \quad (5.11)$$

with \dot{x}_c and \dot{x}_s being the quadrature and in-phase components of the output and ψ_{off} as a phase offset. It needs to be remarked that the factor of 2 in (5.11) follows the convention of [58] and that ψ_{off} is plant-specific and dependent on its dynamics, as detailed later on in Section 5.5.2.

By making use of (5.9)-(5.10), the relation (5.11) results in the following frequency-domain representation

$$\begin{bmatrix} \dot{X}_c(s) \\ \dot{X}_s(s) \end{bmatrix} = \left(e^{j\psi_{off}} \begin{bmatrix} 1 \\ -j \end{bmatrix} \dot{X}(s_-) + e^{-j\psi_{off}} \begin{bmatrix} 1 \\ j \end{bmatrix} \dot{X}(s_+) \right). \quad (5.12)$$

For each of the quadrature and in-phase channels, a linear time-invariant (LTI), SISO *demodulated controller* $C(s)$ is implemented and forms a diagonal decoupled structure, as shown in the following

$$\begin{bmatrix} \Delta T_{g,c}(s) \\ \Delta T_{g,s}(s) \end{bmatrix} = C(s) \begin{bmatrix} \dot{X}_c(s) \\ \dot{X}_s(s) \end{bmatrix}, \quad (5.13)$$

where $C(s) = C(s)\mathbf{I}_{2 \times 2}$. The diagonal controller structure is intended for equal load reduction performance on both channels of the multivariable demodulated system and is valid if both channels have negligible interaction/coupling. As will be shown in Section 5.4,

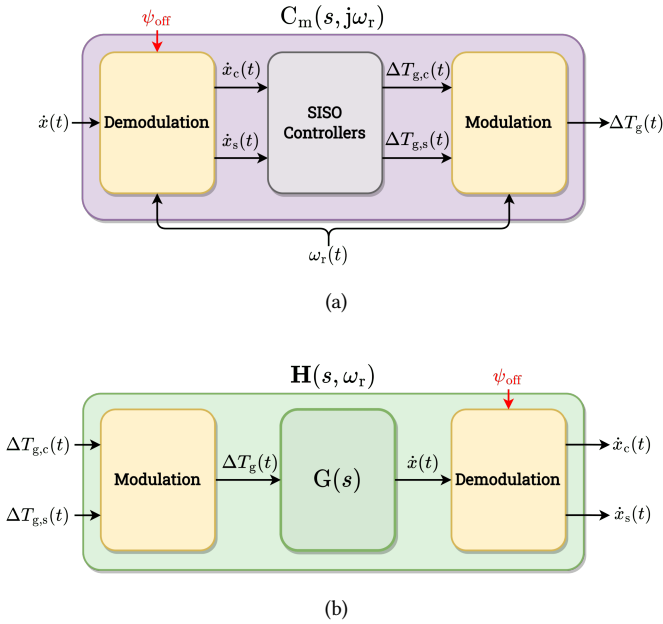


Figure 5.3: (a) SISO modulated controller $C_m(s, \omega_r)$ and (b) MIMO demodulated plant $H(s, \omega_r)$ in the MDC scheme.

this condition is generally not met for all operating points. The phase offset earlier introduced in (5.11) plays an important role in the decoupling of the system throughout varying operational conditions.

Transforming back the quadrature and in-phase control signals $\Delta T_{g,c}$ and $\Delta T_{g,s}$ from the demodulated domain back to the additive torque signal ΔT_g is accomplished by the modulation operation

$$\Delta T_g(s) = \frac{1}{2} \left([1 \quad -j] \begin{bmatrix} \Delta T_{g,c}(s_-) \\ \Delta T_{g,s}(s_-) \end{bmatrix} + [1 \quad j] \begin{bmatrix} \Delta T_{g,c}(s_+) \\ \Delta T_{g,s}(s_+) \end{bmatrix} \right), \quad (5.14)$$

which is the frequency domain equivalence of

$$\Delta T_g(t) = \begin{bmatrix} \cos(\omega_r t) & \sin(\omega_r t) \end{bmatrix} \begin{bmatrix} \Delta T_{g,c}(t) \\ \Delta T_{g,s}(t) \end{bmatrix}. \quad (5.15)$$

The equation above completes the derivation for the MDC framework.

5.4 MDC Controller and System Analysis

The established MDC framework allows for analysis of the system and controller, as depicted in Fig. 5.3. Figure 5.3a shows the combination of the (de)modulators with the controller $C(s)$, forming a SISO *modulated controller* representation from \dot{x} to ΔT_g . This transformed controller possesses several beneficial properties, as further demonstrated in

Section 5.4.1. Presented in Fig. 5.3b is the multiple-input multiple-output (MIMO) *demodulated plant* realization in the quadrature and in-phase channels from $[\Delta T_{g,c}, \Delta T_{g,s}]^T$ to $[\dot{x}_c, \dot{x}_s]^T$, resulting from the combination of $G(s)$ and the (de)modulators. Of particular importance is the knowledge of potential cross-coupling between the demodulated channels of the MIMO plant presented in Section 5.4.2. Section 5.4.3 provides insights into the properties of the demodulated multivariable system towards the justification of a decentralized controller $C(s)$.

In Sections 5.4.1 and 5.4.2, theoretical results for transformed controllers and systems are provided, which are subsequently leveraged for the analysis of a linear wind turbine model in Section 5.4.3. The phase offset ψ_{off} plays a remarkably important role in decoupling the demodulated system; however, to provide a clearer analysis, this variable will be included in the derivations after this section.

5.4.1 SISO Modulated Controller Representation

As previously indicated and shown in Fig. 5.3a, the derived frequency-domain framework allows for a different perspective in analyzing the LTI controllers $C(s)$ in the modulation-demodulation scheme. This section shows a remarkable property of the MDC scheme in that the LTI controllers are transformed into a SISO linear time-varying (LTV) controller structure when the modulation and demodulation stages are accounted for.

The SISO modulated controller representation from $\dot{X}(s)$ to $\Delta T_g(s)$ is derived by first substituting (5.12) to (5.13) to obtain the following expression

$$\begin{bmatrix} \Delta T_{g,c}(s) \\ \Delta T_{g,s}(s) \end{bmatrix} = C(s) \left(\begin{bmatrix} 1 \\ -j \end{bmatrix} \dot{X}(s_-) + \begin{bmatrix} 1 \\ j \end{bmatrix} \dot{X}(s_+) \right), \quad (5.16)$$

which is subsequently combined with (5.14), resulting in

$$\Delta T_g(s) = C_m(s, \omega_r) \dot{X}(s) = (C(s_-) + C(s_+)) \dot{X}(s), \quad (5.17)$$

being scheduled by ω_r . The above relation in (5.17) shows that simple LTI controllers in the demodulated system become LTV if the (de)modulators are included. Under the assumption that ω_r is slowly varying and does not (significantly) change within its period, as stated previously, the results from the linear analysis framework in this section generalize to the nonlinear implementation.

Using the derived relation between $C(s)$ and $C_m(s, \omega_r)$ in (5.17). This section shows three, $n = \{1, 2, 3\}$, controller types of interest $C_n(s)$, for which a convenient analytical expression $C_{m,n}(s, \omega_r)$ exists:

1. The first LTI controller is a *proportional controller*

$$C_1 = K_P, \quad (5.18)$$

with $K_P \in \mathbb{R}$ as a constant gain, produces $\Delta T_{g,c}$ and $\Delta T_{g,s}$ that scale \dot{x}_c and \dot{x}_s . This controller is transformed into

$$C_{m,1} = 2K_P, \quad (5.19)$$

independent from ω_r —thus, retains the LTI characteristic of C_1 .

2. The second LTI controller is an *integral controller*

$$C_2(s) = \frac{K_I}{s}, \quad (5.20)$$

with $K_I \in \mathbb{R}$ as an integral gain, which has infinite gain for steady-state deviations and alleviates high-frequent components of \dot{x}_c and \dot{x}_s . Transformation of the considered controller results in

$$C_{m,2}(s, \omega_r) = \frac{2K_I s}{s^2 + \omega_r^2}, \quad (5.21)$$

being an undamped inverted notch filter with a complex pole pair at $\pm j\omega_r$ and, thus, infinite gain at ω_r [56]. This also means that full cancellation of periodic load at this frequency is possible by this type of controller. Also, it is worth mentioning that this controller structure bears a similarity with that of repetitive control. However, both controllers differ in that (5.21) only tackles the fundamental disturbance frequency, whereas repetitive control also inherently accounts for the higher harmonics. Thus, the former is more advantageous in terms of reduced actuator wear and tear. The interested reader is referred to the literature, e.g. [108, 109], for more details on repetitive control.

3. The last LTI controller is a *first-order low-pass filter*

$$C_3(s) = \frac{K_L}{s + \omega_{\text{LPF}}}, \quad (5.22)$$

with a constant gain $K_L \in \mathbb{R}$ and $\omega_{\text{LPF}} \in \mathbb{R}^+$ as the cut-off frequency. This controller is similar to the previous two LTI controllers in that it proportionally scales \dot{x}_c and \dot{x}_s but also alleviates high-frequent components in the demodulated measurement signals. The introduction of ω_{LPF} moves the pole away from the origin, resulting in a non-infinite steady-state gain, in contrast to the integrator controller. Its SISO modulated expression

$$C_{m,3}(s, \omega_r) = \frac{2K_L(s + \omega_{\text{LPF}})}{s^2 + 2\omega_{\text{LPF}}s + \omega_{\text{LPF}}^2 + \omega_r^2}, \quad (5.23)$$

interestingly, is also an inverted notch but with a beneficial property in that it contains a damping term in the denominator ($2\omega_{\text{LPF}}s$), tunable via the selection of ω_{LPF} . This means that, in contrast to $C_{m,2}(s, \omega_r)$, the gain of the controller at ω_r can be limited, which can be desirable in terms of actuation activity needed to dampen periodic loading and added robustness.

Figure 5.4 depicts the Bode magnitude plots of the considered nominal and transformed controllers, which are, respectively, shown by the top and bottom plots to support the discussed observed conclusions. The plots are created with arbitrary choices for $\omega_r = 0.5$ rad/s, $\omega_{\text{LPF}} = 0.01$ rad/s and $K_P = 2$. For the gains in $C_2(s)$ and $C_3(s)$, $K_I = K_L = 2\omega_{\text{LPF}}$ is chosen such that its crossover frequency matches with that of $C_3(s)$, which results in a clearer comparison.

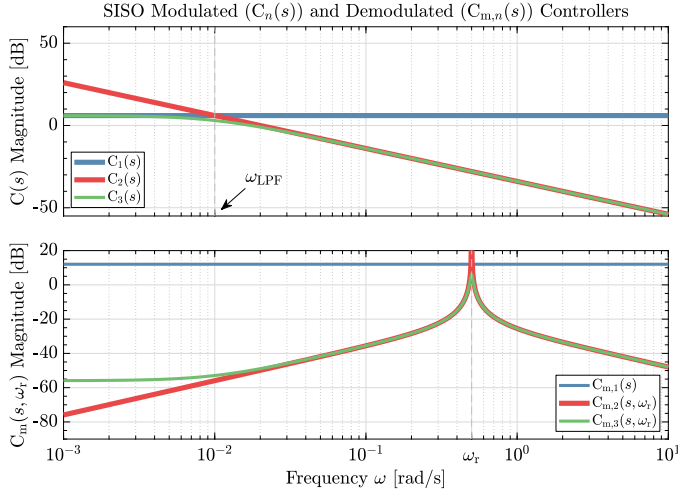


Figure 5.4: Bode magnitude plots of the demodulated controller $C_n(s)$ (top) and the resulting SISO modulated controller $C_{m,n}(s, \omega_r)$ (bottom), $n = \{1, 2, 3\}$. The proportional controller C_1 is mapped into $C_{m,1}$, being the same proportional controller but with an additional factor of 2. The integral controller $C_2(s)$ is rendered into an undamped inverted notch filter $C_{m,2}(s, \omega_r)$ with infinite gain at $\omega_r = 0.5$ rad/s. The low-pass filter $C_3(s)$ with a cut-off frequency of $\omega_{LPF} = 0.01$ rad/s results into a damped inverted notch filter $C_{m,3}(s, \omega_r)$.

In addition to the aforementioned presented LTI controllers $C_n(s)$, alternative controller configurations, potentially of greater complexity, could be suggested and their SISO modulated (LTV) counterparts could be derived by using (5.17). Please refer to [58] for controller selection guidelines.

5.4.2 MIMO Demodulated Plant Representation

The incorporation of the (de)modulators in the proposed framework enables the plant dynamics to be represented as a MIMO system, as shown in Fig. 5.3b, with which the presence of cross-coupling between channels can be investigated. To render the plant dynamics into their demodulated, MIMO representation, the SISO plant $G(s)$ is substituted into (5.12) such that the following equation is obtained

$$\begin{bmatrix} \dot{X}_c(s) \\ \dot{X}_s(s) \end{bmatrix} = \begin{bmatrix} 1 \\ -j \end{bmatrix} G(s_-) \Delta T_g(s_-) + \begin{bmatrix} 1 \\ j \end{bmatrix} G(s_+) \Delta T_g(s_+), \quad (5.24)$$

and substituting (5.14) into (5.24) gives rise to the 2P (i.e. twice-per-revolution) terms indicated by $s_{2\pm} = s \pm 2j\omega_r$ as follows

$$\begin{bmatrix} \dot{X}_c(s) \\ \dot{X}_s(s) \end{bmatrix} = \underbrace{\begin{bmatrix} \mathbf{G}_1(s, \omega_r)^\top \\ \mathbf{G}_2(s, \omega_r)^\top \\ \mathbf{G}_3(s, \omega_r)^\top \end{bmatrix}^\top}_{\mathbf{H}(s, \omega_r)^\top} \begin{bmatrix} \Delta T_{g,c}(s_{2-}) \\ \Delta T_{g,s}(s_{2-}) \\ \Delta T_{g,c}(s) \\ \Delta T_{g,s}(s) \\ \Delta T_{g,c}(s_{2+}) \\ \Delta T_{g,s}(s_{2+}) \end{bmatrix}, \quad (5.25)$$

with $\mathbf{H}(s, \omega_r)$ as the concatenation of the following transfer matrices

$$\mathbf{G}_1(s, \omega_r) = \frac{1}{2} \begin{bmatrix} G(s_-) & -jG(s_-) \\ -jG(s_-) & -G(s_-) \end{bmatrix}, \quad (5.26a)$$

$$\mathbf{G}_2(s, \omega_r) = \frac{1}{2} \begin{bmatrix} G(s_-) + G(s_+) & j(G(s_-) - G(s_+)) \\ j(-G(s_-) + G(s_+)) & G(s_-) + G(s_+) \end{bmatrix}, \quad (5.26b)$$

$$\mathbf{G}_3(s, \omega_r) = \frac{1}{2} \begin{bmatrix} G(s_+) & jG(s_+) \\ jG(s_+) & -G(s_+) \end{bmatrix}. \quad (5.26c)$$

The higher harmonic terms add complexity to the control design and analysis since all the contributions $\mathbf{G}_1(s, \omega_r)$, $\mathbf{G}_2(s, \omega_r)$, and $\mathbf{G}_3(s, \omega_r)$ need to be accounted for. Therefore, the relation above is simplified by selecting an appropriate controller structure that filters out 2P frequency components such that several terms can be omitted, i.e., $[\Delta T_{g,c}(s_{2\pm}), \Delta T_{g,s}(s_{2\pm})]^T \approx 0$. Among the LTI controllers presented in Section 5.4.1, either $C_2(s)$ or $C_3(s)$ is a viable candidate due to the roll-off at high frequencies. Therefore (5.25) simplifies into

$$\begin{bmatrix} \dot{X}_c(s) \\ \dot{X}_s(s) \end{bmatrix} \approx \mathbf{G}_2(s, \omega_r) \begin{bmatrix} \Delta T_{g,c}(s) \\ \Delta T_{g,s}(s) \end{bmatrix}, \quad (5.27)$$

representing an approximation of the demodulated multivariable plant.

5.4.3 Application of MDC on a Simplified Wind Turbine

Now, with the tower dynamics transfer function $G(s)$ at hand, the definition of $\mathbf{G}_2(s, \omega_r)$ in (5.26) is used to transform the nominal dynamics into its demodulated counterpart. It is compelling to investigate their relations by studying Bode plots of both their dynamics. To this end, rather arbitrary wind turbine modal parameters $m = 3 \times 10^4$ kg, $d_{\text{eff}} = 3 \times 10^3$ Ns/m, and $k = 1.5 \times 10^4$ N/m are considered. The chosen parameters resemble a soft-soft wind turbine tower with its natural frequency being $\omega_n = \sqrt{k/m} = 0.7071$ rad/s and the rotor operates in $\omega_r \in \Omega = [\omega_{r,\text{min}}, \omega_{r,\text{rated}}]$, with $\omega_{r,\text{min}} = 0.5$ rad/s and $\omega_{r,\text{rated}} = 1.2$ rad/s.

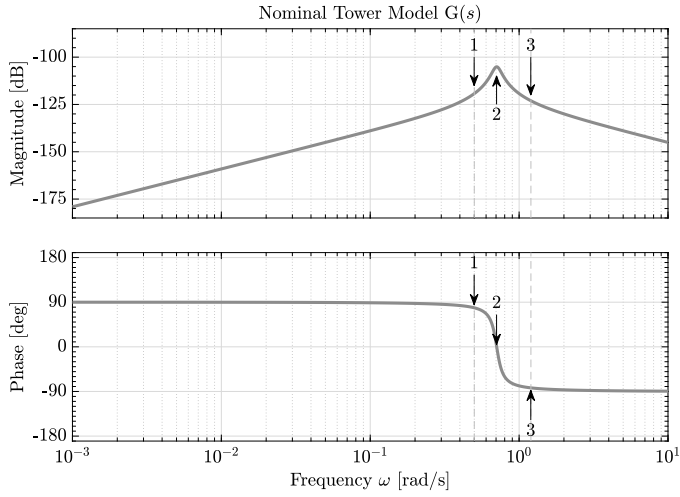
Figure 5.5 shows the Bode plots of both $G(s)$ and $\mathbf{G}_2(s, \omega_r)$, in which the former and latter transfer functions are represented respectively in Figs. 5.5a and 5.5b. As $\mathbf{G}_2(s, \omega_r)$ is a 2×2 Hermitian transfer function matrix, its main and off-diagonal elements,

$$G_{2,11}(s, \omega_r) = G_{2,22}(s, \omega_r) = \frac{1}{2} \frac{N(s_-)D(s_+) + N(s_+)D(s_-)}{D(s_-)D(s_+)}, \quad (5.28)$$

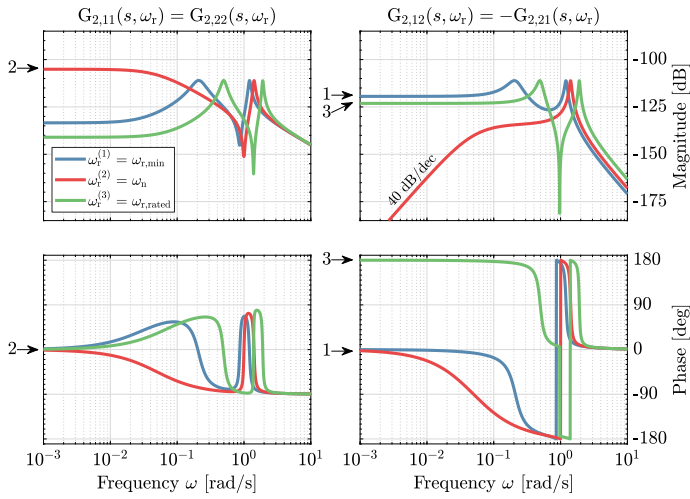
and

$$G_{2,12}(s, \omega_r) = -G_{2,21}(s, \omega_r) = \frac{j}{2} \frac{N(s_-)D(s_+) - N(s_+)D(s_-)}{D(s_-)D(s_+)}, \quad (5.29)$$

are shown in the respective first and second columns of Fig. 5.5b. Since $\mathbf{G}_2(s, \omega_r)$ is parameterized by the 1P frequency, its Bode plot is evaluated for different ω_r values. Specifically, in this case, three frequencies are considered to understand the system's behavior before, at, and after the tower's resonance frequency, i.e., $\omega_r^{(i)} = \{\omega_{r,\text{min}}, \omega_n, \omega_{r,\text{rated}}\}$, where $i = \{1, 2, 3\}$.



(a)



(b)

Figure 5.5: Bode magnitude and phase plots of the nominal (a) and the demodulated (b) wind turbine models. In (a), vertical dashed lines indicate the operating range of a soft-soft wind turbine $G(s)$, where a resonance peak at about $\omega = \omega_n = 0.7071$ rad/s is apparent in the magnitude plot. A 180° phase shift occurs due to the presence of this resonance, as shown in the corresponding phase plot. The points indicated by labeled arrows $i = \{1, 2, 3\}$ represent three sample points $\omega_r^{(i)} = \{\omega_{r,\min}, \omega_n, \omega_{r,\text{rated}}\}$, with $\omega_{r,\min} = 0.5$ rad/s and $\omega_{r,\text{rated}} = 1.2$ rad/s, to evaluate the mapping from $G(s)$ into the steady-state components of $G_2(s, \omega_r)$, as shown in (b), before, during, and after the resonance. Note the 40 dB/dec slope in the magnitude plot of $G_{2,12}(s, \omega_r^{(2)})$ at low frequencies, which indicates the presence of two zeros at the origin.

The modulation-demodulation of $G(s)$ at $s = j\omega_r^{(i)}$ maps its magnitude, $|G(j\omega_r^{(i)})|$, into the steady-state magnitude of the demodulated plant, $|G_2(0, \omega_r^{(i)})|$. Roughly speaking, for

the diagonal LTI SISO controller $C(s)$ to be justified for the entire turbine operating range, it is desirable to have the steady-state magnitudes of the main diagonal be more dominant than the off-diagonal counterparts, that is

$$|G_{2,11}(0, \omega_r)| \gg |G_{2,12}(0, \omega_r)|, \quad \forall \omega_r \in \Omega. \quad (5.30)$$

When the above condition is met, the quadrature and in-phase channels are well decoupled and thus, no significant interaction at low-frequency region and steady-state between channels is present [58].

In Fig. 5.5b, it is shown that this is the case for $G_2(0, \omega_r^{(2)})$, with $\omega_r^{(2)} = \omega_n$. The reason behind such main-diagonal dominance at this operating point is partly due to the presence of a pair of zeros (differentiators) at the origin of $G_{2,12}(s, \omega_r^{(2)})$. Consequently, $|G_{2,12}(s, \omega_r^{(2)})|$ is 0 at steady-state and increases with a 40 dB/dec slope as frequency goes higher, also indicated in the figure. Moreover, as $|G_{2,11}(s, \omega_r^{(2)})|$ has a maximized steady-state contribution, shown by the flat-line region at low frequencies, it can be directly concluded that (5.30) is satisfied in this case. This is not necessarily the case when $\omega_r \neq \omega_n$, as exemplified by $\omega_r^{(1)}$ and $\omega_r^{(3)}$. In both cases, the absence of any differential and integral actions in $G_{2,12}(s, \omega_r)$ results in flat magnitudes at low frequencies but with higher gains compared to $G_{2,11}(s, \omega_r)$; thus, cross-coupling is present for the lower frequency region of interest. Hence, it may be preferred to utilize $G_{2,12}(s, \omega_r)$ for control due to these higher gains at these operating conditions. Nevertheless, additional complexity arises in doing so as a 180° of phase difference presents in $\angle G_{2,12}(0, \omega_r)$ (shown by arrows 1 and 3 in the figure). This infers that a gain sign flip occurs when the turbine switches operating regime from $\omega_r < \omega_n$ to $\omega_r > \omega_n$ and vice versa, which may result in instability.

Also noticeable in Fig. 5.5b is the presence of two resonance peaks in $|G_2(s, \omega_r)|$ for $\omega_r^{(1)}$ and $\omega_r^{(3)}$ with their magnitudes being -6 dB lower than that of $|G(j\omega_n)|$. These two peaks originate from the shift of the nominal plant's natural frequency into $|\omega_n \pm \omega_r^{(i)}|$ due to the $D(s_{\pm})$ terms in (5.28)-(5.29), which also explains why only a single peak presents for $\omega_r^{(2)}$ case [58]. Although there is significant coupling in higher frequencies in the off-diagonal, only the low-frequent region is of interest for the controller design.

The above observation on the magnitude and phase mapping between both plant representations can be understood better by taking another look at (5.28)-(5.29). First, since both $G_{2,11}(s, \omega_r)$ and $G_{2,12}(s, \omega_r)$ are constituted by the same poles, whether or not (5.30) is satisfied depends only on the zeros of these transfer functions. Secondly, as these zeros are located at $z_{1,2} = \pm \sqrt{\omega_n^2 - \omega_r^2}$, they can be either purely on the imaginary axis, origin, or real axis, depending on the value of the rotational speed of the turbine with respect to the tower's natural frequency. This creates different (steady-state) phase behavior for $\omega_r < \omega_n$ and $\omega_r > \omega_n$ because the latter produces a right-half plane (RHP) zero at the dominant channel such that the aforementioned 180° phase difference/sign flip occurs. Therefore, to ensure main-diagonal dominance for the entire turbine operating range and elimination of the phase drop in the dominant channels, it becomes compelling to manipulate the zero locations of $G_{2,11}(s, \omega_r)$ and $G_{2,12}(s, \omega_r)$. In Section 5.5, both goals can be achieved simultaneously by the inclusion of an offset in the MDC scheme.

Remark 6 Whether \ddot{x} , \dot{x} , or x is used as the output of the plant affects the numerator of $G(s)$ and thus the zeros of (5.28)–(5.29). This also determines how (5.30) is satisfied for different operating points. Nevertheless, regardless of the selected output signal, channel cross-coupling and a 180° phase shift in the dominant channel of $G_2(s, \omega_r)$ still exists, which necessitates their compensation by phase offset inclusion.

5.5 Quadrature and In-Phase Channels Decoupling by Phase Offset Inclusion

The MIMO demodulated plant channel cross-coupling, as well as the gain sign flip examined earlier, has uncovered potential challenges in the proposed MDC design. To gain more knowledge on the degree of this coupling for the entire turbine operating range, a more reliable metric, namely the relative gain array, is used in Section 5.5.1. As inferred in Section 5.4, the inclusion of the phase offset ψ_{off} in the MDC plays a key role in the decoupling of the MIMO demodulated plant. In Section 5.5.2, the optimal phase offset value, by which the highest degree of decoupling and gain sign flip correction can be achieved, is discussed.

5

5.5.1 Relative Gain Array Analysis

Relative gain array (RGA), denoted $\Lambda(\cdot)$, is a measure of interaction between multiple control channels [110]. The RGA is used to assess the coupling of the MIMO demodulated system at steady-state $G_2(0, \omega_r)$ as follows:

$$\Lambda(G_2(0, \omega_r)) = G_2(0, \omega_r) \circ G_2(0, \omega_r)^{-T}, \quad (5.31)$$

where ‘ \circ ’ denotes an element-by-element multiplication known as the Hadamard or Schur product.

Figure 5.6 shows the evaluation of $\Lambda(G_2(0, \omega_r))$ for an extended range of rotor operation $\omega_r \in \Omega' = [0, 1.5]$ rad/s, where the magnitude of the main diagonal elements $|\Lambda_{11}| = |\Lambda_{22}|$ is shown by the blue lines and that of the off-diagonal $|\Lambda_{12}| = |\Lambda_{21}|$ is represented by the red lines. As the rows and columns of $\Lambda(G_2(0, \omega_r))$ sum to 1, it is sufficient to mention only $|\Lambda_{11}|$ for the following discussion.

Figure 5.6a depicts the current case where the main diagonal pairings are dominant with $|\Lambda_{11}| = 1$ only about $\omega_r^{(2)} = \omega_n$. Also evident is the increasing off-diagonal dominance as ω_r deviates from ω_n with $|\Lambda_{11}| \approx 0$ at $\omega_r^{(1)}$ and $\omega_r^{(3)}$. This shows agreement with the previous Bode plot observations in Fig. 5.5b and hints that the current input-output pairings preference is not suitable for the entire operating range [110]. Swapping the input-output pairings to the off-diagonal may be preferable but insufficient to account for the negative gain resulting from the 180° phase difference in $\angle G_2(0, \omega_r)$ indicated by the red-shaded region. Figure 5.6b shows an ideal case where $|\Lambda_{11}| = 1$ for the entire operating regime without any gain sign change, as opposed to Fig. 5.6a. In Section 5.5.2, such a condition is shown to be achievable by means of phase offset inclusion in the proposed MDC framework.

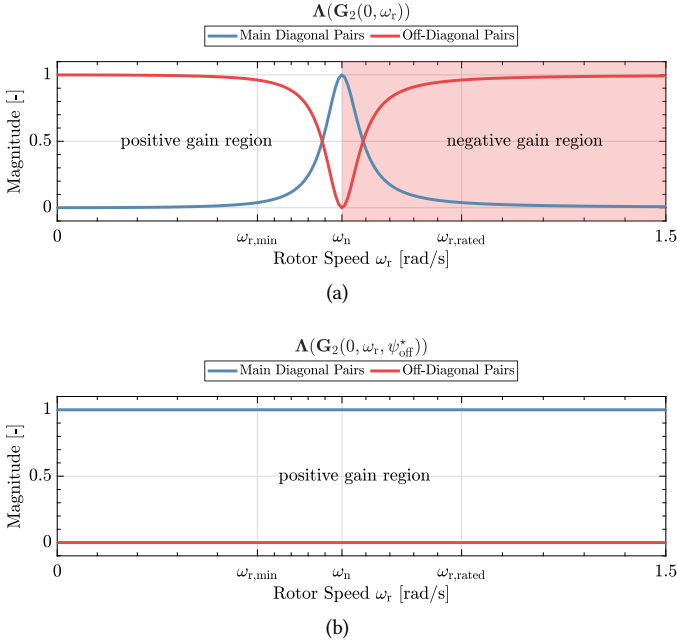


Figure 5.6: Steady-state RGA of $G_2(s, \omega_r)$ over the operating regime of a simple wind turbine model without (a) and with (b) phase offset ψ_{off} . The inclusion of optimal phase offset ψ_{off}^* into the MDC results in decoupled quadrature and in-phase input-output channels at steady-state, as well as eliminating the need for control gain swapping. Please note that for the figures, \dot{x} is measured. In case of x or \ddot{x} , these results, in particular that of (a) will be different (see Remark 6).

5.5.2 Phase Offset Inclusion

In Section 5.4.3, it has been shown that the value of ω_r plays a role in the positioning of the zeros of $G_{2,11}(s, \omega_r)$ and $G_{2,12}(s, \omega_r)$, resulting in both channel cross-coupling and gain sign flip. The previously omitted phase offset ψ_{off} , however, may play a critical role in tackling both issues at the same time by influencing these zero locations. In particular, the optimal phase offset value, defined by

$$\psi_{\text{off}}^*(\omega_r) = -\angle G(j\omega_r), \quad (5.32)$$

can be chosen. As the plant's dynamics vary according to the frequency of the periodic excitation, ψ_{off}^* varies according to ω_r . In the remainder of this chapter, the notation ω_r is dropped when referring to ψ_{off}^* for brevity's sake. This offset value has been rigorously studied in the literature, where methods such as averaging theory, root locus, and loop-shaping have been employed. The interested reader is referred to [57, 111], and references therein for more detailed analysis. The effects of ψ_{off} inclusion on the MIMO demodulated plant and SISO modulated controller are discussed in Sections 5.5.2.1 and 5.5.2.2.

5.5.2.1 Effects of ψ_{off} on MIMO Demodulated Plant

To understand the effects ψ_{off} creates on $G_2(s, \omega_r)$, the derivation done in Section 5.4.2 is repeated by including this offset, which results in the following relation

$$G_2(s, \omega_r, \psi_{\text{off}}^*) = \begin{bmatrix} \frac{e^{j\psi_{\text{off}}^*}G(s_-) + e^{-j\psi_{\text{off}}^*}G(s_+)}{2} & j \frac{e^{j\psi_{\text{off}}^*}G(s_-) - e^{-j\psi_{\text{off}}^*}G(s_+)}{2} \\ j \frac{(-e^{j\psi_{\text{off}}^*}G(s_-) + e^{-j\psi_{\text{off}}^*}G(s_+))}{2} & \frac{e^{j\psi_{\text{off}}^*}G(s_-) + e^{-j\psi_{\text{off}}^*}G(s_+)}{2} \end{bmatrix}, \quad (5.33)$$

in which $\psi_{\text{off}} = \psi_{\text{off}}^*$ is applied. In comparison with the original definition of $G_2(s, \omega_r)$ in (5.26b), $e^{\pm j\psi_{\text{off}}^*}$ terms appear in (5.33) after the inclusion of ψ_{off}^* into the MDC scheme. These terms play a role in zero positioning of both $G_{2,11}(s, \omega_r, \psi_{\text{off}}^*)$ and $G_{2,12}(s, \omega_r, \psi_{\text{off}}^*)$, thereby affecting their (steady-state) gains and phases.

Figure 5.7 depicts the Bode plot of the MIMO demodulated wind turbine model including ψ_{off}^* (5.33). It is apparent that in comparison with the previous case in Fig. 5.5b, the transfer function matrix has now become diagonally dominant, with their phases starting from zero at the steady state and not exhibiting 180° phase difference anymore. This main-diagonal dominance is made clearer by investigating the analytical expressions for the main and off-diagonal elements of the MIMO demodulated plant at steady-state by substituting (5.8) into (5.33) and setting $s = 0$ rad/s, that is

$$G_{2,11}(0, \omega_r, \psi_{\text{off}}^*) = \text{sf} \frac{m \sin(\psi_{\text{off}}^*) \omega_r^3 + d \cos(\psi_{\text{off}}^*) \omega_r^2 - k \sin(\psi_{\text{off}}^*) \omega_r}{d^2 \omega_r^2 + k^2 - 2km\omega_r^2 + m^2 \omega_r^4}, \quad (5.34)$$

and

$$G_{2,12}(0, \omega_r, \psi_{\text{off}}^*) = \text{sf} \frac{-m \cos(\psi_{\text{off}}^*) \omega_r^3 + d \sin(\psi_{\text{off}}^*) \omega_r^2 + k \cos(\psi_{\text{off}}^*) \omega_r}{d^2 \omega_r^2 + k^2 - 2km\omega_r^2 + m^2 \omega_r^4}, \quad (5.35)$$

respectively. Then, the steady-state magnitudes of both the main and off-diagonal elements can be computed for all operating points, where the main diagonal's magnitude equals that of the nominal plant at the excitation frequency

$$|G_{2,11}(0, \omega_r, \psi_{\text{off}}^*)| = |G(j\omega_r)|, \quad (5.36)$$

whereas

$$|G_{2,12}(0, \omega_r, \psi_{\text{off}}^*)| = 0. \quad (5.37)$$

This means that (5.30) is always fulfilled.

Steady-state RGA evaluation of the MIMO demodulated plant after the optimal offset inclusion $\Lambda(G(0, \omega_r, \psi_{\text{off}}^*))$ also confirms the above observation. This is depicted in Fig. 5.6b, where $|\Lambda_{11}| = 1$ for the entire (extended) operating range.

The above observations conclude that under the inclusion of ψ_{off}^* , the main diagonal dominance is asserted and no gain sign flip is experienced as the rotational frequency sweeps through the tower's natural frequency. Therefore, the use of diagonal controller $C(s)$ is now justified.

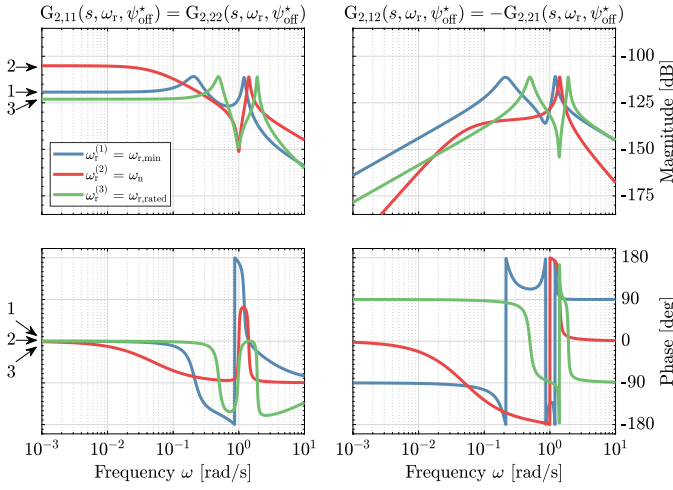


Figure 5.7: Bode plot of the demodulated wind turbine model with the optimal phase offset included $G_2(s, \omega_r, \psi_{\text{off}}^*)$. It is evident that the steady-state off-diagonal contributions are attenuated and that the main diagonal components become dominant.

5.5.2.2 Effects of ψ_{off} on SISO Modulated Controller

Similar to Section 5.5.2.1, the effects of the ψ_{off} inclusion on the SISO modulated controller requires $C_m(s, \omega_r)$ derived in Section 5.4.1 to be reformulated into

$$C_m(s, \omega_r, \psi_{\text{off}}) = e^{-j\psi_{\text{off}}} C(s_-) + e^{j\psi_{\text{off}}} C(s_+). \quad (5.38)$$

Effectively, the LTI controllers (5.18), (5.20), and (5.22) previously proposed are transformed by (5.38) (also by making use of (5.10)) into the following respective (LTV) controllers:

$$C_{m,1}(\psi_{\text{off}}) = 2K_P \cos(\psi_{\text{off}}), \quad (5.39)$$

$$C_{m,2}(s, \omega_r, \psi_{\text{off}}) = \frac{2K_I(\cos(\psi_{\text{off}})s + \sin(\psi_{\text{off}})\omega_r)}{s^2 + \omega_r^2}, \quad (5.40)$$

$$C_{m,3}(s, \omega_r, \psi_{\text{off}}) = \frac{2K_L(\cos(\psi_{\text{off}})(s + \omega_{\text{LPF}}) + \sin(\psi_{\text{off}})\omega_r)}{s^2 + 2\omega_{\text{LPF}}s + \omega_{\text{LPF}}^2 + \omega_r^2}. \quad (5.41)$$

From (5.39)-(5.41), it can be seen that the phase offset ψ_{off} influences the modulated controllers in the following ways. First, for $C_{m,1}(\psi_{\text{off}})$, the phase offset affects the gain of the controller. However, in Section 5.4.2, it has been stated that this controller structure cannot filter out the 2P frequency components; therefore, it is not considered any further during the time-domain demonstration in Section 5.6. For $C_{m,2}(s, \omega_r, \psi_{\text{off}})$, its zero location becomes

$$z_{m,2} = -\omega_r \tan(\psi_{\text{off}}).$$

In the original formulation (5.21), $C_{m,2}(s, \omega_r)$ has a pure zero at the origin but the offset enables relocation of this zero into the left- or right-half plane (LHP or RHP). Similarly,

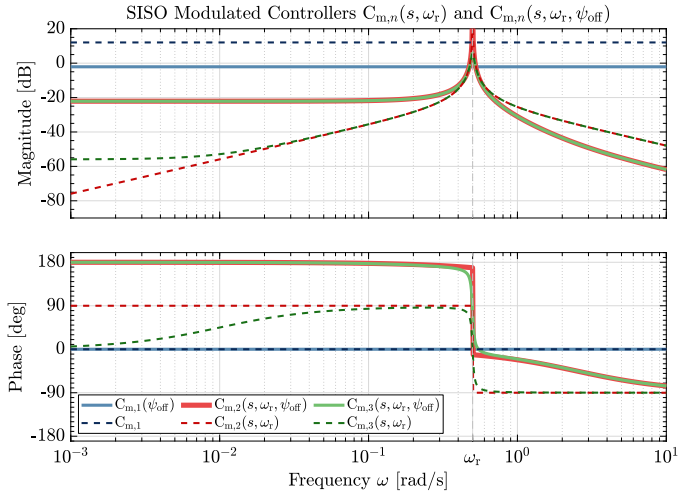


Figure 5.8: Bode plots of SISO modulated controllers, without (dashed lines) and with (solid lines) ψ_{off} , $C_{m,n}(s, \omega_r)$ and $C_{m,n}(s, \omega_r, \psi_{\text{off}})$, respectively, $n = \{1, 2, 3\}$ and $\omega_r = 0.5$ rad/s.

for $C_{m,3}(s, \omega_r, \psi_{\text{off}})$, its zero is relocated from $-\omega_{\text{L呢}}$ into

$$z_{m,3} = -\omega_{\text{L呢}} - \omega_r \tan(\psi_{\text{off}}).$$

An in-depth analysis of the controller zero positioning by this offset is discussed in [57].

Figure 5.8 illustrates the Bode plots of the SISO modulated controllers, similar to that of Section 5.4.1, without and with ψ_{off} . Compared to the inverted notch filters without ψ_{off} , those with the optimal offset included exhibit increased magnitude at the low frequencies due to the introduction of a zero (for $C_{m,2}(s, \omega_r, \psi_{\text{off}})$) or relocation of an existing zero to a high frequency (for $C_{m,3}(s, \omega_r, \psi_{\text{off}})$). For both controllers, the same ψ_{off} is chosen.

5.6 Simulation Results

In this section, simulations demonstrating the performance of the proposed control scheme are carried out. The control scheme consists of the conventional active tower damping controller for increasing the effective damping of the side-side tower motion, as explained in Section 5.2.2. This conventional controller is augmented by the MDC studied earlier in Sections 5.4 and 5.5 to alleviate the periodic 1P fatigue load.

Time-domain simulations at two fidelity levels are considered, where the lower fidelity simulations, discussed in Section 5.6.1, show the proof-of-concept of the MDC framework with the simplified wind turbine model derived earlier. Afterward, high-fidelity simulations employing the National Renewable Energy Laboratory (NREL) OpenFAST software package [112] are covered in Section 5.6.2.

5.6.1 Simplified Turbine Simulations

For the simulations presented here, the wind turbine model derived in Section 5.2 is employed. The synthetic tower properties used in Section 5.4.3 are utilized for the tower

Table 5.1: Parameters of the (modified) NREL-5MW reference wind turbine and environment condition.

| Description | Notation | Value | Unit |
|-------------------------------|---------------------------|---------------------|-------------------------|
| Rated generator power | - | 5 | MW |
| Optimal tip-speed ratio | λ^* | 7 | - |
| Max. power coefficient | C_p^* | 0.458 | - |
| Fine pitch angle | - | 0 | ° |
| Optimal torque gain (LSS) | K | $2.1286 \cdot 10^6$ | Nm/(rad/s) ² |
| LSS equivalent inertia | J_r | $4.0802 \cdot 10^7$ | kgm ² |
| Gearbox ratio | G | 97 | - |
| Rotor radius | R | 63 | m |
| Minimum rotor speed | $\omega_{r,\min}$ | 0.5 | rad/s |
| Rated rotor speed | $\omega_{r,\text{rated}}$ | 1.2 | rad/s |
| Rated generator torque | $T_{g,\text{rated}}$ | 43.09355 | kNm |
| Generator efficiency | - | 0.944 | - |
| Hub height | H | 90 | m |
| Tow. natural frequency (sca.) | $\omega_{n,s}$ | 0.6963 | rad/s |
| Tow. modal mass (sca.) | m_s | $3.6200 \cdot 10^5$ | kg |
| Tow. modal damping (sca.) | d_s | $2.4588 \cdot 10^3$ | Ns/m |
| Tow. modal stiffness (sca.) | k_s | $1.7677 \cdot 10^5$ | N/m |
| Air density | ρ | 1.225 | kg/m ³ |

sca. = scaled

dynamics (5.1). The parameters of NREL 5-MW reference wind turbine [25], as shown in Table 5.1, are used for the rotor dynamics (5.3) and to determine the below-rated torque controller gain according to (5.4).

A steady, uniform, staircase wind inflow from $v = 5$ m/s to $v = 10$ m/s with 1.25 m/s of speed increment is generated for the simulations. Each wind speed lasts for 250 s, resulting in 1250 s of total simulation time. The choice of this wind speed condition is made such that the rotor starts about $\omega_{r,\min}$ at $\omega_r = 0.58$ rad/s and ends near $\omega_{r,\text{rated}}$ at $\omega_r = 1.128$ rad/s, thus covering most of the operating range Ω and that resonance is experienced when $v = 6.25$ m/s at $t = 250 - 500$ s. To model a rotor imbalance, F_{sd} with $a_{sd} = 150$ N and $\phi_{sd} = \pi/4$ rad is selected, equivalent to $a_{sd}/s_f = 9$ kNm of torque amplitude at the tower-top.

Figures 5.9-5.10 depict the performance of the controllers in the MDC scheme, where only the (damped) inverted notch filters are of interest, without and with ψ_{off}^* included. The respective blue and red lines show the former and latter MDCs, whereas the gray lines show the uncontrolled wind turbine responses. In the figures, \dot{x} and ΔT_g measurements are depicted by the top and bottom plots, respectively. For MDCs without ψ_{off}^* , $\psi_{\text{off}} = -90^\circ$ is used for the whole operating range Ω to swap the input-output pairings to the more dominant off-diagonal pairs (see Section 5.5.1). For brevity's sake, the notation $C_{m,n}(s, \omega_r)$ is kept for referring to the pair-swapped MDCs in this section.

The tuning gains for the controllers are chosen to be $K_I = K_L = 1500$ and $\omega_{\text{LPF}} = 0.025$ rad/s by loop-shaping while ensuring stability. During the simulations, the value of ψ_{off}^* , used to decouple the control channels, is determined by means of a look-up table (LUT), fed by filtered rotor measurements where a first-order LPF with a cut-off frequency of 0.2 rad/s is employed.

Figure 5.9 compares the performance of the undamped inverted notch filters $C_{m,2}(s, \omega_r)$

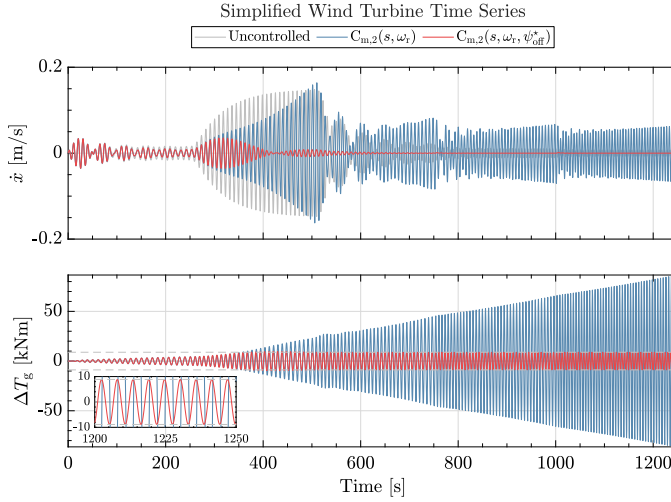


Figure 5.9: Time series response of tower velocity (top) and additive generator torque (bottom) under staircase wind $v = 5 - 10$ m/s where the performance of $C_{m,2}(s, \omega_r)$ and $C_{m,2}(s, \omega_r, \psi_{off}^*)$ are demonstrated. Horizontal dashed lines of ± 9 kNm in the bottom plot indicate the periodic load magnitude's equivalence in terms of torque. A zoomed-in plot depicts control action behavior at the end of the simulation.

5

and $C_{m,2}(s, \omega_r, \psi_{off}^*)$. It is observed from the figure that $C_{m,2}(s, \omega_r)$ does not cancel the 1P periodic loading at the tower as shown in the measurements of \dot{x} . During resonance, tower oscillation starts to grow due to the strong coupling at this frequency as the main-diagonal pairings gain dominance (see Fig. 5.6a). After the resonance, the controller enters the negative gain region (i.e., sign flip occurs) and the growth of ΔT_g becomes unbounded. On the other hand, $C_{m,2}(s, \omega_r, \psi_{off}^*)$ does not exhibit instability and fully cancels the 1P load. The full cancellation of the periodic load is attributed to the infinite gain of the controller at the disturbance frequency. Notice the convergence of the control action's amplitude to 9 kNm (equal to a_{sd}/s_f) as indicated by the horizontal dashed lines and a zoomed-in plot for $t = 1200 - 1250$ s.

Figure 5.10 depicts the performance of the damped inverted notch filters $C_{m,3}(s, \omega_r)$ and $C_{m,3}(s, \omega_r, \psi_{off}^*)$. The differences in both controllers' performance are evident once the wind speed reaches $v = 6.25$ m/s, where resonance starts to occur. The former is shown to dampen the tower's oscillation at about $t = 400 - 450$ s (and slightly beyond when $v = 7.5$ m/s is reached), however not as effective as the latter, shown by the greater reduction in \dot{x} with lower control action. An inset plot at the top highlights that after the resonance, exemplified for $t = 725 - 750$ s, a slight increase in tower oscillation is caused by $C_{m,3}(s, \omega_r)$. On the other hand, evident tower motion reduction is performed by $C_{m,3}(s, \omega_r, \psi_{off}^*)$. In comparison to $C_{m,2}(s, \omega_r, \psi_{off}^*)$ in Fig. 5.9, $C_{m,3}(s, \omega_r, \psi_{off}^*)$ does not fully cancel the 1P periodic loading due to limited gain at ω_r . Nonetheless, maximum ΔT_g magnitude of only ≈ 4.5 kNm is observed in $C_{m,3}(s, \omega_r, \psi_{off}^*)$ contrast to aggressive 9 kNm exhibited by $C_{m,2}(s, \omega_r, \psi_{off}^*)$.

From these simplified wind turbine simulations, it is concluded that ψ_{off}^* is crucial in the load-mitigating performance of the proposed MDCs and in preventing closed-loop insta-

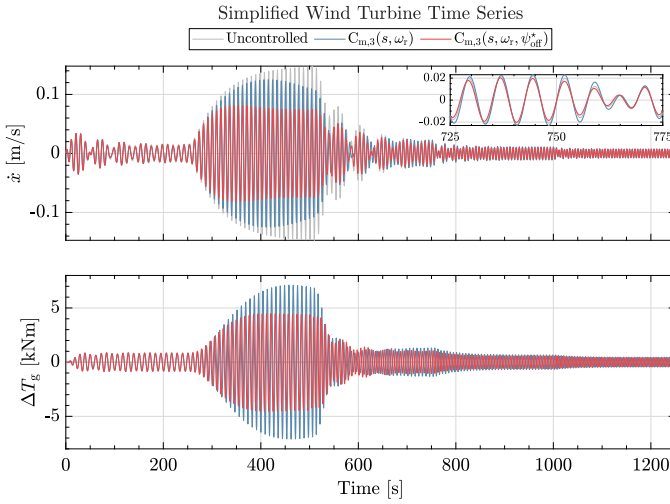


Figure 5.10: Time series response of tower velocity (top) and additive generator torque (bottom) under staircase wind $v = 5 - 10$ m/s where the performance of $C_{m,3}(s, \omega_r)$ and $C_{m,3}(s, \omega_r, \psi_{off}^*)$ are demonstrated. A zoomed-in plot depicts tower velocities at $t = 725 - 750$ s.

bility. Secondly, it can be observed that MDCs perform best in terms of 1P load reduction when $\omega_r = \omega_n$ as their gains are highest at this frequency. This motivates a gain-scheduling strategy to be incorporated into the framework, done in the higher fidelity simulations of the following section.

5.6.2 OpenFAST Simulations

In the high-fidelity OpenFAST simulations presented in this section, the NREL 5-MW reference wind turbine is again used. However, since this reference turbine's tower was originally classified as soft-stiff, its wall thickness is downscaled by a factor of 7.5 to recast it into a soft-soft tower design. This consequently reduces tower mass so that its first natural frequency approximates $\omega_n = 0.7071$ rad/s of the soft-soft tower in the simplified wind turbine setting. The tower modal mass, damping, and stiffness for this scaled tower are denoted respectively as m_s , d_s , and k_s in Table 5.1 and the tower's natural frequency is denoted $\omega_{n,s}$.

For controller design, the reference wind turbine is linearized at the below-rated wind speeds, ranging from $v = 4$ m/s to $v = 10$ m/s with 1 m/s increment. Figure 5.11 shows the Bode plots of the linearized wind turbine (gray lines) for the different operating points, where the transfer from the generator torque to tower velocity is taken. Also plotted is the second order tower model $G(s)$ (black lines), in which modal properties of the scaled reference wind turbine's tower are employed, as well as gain adjustment to fit the linearized wind turbine plots. The gain adjustment is made by setting s_f to 1.667 m^{-1} , which from the physical point of view may infer that, for the employed reference turbine, the prismatic beam assumption as used in (5.1) might be inaccurate. Note that numerical artifacts present in the linearized wind turbine at frequencies lower than 0.01 rad/s, which makes the use of the fitted model $G(s)$ more convenient.

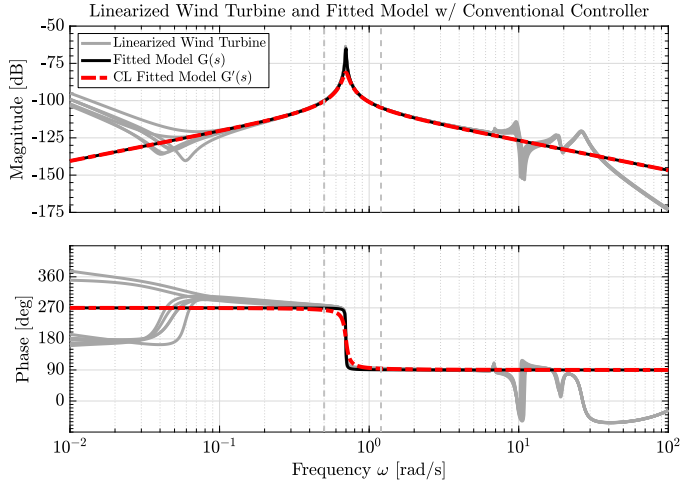


Figure 5.11: Bode plot of linearized NREL 5-MW reference wind turbine and fitted simple model $G(s)$ and closed-loop model with the conventional active tower controller. Vertical dashed lines indicate the operating range of the turbine.

5

Additional damping is added to the lightly-damped $G(s)$ by the conventional active tower damper explained in Section 5.2.2. The gain of the conventional controller is chosen to be $K_{I,conv} = -10000$, which is equivalent to increasing the modal damping into $d_{eff,s} = 1.9125 \cdot 10^4$ Ns/m. The negative sign of $K_{I,conv}$ is needed to account for the difference in the coordinate convention used in the simple model and OpenFAST. In Fig. 5.11, the Bode plot of the fitted plant $G(s)$ in closed-loop with this conventional controller is shown by the red, dashed lines and denoted $G'(s)$.

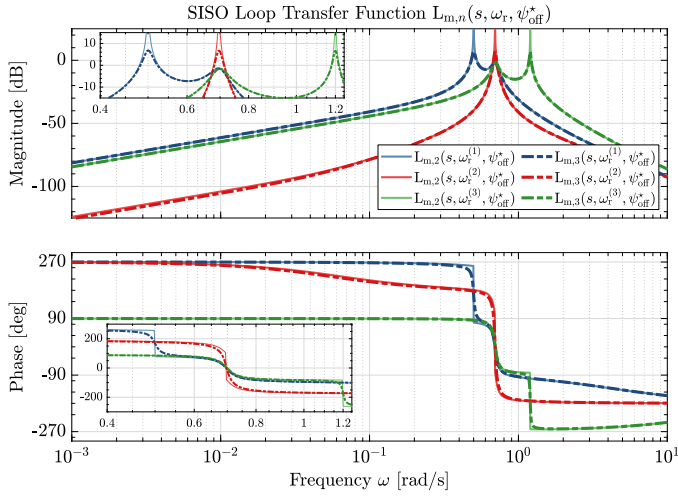
Having a damped tower, the next step is to cascade MDCs on top of the conventional controller. One needs to be reminded that the conventional controller and MDCs serve different purposes and are fundamentally different in that the former increases the effective damping of the tower structure whilst the latter cancels rotational-speed-driven load at the tower. Stated differently, the MDCs can be treated as generalized tower dampers in that they can add more damping to the tower motion not only at a fixed (natural) frequency (such as exemplified in [58]) but also at a varying one, such as used in this work.

Similar to the simple wind turbine simulations, the (damped) inverted notch filters $C_{m,2}(s, \omega_r, \psi_{off}^*)$ and $C_{m,3}(s, \omega_r, \psi_{off}^*)$, with $\omega_{LPF} = 0.01$ rad/s used in the latter, are employed. To cast similar 1P load-reducing performance of MDCs for the entire operating regime, gain-scheduling is implemented by setting the controller gains $K_I = K_L = 0.022\gamma$ with the inverse of the plant's magnitude at the disturbance frequency $\gamma = 1/|G'(j\omega_r)|$ [113] while ensuring stability. Figure 5.12 depicts the resulting Bode plots of the SISO (Fig. 5.12a) and MIMO loop transfer functions (Fig. 5.12b)

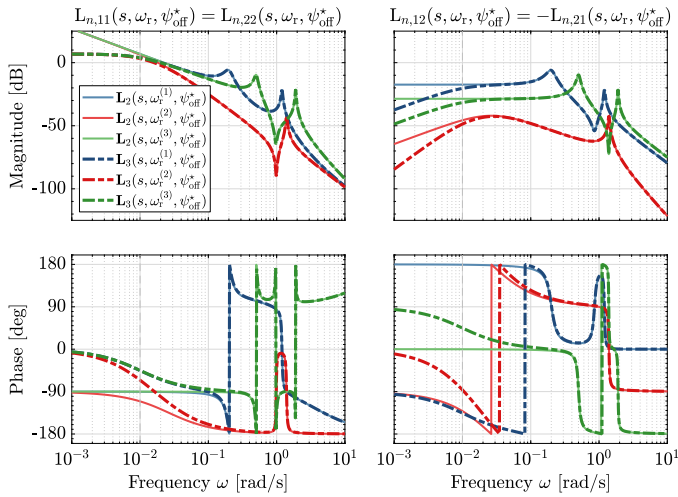
$$L_{m,n}(s, \omega_r^{(i)}, \psi_{off}^*) = G(s)C_{m,n}(s, \omega_r^{(i)}, \psi_{off}^*),$$

and

$$L_n(s, \omega_r^{(i)}, \psi_{off}^*) = G_2(s, \omega_r^{(i)}, \psi_{off}^*)C_n(s),$$



(a)



(b)

Figure 5.12: Bode plots of SISO and MIMO loop transfer functions for $\omega_r^{(i)} = \{\omega_{r,\min}, \omega_{n,s}, \omega_{r,\text{rated}}\}$. In (a), SISO loop transfers with an undamped inverted notch filter and a damped inverted notch filter are depicted with the respective solid and dashed lines. The corresponding transformed MIMO transfers are shown in (b), where the solid lines illustrate the MIMO demodulated plant with an integral controller and dashed lines with a low-pass filter.

respectively, where $\omega_r^{(i)} = \{\omega_{r,\min}, \omega_{n,s}, \omega_{r,\text{rated}}\}$. During the constant and turbulent wind cases that follow, the information of γ and $\psi_{\text{off}}^* = \angle G'(j\omega_r)$ (for decoupling the control channels) are fed into the MDCs by LUTs, making use of low-pass-filtered rotor speed measurements with the same cut-off frequency as used in the simple wind turbine simulations.

5.6.2.1 Constant Wind Simulations

Steady, uniform constant wind cases at $v = \{5, 6.25, 10\}$ m/s, each lasting for 1000 s, are employed for simulations in this section, which produce rotor speeds being lower, equal, and higher than the resonance frequency at steady-state. To induce a 1P excitation to the fixed structure by a rotor mass imbalance, a blade's mass density is lowered by 2% with respect to the original value [53] such that two blades are equally heavier than one other blade.

Figure 5.13 shows the wind turbine tower velocity and total additive generator torque measurements $\Delta T_{g,\text{total}} = \Delta T_{g,\text{damp}} + \Delta T_g$ for these cases, shown during the steady-state at $t = 900 - 1000$ s. The uncontrolled wind turbine signals are shown by the gray lines and those with only the conventional controller $C_{\text{conv}} = K_{\text{conv}}$ are shown by the blue lines. The conventional tower damper targets fatigue loading at the tower's natural frequency, while tower excitations at other frequencies are not alleviated as effectively, especially the 1P-driven load. This is evident in the figure, where the conventional controller performs well only in the second steady wind case where $\omega_r = \omega_n$.

Nevertheless, some residual oscillations are still shown. The performance of C_{conv} is improved by cascading it with the MDCs $C_{m,2}(s, \omega_r, \psi_{\text{off}}^*)$ and $C_{m,3}(s, \omega_r, \psi_{\text{off}}^*)$, illustrated by the respective red and green lines. Similar to the simplified wind turbine simulations in Section 5.6.1, the infinite gain of $C_{m,2}(s, \omega_r, \psi_{\text{off}}^*)$ at the 1P frequency creates the most control effort in every case compared to other settings. This consequently allows the controller to mitigate most of the periodic loads while still providing damping at the tower's natural frequency. Less 1P load reduction due to the less aggressive control action at this frequency is demonstrated when C_{conv} is combined with $C_{m,3}(s, \omega_r, \psi_{\text{off}}^*)$, while still outperforming C_{conv} without MDCs. Also noticeably different than the simplified wind turbine simulations is the effect of the gain-scheduling of the MDCs, such that the effectiveness of the 1P load reduction is not only observed during the resonance but also when $\omega_r < \omega_n$ at $v = 5$ m/s and $\omega_r > \omega_n$ at $v = 10$ m/s.

Remark 7 *The rotor mass imbalance creates greater centrifugal force when the rotor spins faster, resulting in greater 1P loading amplitude at higher rotational speeds, in contrast to the constant amplitude assumed in simplified wind turbine simulations. This explains the need for larger control action of the cascaded controllers for higher rotor speeds.*

5.6.2.2 Turbulent Wind Simulations

Two Kaimal turbulent cases are chosen based on the International Electrotechnical Commission (IEC) 61400-1 standard [114] with $v_h = 6.25$ m/s of mean wind speed at hub height. Turbulence intensities of $I_T = 4\%$ and $I_T = 12\%$ are selected to represent low and high turbulence, respectively. For these wind cases, 2000 s of simulations are run, where the first 200 s is not accounted for to exclude transient effects from the analysis. The same rotor mass imbalance from the steady wind simulations is used here to induce 1P loading.

Results of these turbulent cases are presented in Fig. 5.14. Figure 5.14a depicts the time series results, where records at $t = 875 - 1075$ s and $t = 1575 - 1775$ s are shown for the respective low and high turbulence cases. In the figure, v , ω_r , \dot{x} , and $\Delta T_{g,\text{total}}$ measurements are shown from the first to the fourth rows, respectively. Also indicated by the red dashed lines in the measurements of v and ω_r are v_h and ω_n . Figure 5.14b depicts the

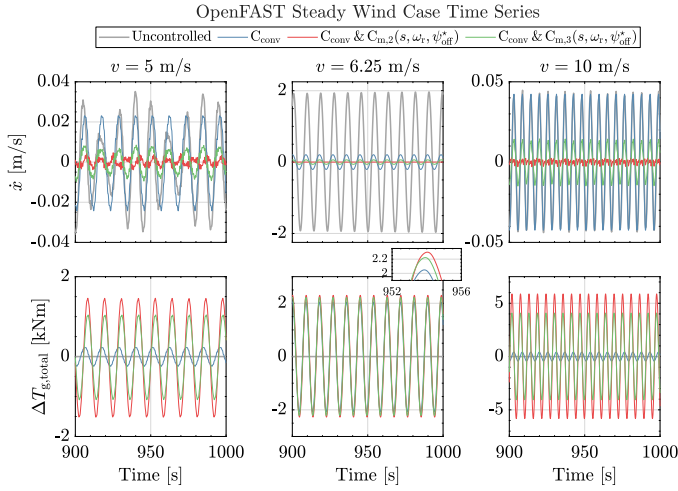


Figure 5.13: OpenFAST time series results in constant wind cases $v = \{5, 6.25, 10\}$ m/s. During the steady-state at $t = 900 - 1000$ s, a large portion of the tower load is mitigated by the conventional controller cascaded with MDCs where $C_{m,2}(s, \omega_r, \psi_{\text{off}}^*)$ yields the most reduction. Increased controller input at higher wind speeds is caused by the greater amplitude of the 1P periodic load.

5

corresponding power spectral density (PSD) plots of \dot{x} and $\Delta T_{g,\text{total}}$, post-processed from the time series measurements. In low turbulence where v varies closer to v_h , ω_r tends to cause tower resonance more frequently compared to when turbulence is higher. This explains the higher PSD magnitude of \dot{x} about ω_n (gray dashed lines) during low turbulence with respect to its higher turbulent counterpart. Regarding controllers' activity, results consistent with the previous steady wind simulations are observed in the two turbulence cases. In the time series, C_{conv} is shown to perform less effectively than when operated in conjunction with MDCs. In terms of load reduction, C_{conv} with $C_{m,2}(s, \omega_r, \psi_{\text{off}}^*)$ performs best. More benign control action is exercised when $C_{m,3}(s, \omega_r, \psi_{\text{off}}^*)$ is incorporated but resultingly, slightly less reduction in tower fatigue load is performed.

The capabilities of the MDCs to follow and cancel the varying 1P periodic load frequency are shown best by the high turbulence case, where 1P frequency varies more and covers a wider range than in low turbulence. This is most evident in the PSD result of \dot{x} , lower frequency content with respect to C_{conv} is evident not only at ω_n but also at the surrounding frequencies. In the PSD plot of $\Delta T_{g,\text{total}}$ in Fig. 5.14b, multiple peaks at 0.6, 0.63, 0.74, and 0.78 rad/s are seen for the cascaded controller settings, apart from that at ω_n . This indicates intensive 1P load reduction activity at the said frequencies, which are virtually non-existent except at 0.74 rad/s for the C_{conv} setting.

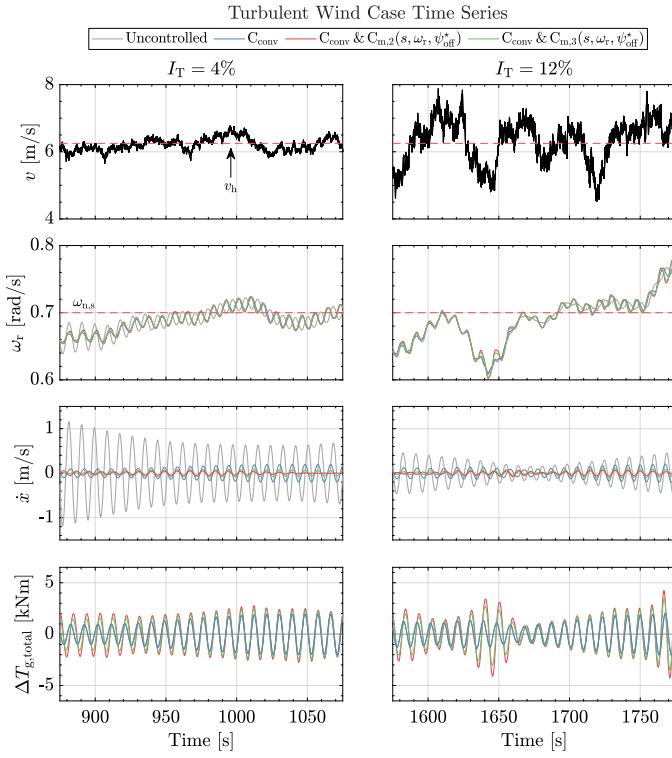
A statistical evaluation of the measurement data from the simulations is done in terms of standard deviations. Table 5.2 summarizes those of the side-side tower velocity $\sigma_{\dot{x}}$, total additive generator torque $\sigma_{\Delta T_{g,\text{total}}}$, and generated power σ_{P_g} . Respectively, these values indicate changes in the side-side tower fatigue load, controller activity, and power fluctuation. While the tower load control methods aim to mitigate side-side tower load, its influence on the fore-aft tower load is also of interest; therefore, the standard deviation

Table 5.2: Standard deviations of side-side tower velocity $\sigma_{\dot{x}}$, fore-aft tower velocity $\sigma_{\dot{x}_{fa}}$, total additive generator torque $\sigma_{\Delta T_{g,total}}$, and generated power σ_{P_g} , as well as mean generated power μ_{P_g} for the turbulent wind cases.

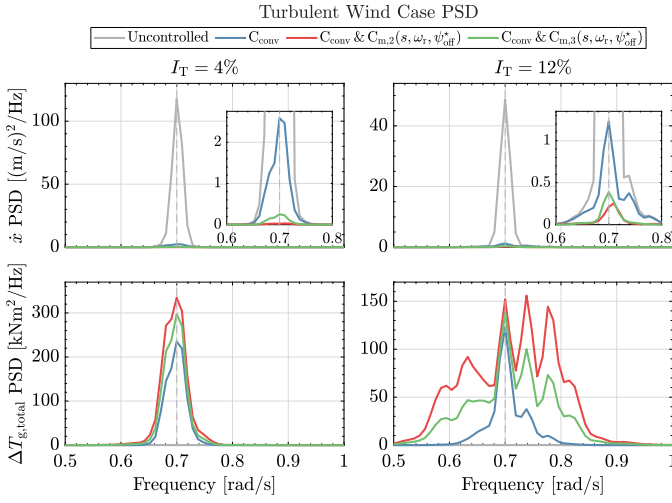
| I_T (%) | Controller | $\sigma_{\dot{x}}$ (m/s) | $\sigma_{\dot{x}_{fa}}$ (m/s) | $\sigma_{\Delta T_{g,total}}$ (kNm) | σ_{P_g} (kW) | μ_{P_g} (kW) |
|--------------|--|-----------------------------|----------------------------------|--|------------------------|---------------------|
| 4 | Uncontrolled | 0.646 | 0.018 | 0 | 67.924 | 825.023 |
| | C_{conv} | ↓ 0.126 | ↓ 0.013 | ↑ 1.263 | ↑ 113.249 | ↑ 825.708 |
| | $C_{conv} \& C_{m,2}(s, \omega_r, \psi_{off}^*)$ | ↓ 0.016 | ↓ 0.015 | ↑ 1.638 | ↑ 132.500 | ↑ 825.769 |
| | $C_{conv} \& C_{m,3}(s, \omega_r, \psi_{off}^*)$ | ↓ 0.041 | ↓ 0.014 | ↑ 1.476 | ↑ 123.685 | ↑ 825.775 |
| 12 | Uncontrolled | 0.393 | 0.021 | 0 | 201.579 | 842.690 |
| | C_{conv} | ↓ 0.095 | ↓ 0.020 | ↑ 0.945 | ↑ 212.809 | ↓ 842.662 |
| | $C_{conv} \& C_{m,2}(s, \omega_r, \psi_{off}^*)$ | ↓ 0.041 | ↑ 0.023 | ↑ 1.953 | ↑ 245.641 | ↑ 842.828 |
| | $C_{conv} \& C_{m,3}(s, \omega_r, \psi_{off}^*)$ | ↓ 0.047 | 0.021 | ↑ 1.525 | ↑ 229.328 | ↑ 842.716 |

↑ / ↓: increase/decrease w.r.t. uncontrolled wind turbine.

of the fore-aft tower velocity $\sigma_{\dot{x}_{fa}}$ is also computed. For the sake of completeness, the mean generated power μ_{P_g} is used to assess changes in the average power production due to the controllers' activities. Upward (↑) and downward (↓) arrows are used to indicate standard deviation and mean values that are higher and lower with respect to the uncontrolled turbine. The overall computed $\sigma_{\dot{x}}$ and $\sigma_{\Delta T_{g,total}}$ for both turbulent cases point to the same conclusion as the time series and PSD results. Best fatigue load reduction, shown by the least $\sigma_{\dot{x}}$ values, is achieved by C_{conv} and $C_{m,2}(s, \omega_r, \psi_{off}^*)$, the control action of which is also the most active, as indicated by the corresponding $\sigma_{\Delta T_{g,total}}$. With respect to this configuration, C_{conv} and $C_{m,3}(s, \omega_r, \psi_{off}^*)$ are able to compromise between the actuation effort and load mitigation, shown by their milder $\sigma_{\Delta T_{g,total}}$ from which slightly lower $\sigma_{\dot{x}}$ is obtained. Again, C_{conv} shows the least increase in $\sigma_{\Delta T_{g,total}}$ with respect to the uncontrolled case, but also the least load reduction among other controller setups. Results from $\sigma_{\dot{x}_{fa}}$ computation indicate that the side-side tower load controllers only slightly affect the fore-aft tower motion, in contrast to $\sigma_{\dot{x}}$. As torque fluctuation affects the generator power due to their proportional relation, the trend of σ_{P_g} follows that of $\sigma_{\Delta T_{g,total}}$. Important to note here is during the high turbulence, generated power fluctuates more due to the high variation in the wind, thus the much higher overall standard deviation with respect to the low turbulence case. Improvements in terms of power fluctuation may be achieved by utilization of individual blade pitching in place of additive generator torque due to the less coupling with the generator power [84]. However, implementing side-side tower periodic load cancelation by individual blade pitching methods is outside the scope of this chapter and is a subject of future work. That said, the computed μ_{P_g} shows that the controllers do not lead to significant changes in the average power production, which indicates that the proposed method can still be desirable. Having the simulation results analyzed, the conclusions of this work are drawn in the next section.



(a)



(b)

Figure 5.14: Time series (a) and PSD (b) results of the turbulent wind cases. Cascaded conventional tower damper and MDCs outperform the conventional controller without MDCs in both low and high turbulence. For $v_h = 6.25$ m/s, different turbulence intensities influence the prevalence of resonances, as shown in (a), thereby affecting the PSD content about $\omega_{n,s} = 0.6963$ rad/s (gray dashed lines) in (b). Greater variation in the 1P frequency during high turbulence results in the cascaded controllers actively operating in a wider frequency range to mitigate the periodic load, shown clearly in the PSD of $\Delta T_{g,total}$.

5.7 Conclusions

In this chapter, an MDC framework for the cancellation of 1P periodic loading acting on wind turbine side-side tower motion has been proposed. The framework relies on the modulation of input and demodulation of output signals at the periodic load frequency, resulting in each signal being representable in its quadrature and in-phase components. Convenient yet effective diagonal LTI controllers are designed onto these channels, representable as an LTV when combined with the modulation-demodulation. MIMO representation of the plant has also been rendered in terms of the quadrature and in-phase channels, which, by frequency-domain analysis, has been shown to contain cross-coupling at steady-state and instability-inducing gain sign flip. A phase offset, the optimal value of which is defined as the negative of the nominal plant's phase at the 1P frequency, has been shown to be a remedy for both the cross-coupling and gain sign flip issues. Simulations at two different levels of fidelity have been conducted to demonstrate the effectiveness of two proposed MDC designs, being undamped and damped inverted notch filters centered at the 1P frequency. Low-fidelity simulations exhibited the controllers' performance deterioration and instability when the optimal phase offset was not incorporated. OpenFAST was employed to simulate steady and turbulent wind cases in a higher-fidelity setting, in which the MDCs are cascaded with a conventional tower damping controller. Results have indicated a performance improvement of the conventional controller in fatigue load reduction when the MDCs are operated synergetically. The conventional tower damper has been shown to mitigate only the tower's natural frequency, while the MDCs target the 1P periodic loading caused by a mass imbalance in the rotor disk. Suggestions for future work include combining MDC and frequency-skipping methods, incorporating individual blade pitching for periodic side-side tower load cancelation, and implementation for canceling higher harmonic structural loads such as 3P for three-bladed turbines.

6

Conclusions and Recommendations

6.1 Conclusions

In this thesis, contributions in the wind turbine control field have been made toward establishing a unified convex economic model predictive control (CEMPC) framework. It can be regarded that a common feature shared by each contribution is the utilization of various coordinate transformations. The variable mapping from nominal terms into that of power and energy has led to the convexity of the power-and-energy CEMPC, which enables globally optimal control solutions and real-time deployment. Then, rendering an extended demodulated model for the periodic side-side tower load estimation has been made possible by applying a model demodulation transformation (MDT) to a nominal wind turbine model. Lastly, the (de)modulations used in the modulation-demodulation control (MDC) method have established an active periodic side-side tower load cancellation scheme, improving a conventional tower damper's performance with which the MDCs have been cascaded. Thus, the advancements in state-of-the-art wind turbine control have been made possible by appropriate uses of coordinate transformations. More importantly, the elements toward having a unified CEMPC framework, where the benefits of both power-and-energy CEMPC and quasi-linear parameter-varying model predictive control (qLPV-MPC) can be further harnessed, have been provided in this thesis.

In Chapters 2 and 3, the power-and-energy CEMPC's load mitigation aspects have been extended, accounting for side-side tower load and blade loads, respectively. These extensions have contributed to the introduction of individual pitch control (IPC) to the framework, by which effective alleviation of the said loads has been successfully performed in mid-fidelity simulations alongside power optimization objectives. Employment of IPC within this framework is advantageous in that not only globally optimal solution is guaranteed, but also the trade-off between actuation rate-of-change (ROC) and load attenuation, being the controller's economic objectives in this case, can be calibrated with convenience.

Generally, lowering actuation ROC penalization and increasing load reduction objectives have resulted in good structural damping at the expense of more active blade pitching. However, blade pitching in the side-side tower load mitigation case is exercised at low frequency, which may not significantly influence pitch actuator wear and tear. The side-side tower base bending moment's damage equivalent load (DEL) has resultingly been reduced with minimal impact on those of the blade flapwise and edgewise moments, as well as power quality, with respect to a basic CEMPC.

For blade loads alleviation, the blades pitch at the once-per-revolution (1P) frequency as the controller aims to mitigate the out-of-plane (OoP) blade root bending moments at the same frequency due to asymmetric load posed by spatiotemporal variability in the wind. Comparison with a conventional IPC has shown similar fatigue load reduction performance of the rotating OoP blade root bending moments and low-speed shaft, as well as fixed yaw bearing yaw moments. At times, during high wind speed and high turbulence intensity, the blade pitch ROC may violate the reference turbine pitch rate limit, which is not necessarily unexpected as explicit pitch ROC constraints have not yet been implemented in the optimal control problem (OCP).

Apart from the aforementioned contributions within the power-and-energy CEMPC scope, other contributions in this thesis have been dedicated to providing advanced control solutions for supporting soft-soft wind turbine tower technology. In Chapter 4, a periodic

tower load estimation scheme has been established, where the periodic loading arising from a rotor imbalance exacerbates the resonance of the side-side tower flexural mode. In a simplified wind turbine simulation setup, the Kalman filter (KF) incorporating a demodulated wind turbine model has been able to estimate the unknown periodic loading and tower states in their slow-varying, demodulated representations in good agreement with the reference. Such a periodic loading estimate could then be utilized to provide control algorithms, such as qLPV-MPC, for active disturbance rejection of this loading.

Despite the attractiveness of the qLPV-MPC with an active periodic load rejection idea, the absence of an active periodic load control design still needs to be addressed in a classical manner. Therefore, Chapter 5 has been dedicated to synthesizing a periodic side-side tower load control by MDC techniques. The proposed scheme has been cascaded with a conventional side-side tower damper control to enhance its load mitigation efficacy, demonstrated by simulations at different fidelities. While the conventional tower damper alone effectively lowers tower load at frequencies at and about the tower's first mode, its effectiveness in counteracting the time-varying 1P periodic load has been improved after cascading with the MDCs. When partial load cancelation is desired, for instance, to minimize the influence of the generator torque control input on the power quality, the MDC structure can be easily adjusted from an integrator to a low-pass filter, resulting in more benign actuation. This control scheme also provides a convenient solution to the channel coupling and gain sign flip by a phase offset inclusion, which has been analyzed in the frequency domain and shown to improve the controller's performance and stability.

6.2 Recommendations

This thesis has exhibited the efforts made toward establishing a unified CEMPC framework. Nevertheless, further improvements could be made for future research, for which the following recommendations are given.

1. With the extensions of the power-and-energy CEMPC developed in this thesis to mitigate side-side tower fatigue load and blade loads, combining other, already established fatigue mitigation features is a possible next step. This comprises fore-aft tower damping, such as done in [52], which may also include second tower modes [83]. With multiple load mitigation and power production optimization objectives, weight tuning may become more intricate as several objectives need to be satisfied simultaneously. To this end, Pareto front/curve may be employed [115] to find the best weight configuration. However, care must be taken in terms of real-time feasibility, as including additional objectives and structural modes into the optimization control problem may result in a higher computational load.
2. Concerning state estimation in the power-and-energy CEMPC framework, a single, unified state estimator could be developed. Although modularity is an advantage in having multiple state estimators, with each serving a different purpose, having a single estimator might be more practical regarding maintainability and ease of troubleshooting. Moreover, benefits in terms of estimation quality might also be achieved by the interactions between states combined with multiple incoming measurements. The scalability of the chosen estimation method is also crucial, particularly for estimating more unknown quantities due to the incorporation of addi-

tional structural modes, as mentioned in the previous recommendation. Additionally, wind speed estimation, which only provides the CEMPC with wind speed information at the current time instance, may be replaced with preview wind information such as from light detection and ranging (LIDAR) equipments [64] to enhance not only load reduction performance but also power production.

3. In this thesis, side-side wind turbine tower dynamics have been modeled in several manners, using either generator torque or individual blade pitching. Each actuation method has its advantages and disadvantages; the former influences power quality when used for tower damping but is more straightforward to design, whereas the latter poses more risk to actuation wear and tear but has less influence on the power quality. Incorporating both actuation methods into the tower dynamics would pose a control allocation problem; however, it might be beneficial when an actuation method is mostly desired in a particular situation, e.g., fault event and actuator wear minimization [116].
4. The periodic load estimation presented in Chapter 4 utilizes an extended demodulated wind turbine model for the internal model of the KF derived using MDT. To supply the KF with tower-top acceleration data in a demodulated manner, MSD involving azimuthal and temporal samplings was applied to the actual plant's output. Such signal demodulation, however, introduces delays that deteriorate the KF's performance such that delay-proofing the state estimator is needed in future work, for instance, by including the model of the signal demodulation mechanism in the internal KF model. Moreover, as the study used a simple wind turbine model, further validation of the estimation scheme within a higher-fidelity simulation environment is necessary.
5. Having the periodic load estimation ready, the next step that could be taken in future research is to incorporate the periodic load estimation into the qLPV-MPC of [53]. This requires the more representative extended demodulated model derived in Chapter 4 to be incorporated in place of the original demodulated model. Having the generator torque contribution to the side-side tower motion modeled allows for the periodic load to be actively canceled. Moreover, combining frequency skipping and active load cancelation in the same qLPV-MPC scheme may result in improved tower load reduction performance.
6. In the MDC development, a demodulated wind turbine representation in the quadrature and in-phase channels has been rendered. This demodulated model resembles that derived by the MDT method, e.g., in Chapter 4 or the work of [53]. Therefore, it is suggested to study whether the model demodulation in the MDC and the MDT methods are equivalent. In addition, since the development of the MDC method has shown the importance of an optimal phase offset in rendering both control channels decoupled, it might be necessary to show whether such an optimal offset is also necessary for the derivation by MDT.

A

Turbulent Wind Case Simulation Results

Table A.1: Baseline controllers and CEMPC-IPC results in moment standard deviations and cumulative pitch travel distance.

| v_0 (m/s) | 16 | | | | 20 | | | |
|--------------------|---|----------|----------|----------|----------|----------|----------|----------|
| | 4 | 8 | 12 | 16 | 4 | 8 | 12 | 16 |
| I_T (%) | | | | | | | | |
| | Mean standard deviation of OoP blade root bending moments ($\sigma_{M_{op,123}}$) | | | | | | | |
| Baseline (kNm) | 841.420 | 1061.333 | 1372.230 | 1726.434 | 1078.221 | 1286.137 | 1589.222 | 1994.160 |
| Baseline IPC (kNm) | 350.948 | 685.019 | 1058.651 | 1434.220 | 396.018 | 753.735 | 1144.278 | 1630.281 |
| CEMPC-IPC (kNm) | 341.486 | 632.300 | 926.773 | 1264.573 | 396.053 | 728.194 | 1098.685 | 1514.710 |
| | Standard deviation of rotating low-speed shaft ($\sigma_{M_{lss}}$) | | | | | | | |
| Baseline (kNm) | 1100.345 | 1278.814 | 1522.350 | 1799.263 | 1474.161 | 1676.542 | 1962.194 | 2310.552 |
| Baseline IPC (kNm) | 375.454 | 622.960 | 894.843 | 1176.211 | 483.679 | 816.804 | 1171.619 | 1546.930 |
| CEMPC-IPC (kNm) | 404.949 | 638.005 | 890.900 | 1200.994 | 501.051 | 806.703 | 1141.918 | 1518.826 |
| | Standard deviation of fixed yaw bearing yaw moment ($\sigma_{M_{yb}}$) | | | | | | | |
| Baseline (kNm) | 384.151 | 712.070 | 1052.017 | 1392.475 | 478.646 | 894.101 | 1317.172 | 1748.134 |
| Baseline IPC (kNm) | 343.325 | 607.805 | 887.502 | 1174.124 | 438.233 | 771.345 | 1121.147 | 1490.183 |
| CEMPC-IPC (kNm) | 359.330 | 606.845 | 875.353 | 1161.360 | 449.448 | 769.436 | 1109.004 | 1479.080 |
| | Cumulative pitch travel distance (β_{tot}) | | | | | | | |
| Baseline (deg) | 130.062 | 264.841 | 408.633 | 559.424 | 149.628 | 300.342 | 453.346 | 614.807 |
| Baseline IPC (deg) | 2014.433 | 2096.757 | 2240.568 | 2438.766 | 2460.793 | 2544.232 | 2678.088 | 2888.781 |
| CEMPC-IPC (deg) | 2131.821 | 2473.935 | 2983.453 | 3618.730 | 2598.891 | 3034.297 | 3596.848 | 4416.405 |

Bibliography

References

- [1] H. Lee and J. Romero (eds.). *Summary for Policymakers*. IPCC, Geneva, Switzerland, 2023.
- [2] UNFCCC. The paris agreement: Unfccc, Oct 2023.
- [3] E. Roston and J. Gu. Is the heat wave caused by climate change? this is what scientists say, Nov 2021.
- [4] J. Horton and D. Palumbo. Europe wildfires: Are they linked to climate change?, Jul 2022.
- [5] F. Davenport. Climate change is making flooding worse: 3 reasons the world is seeing more record-breaking deluges and flash floods, Jul 2023.
- [6] L.W. Foderaro. Climate change has contributed to droughts since 1900, and is likely to get worse, says tree-ring study, May 2021.
- [7] O. Milman. Climate impacts have worsened vast range of human diseases, Aug 2022.
- [8] H. Ritchie, M. Roser, and P. Rosado. Energy mix, Oct 2022.
- [9] Global Wind Energy Council. Global wind report 2022. Report, Global Wind Energy Council, Belgium, 2022.
- [10] P. Veers, K. Dykes, E. Lantz, S. Barth, C. L. Bottasso, O. Carlson, A. Clifton, J. Green, P. Green, H. Holttinen, D. Laird, V. Lehtomäki, J. K. Lundquist, J. Manwell, M. Marquis, C. Meneveau, P. Moriarty, X. Munduate, M. Muskulus, J. Naughton, L. Pao, J. Paquette, J. Peinke, A. Robertson, J. Sanz Rodrigo, A. M. Sempreviva, J. C. Smith, A. Tuohy, and R. Wiser. Grand challenges in the science of wind energy. *Science*, 366(6464):eaau2027, October 2019.
- [11] L. Paddison. The planet saw its hottest day on record this week. it's a record that will be broken again and again, Jul 2023.
- [12] R. Wiser, D. Millstein, M. Bolinger, S. Jeong, and A. Mills. The hidden value of large-rotor, tall-tower wind turbines in the United States. *Wind Engineering*, 45(4):857–871, August 2021.
- [13] T. Burton, N. Jenkins, D. Sharpe, and E. Bossanyi. *Wind Energy Handbook*. John Wiley & Sons, Ltd, Chichester, UK, may 2011.

- [14] K. Dykes, R. Damiani, O. Roberts, and E. Lantz. Analysis of ideal towers for tall wind applications. techreport NREL/CP-5000-70642, National Renewable Energy Laboratory (NREL), Golden, Colorado, January 2018.
- [15] E.A. Bossanyi. Individual Blade Pitch Control for Load Reduction. *Wind Energy*, 6(2):119–128, April 2003.
- [16] S.P. Mulders and J.W. van Wingerden. Delft Research Controller: An open-source and community-driven wind turbine baseline controller. *Journal of Physics: Conference Series*, 1037(3), 2018.
- [17] L. Hartman. Wind turbines: The bigger, the better, August 2023.
- [18] R. Wiser, J. Rand, J. Seel, P. Beiter, E. Baker, E. Lantz, and P. Gilman. Expert elicitation survey predicts 37% to 49% declines in wind energy costs by 2050. *Nature Energy*, 6(5):555–565, May 2021.
- [19] H. Polinder, F.F.A. van der Pijl, G.J. de Vilder, and P.J. Tavner. Comparison of direct-drive and geared generator concepts for wind turbines. *IEEE Transactions on Energy Conversion*, 21(3):725–733, September 2006.
- [20] P.A. Fleming, P.M.O. Gebraad, S. Lee, J.W. van Wingerden, K. Johnson, M. Churchfield, J. Michalakes, P. Spalart, and P. Moriarty. Evaluating techniques for redirecting turbine wakes using SOWFA. *Renewable Energy*, 70:211–218, October 2014.
- [21] M.T. van Dijk, J.W. van Wingerden, T. Ashuri, and Y. Li. Wind farm multi-objective wake redirection for optimizing power production and loads. *Energy*, 121:561–569, February 2017.
- [22] F.D. Bianchi, R.J. Mantz, and H. De Battista. *Wind Turbine Control Systems*. Advances in Industrial Control. Springer London, London, 1 edition, jul 2007.
- [23] L.Y. Pao and K.E. Johnson. A tutorial on the dynamics and control of wind turbines and wind farms. *2009 American Control Conference*, pages 2076–2089, 2009.
- [24] L. Brandetti, S.P. Mulders, Y. Liu, S. Watson, and J.W. van Wingerden. Analysis and multi-objective optimisation of model-based wind turbine controllers. *Wind Energy Science Discussions*, 2023:1–28, 2023.
- [25] J. Jonkman, S. Butterfield, W. Musial, and G. Scott. Definition of a 5-MW Reference Wind Turbine for Offshore System Development. Technical report, National Renewable Energy Laboratory (NREL), Golden, CO, feb 2009.
- [26] E.A. Bossanyi. The Design of closed loop controllers for wind turbines. *Wind Energy*, 3(3):149–163, 2000.
- [27] J. Jonkman. Definition of the Floating System for Phase IV of OC3. Technical Report NREL/TP-500-47535, 979456, National Renewable Energy Lab.(NREL), Golden, CO (United States), Colorado, USA, May 2010.

- [28] N.J. Abbas, D.S. Zalkind, L. Pao, and A. Wright. A reference open-source controller for fixed and floating offshore wind turbines. *Wind Energy Science*, 7(1):53–73, January 2022.
- [29] G. Sieros, P. Chaviaropoulos, J.D. Sørensen, B.H. Bulder, and P. Jamieson. Upscaling wind turbines: Theoretical and practical aspects and their impact on the cost of energy. *Wind Energy*, 15(1):3–17, 2012.
- [30] E.A. Bossanyi. Wind Turbine Control for Load Reduction. *Wind Energy*, 6(3):229–244, jul 2003.
- [31] E.L. van der Hooft, P. Schaak, and T. van Engelen. Wind turbine control algorithms. Technical report, Energy research Centre of the Netherlands ECN, Petten, Netherlands, 2003.
- [32] Z. Zhang, S. Nielsen, F. Blaabjerg, and D. Zhou. Dynamics and Control of Lateral Tower Vibrations in Offshore Wind Turbines by Means of Active Generator Torque. *Energies*, 7(11):7746–7772, November 2014.
- [33] K.A. Stol, W. Zhao, and A.D. Wright. Individual Blade Pitch Control for the Controls Advanced Research Turbine (CART). *Journal of Solar Energy Engineering*, 128(4):498–505, nov 2006.
- [34] D. Duckwitz and M. Geyler. Active damping of the side-to-side oscillation of the tower. In *Proceedings of DEWEK*, volume 49. DEWEK, 2010.
- [35] J. Licari, J.B. Ekanayake, and N. Jenkins. Investigation of a speed exclusion zone to prevent tower resonance in variable-speed wind turbines. *IEEE Transactions on Sustainable Energy*, 4(4):977–984, 2013.
- [36] R. Ramlau and J. Niebsch. Imbalance Estimation Without Test Masses for Wind Turbines. *Journal of Solar Energy Engineering*, 131(1):011010, February 2009.
- [37] F.C. Mehlan and A.R. Nejad. Rotor imbalance detection and diagnosis in floating wind turbines by means of drivetrain condition monitoring. *Renewable Energy*, 212:70–81, August 2023.
- [38] E. Smilden and A.J. Sørensen. Application of a Speed Exclusion Zone Algorithm on a Large 10MW Offshore Wind Turbine. In *ASME 2016 35th International Conference on Ocean, Offshore and Arctic Engineering*. American Society of Mechanical Engineers Digital Collection, October 2016.
- [39] G. Bir. Multi-blade coordinate transformation and its application to wind turbine analysis. *ASME Wind Energy Symposium*, (January):1–15, 2008.
- [40] E.A. Bossanyi, P.A. Fleming, and A.D. Wright. Validation of Individual Pitch Control by Field Tests on Two-and Three-Bladed Wind Turbines. *IEEE Transactions on Control Systems Technology*, 21(4):1067–1078, 2013.

- [41] T.G. van Engelen and E.L. van der Hooft. Individual pitch control inventory. *Technical Report ECN-E-03*, (ECN-C-03-138), 2005.
- [42] P. Novak, T. Ekelund, I. Jovik, and B. Schmidtbauer. Modeling and Control of Variable-Speed Wind-Turbine Drive-System Dynamics. pages 28–38, 1995.
- [43] J. Aho, P. Fleming, and L.Y. Pao. Active power control of wind turbines for ancillary services: A comparison of pitch and torque control methodologies. *Proceedings of the American Control Conference*, 2016-July:1407–1412, 2016.
- [44] D. van der Hoek, S. Kanev, and W. Engels. Comparison of Down-Regulation Strategies for Wind Farm Control and their Effects on Fatigue Loads. In *2018 Annual American Control Conference (ACC)*, pages 3116–3121, June 2018.
- [45] M. Mirzaei, M. Soltani, N.K. Poulsen, and H.H. Niemann. Model based active power control of a wind turbine. *Proceedings of the American Control Conference*, pages 5037–5042, 2014.
- [46] P.A. Fleming, J. Aho, A. Buckspan, E. Ela, Y. Zhang, V. Gevorgian, A. Scholbrock, L. Pao, and R. Damiani. Effects of power reserve control on wind turbine structural loading. *Wind Energy*, 19(3):453–469, 2016.
- [47] C.L. Bottasso, A. Croce, Y. Nam, and C.E.D. Riboldi. Power curve tracking in the presence of a tip speed constraint. *Renewable Energy*, 40(1):1–12, April 2012.
- [48] J.B. Rawlings, D.Q. Mayne, and M. Diehl. *Model predictive control: theory, computation, and design*, volume 2. Nob Hill Publishing Madison, WI, 2017.
- [49] T. Tran, K.V. Ling, and J.M. Maciejowski. Economic model predictive control-A review. *31st International Symposium on Automation and Robotics in Construction and Mining, ISARC 2014 - Proceedings*, (Isarc):35–42, 2014.
- [50] A.J.J. van den Boom and B. De Schutter. Optimization in Systems and Control SC4091. (August), 2011.
- [51] T.G. Hovgaard, S. Boyd, and J.B. Jørgensen. Model predictive control for wind power gradients. *Wind Energy*, 18(6):991–1006, jun 2015.
- [52] M.L. Shaltout, Z. Ma, and D. Chen. An Adaptive Economic Model Predictive Control Approach for Wind Turbines. *Journal of Dynamic Systems, Measurement, and Control*, 140(5):1–10, may 2018.
- [53] S.P. Mulders, T.G. Hovgaard, J.D. Grunnet, and J.W. van Wingerden. Preventing wind turbine tower natural frequency excitation with a quasi-LPV model predictive control scheme. *Wind Energy*, 23(3):627–644, mar 2020.
- [54] A. Keyvani, M.S. Tamer, J.W. van Wingerden, J.F.L. Goosen, and F. van Keulen. A comprehensive model for transient behavior of tapping mode atomic force microscope. *Nonlinear Dynamics*, 97(2):1601–1617, 2019.

- [55] P.S.G. Cisneros, S. Voss, and H. Werner. Efficient Nonlinear Model Predictive Control via quasi-LPV representation. In *2016 IEEE 55th Conference on Decision and Control (CDC)*, number Cdc, pages 3216–3221. IEEE, dec 2016.
- [56] M. Bodson, A. Sacks, and P. Khosla. Harmonic generation in adaptive feedforward cancellation schemes. *IEEE Transactions on Automatic Control*, 39(9):1939–1944, September 1994.
- [57] M.F. Byl, S.J. Ludwick, and D.L. Trumper. A loop shaping perspective for tuning controllers with adaptive feedforward cancellation. *Precision Engineering*, 29(1):27–40, January 2005.
- [58] K. Lau, D.E. Quevedo, B.J.G. Vautier, G.C. Goodwin, and S.O.R. Moheimani. Design of modulated and demodulated controllers for flexible structures. *Control Engineering Practice*, 15(3):377–388, March 2007.
- [59] P. Enevoldsen and G. Xydis. Examining the trends of 35 years growth of key wind turbine components. *Energy for Sustainable Development*, 50:18–26, 2019.
- [60] B. Fischer and M. Shan. A survey on control methods for the mitigation of tower loads. *Fraunhofer IWES Report*, 655, 2013.
- [61] Vestas. General Specification V90-3.0MW: 60 Hz Variable Speed Turbine. Technical report, Vestas Wind Systems A/S, Denmark, 2004.
- [62] J.B. Rawlings, D. Angeli, and C.N. Bates. Fundamentals of economic model predictive control. In *2012 IEEE 51st IEEE Conference on Decision and Control (CDC)*, pages 3851–3861. 2012 IEEE 51st IEEE Conference on Decision and Control (CDC), IEEE, dec 2012.
- [63] K. Selvam, S. Kanev, J.W. van Wingerden, T. van Engelen, and M. Verhaegen. Feedback-feedforward individual pitch control for wind turbine load reduction. *International Journal of Robust and Nonlinear Control*, 19(1):72–91, jan 2009.
- [64] D. Schlipf, D. Johannes Schlipf, and M. Kühn. Nonlinear model predictive control of wind turbines using LIDAR. *Wind Energy*, 16(7):1107–1129, oct 2013.
- [65] Y. Liu, A.K. Pamososuryo, R.M.G. Ferrari, and J.W. van Wingerden. The immersion and invariance wind speed estimator revisited and new results. *IEEE Control Syst. Lett.*, 6:361–366, 2022.
- [66] Y. Liu, A.K. Pamososuryo, S.P. Mulders, R.M.G. Ferrari, and J.W. van Wingerden. The Proportional Integral Notch and Coleman Blade Effective Wind Speed Estimators and Their Similarities. *IEEE Control Syst. Lett.*, 6:2198–2203, 2022.
- [67] B.J. Jonkman and J.M. Jonkman. FAST v8.16.00a-bjj User’s Guide. Technical report, National Renewable Energy Lab.(NREL), Golden, CO (United States), Colorado, USA, 2016.

- [68] MOSEK ApS. *The MOSEK optimization toolbox for MATLAB manual. Version 9.0*. MOSEK ApS, Denmark, 2019.
- [69] G. Hayman. Mlife theory manual for version 1.00. *National Renewable Energy Laboratory, Golden, CO, 74(75):106*, 2012.
- [70] S.P. Mulders, A.K. Pamososuryo, G.E. Disario, and J.W. van Wingerden. Analysis and optimal individual pitch control decoupling by inclusion of an azimuth offset in the multiblade coordinate transformation. *Wind Energy*, 22(3):341–359, mar 2019.
- [71] F. Sandquist, G. Moe, and O. Anaya-Lara. Individual Pitch Control of Horizontal Axis Wind Turbines. *Journal of Offshore Mech. Arctic Eng.-Trans. ASME*, 134(3):31901, 2012.
- [72] M. Geyler and P. Caselitz. Robust Multivariable Pitch Control Design for Load Reduction on Large Wind Turbines. *Journal of Solar Energy Engineering*, 130(3):031014, 2008.
- [73] Q. Lu, R. Bowyer, and B.Ll. Jones. Analysis and design of Coleman transform-based individual pitch controllers for wind-turbine load reduction. *Wind Energy*, 18(8):1451–1468, August 2015.
- [74] M. Vali, J.W. van Wingerden, and M. Kühn. Optimal multivariable individual pitch control for load reduction of large wind turbines. *2016 American Control Conference (ACC)*, pages 3163–3169, 2016.
- [75] J.B. Rawlings. Tutorial overview of model predictive control. *IEEE Control Systems*, 20(3):38–52, June 2000.
- [76] J. Friis, E. Nielsen, J. Bonding, F. Daher Adegas, J. Stoustrup, and P.F. Odgaard. Repetitive model predictive approach to individual pitch control of wind turbines. In *Proceedings of the IEEE Conference on Decision and Control*, pages 3664–3670. Conference on Decision and Control, 2011.
- [77] L.C. Henriksen, M.H. Hansen, and N.K. Poulsen. Wind turbine control with constraint handling: A model predictive control approach. *IET Control Theory and Applications*, 6(11):1722–1734, 2012.
- [78] M. Madsen, J. Filsø, and M. Soltani. Preview-based asymmetric load reduction of wind turbines. In *2012 IEEE International Conference on Control Applications*, pages 1424–1429. 2012 IEEE International Conference on Control Applications CCA), October 2012.
- [79] A. Koerber and R. King. Combined Feedback–Feedforward Control of Wind Turbines Using State-Constrained Model Predictive Control. *IEEE Transactions on Control Systems Technology*, 21(4):1117–1128, July 2013.
- [80] M.A. Evans, M. Cannon, and B. Kouvaritakis. Robust MPC tower damping for variable speed wind turbines. *IEEE Transactions on Control Systems Technology*, 23(1):290–296, 2015.

- [81] S. Gros. An economic NMPC formulation for Wind Turbine Control. *Proceedings of the IEEE Conference on Decision and Control*, pages 1001–1006, 2013.
- [82] S. Gros and A. Schild. Real-time economic nonlinear model predictive control for wind turbine control. *International Journal of Control*, 90(12):2799–2812, 2017.
- [83] Z. Feng, A.J. Gallo, Y. Liu, A.K. Pamososuryo, R.M.G. Ferrari, and J.W. van Wingerden. An Economic Model Predictive Control Approach for Load Mitigation on Multiple Tower Locations of Wind Turbines. In *2022 IEEE 61st Conference on Decision and Control (CDC)*, pages 2425–2430. 2022 IEEE 61st IEEE Conference on Decision and Control (CDC), December 2022.
- [84] A.K. Pamososuryo, Y. Liu, T.G. Hovgaard, R. Ferrari, and J.W. van Wingerden. Individual pitch control by convex economic model predictive control for wind turbine side-side tower load alleviation. In *Journal of Physics: Conference Series*, volume 2265, page 032071. IOP Publishing, May 2022.
- [85] W.H. Lio. *Blade-Pitch Control for Wind Turbine Load Reductions*. Number February in Springer Theses. Springer International Publishing, Cham, 2018.
- [86] S. Raach, D. Schlipf, F. Sandner, D. Matha, and P.W. Cheng. Nonlinear model predictive control of floating wind turbines with individual pitch control. In *Proceedings of the American Control Conference*, pages 4434–4439. American Control Conference, IEEE, June 2014.
- [87] A. Jain, G. Schildbach, L. Fagiano, and M. Morari. On the design and tuning of linear model predictive control for wind turbines. *Renewable Energy*, 80:664–673, aug 2015.
- [88] K.J. Åström and B. Wittenmark. *Computer-controlled systems: theory and design*. Courier Corporation, 2013.
- [89] Y. Liu, A.K. Pamososuryo, R. Ferrari, T.G. Hovgaard, and J.W. van Wingerden. Blade Effective Wind Speed Estimation: A Subspace Predictive Repetitive Estimator Approach. In *2021 European Control Conference (ECC)*, pages 1205–1210. 2021 European Control Conference (ECC), June 2021.
- [90] E.A. Wan and R. Van Der Merwe. The unscented kalman filter for nonlinear estimation. In *Proceedings of the IEEE 2000 Adaptive Systems for Signal Processing, Communications, and Control Symposium (Cat. No.00EX373)*, pages 153–158. IEEE 2000 Adaptive Systems for Signal Processing, Communications, and Control Symposium, 2000.
- [91] S.P. Mulders, M.B. Zaaijer, R. Bos, and J.W. van Wingerden. Wind turbine control: Open-source software for control education, standardization and compilation. *Journal of Physics: Conference Series*, 1452(1):012010, January 2020.
- [92] J. Löfberg. Yalmip : a toolbox for modeling and optimization in matlab. In *2004 IEEE International Conference on Robotics and Automation (IEEE Cat. No.04CH37508)*,

- pages 284–289. 2004 IEEE International Conference on Robotics and Automation, 2004.
- [93] B.J. Jonkman. Turbsim user’s guide v2.00.00. Technical report, National Renewable Energy Lab.(NREL), Golden, CO (United States), Colorado, USA, 2016.
- [94] Iec 61400-3 wind turbines part 3: Design requirements for offshore wind turbines. Standard, International Electrotechnical Commission, Geneva, Switzerland, 2009.
- [95] E. van Solingen and J.W. van Wingerden. Linear individual pitch control design for two-bladed wind turbines. *Wind Energy*, 18(4):677–697, 2015.
- [96] P. Welch. The use of fast Fourier transform for the estimation of power spectra: A method based on time averaging over short, modified periodograms. *IEEE Transactions on Audio and Electroacoustics*, 15(2):70–73, June 1967.
- [97] C.L. Bottasso, A. Croce, C.E.D. Riboldi, and Y. Nam. Multi-layer control architecture for the reduction of deterministic and non-deterministic loads on wind turbines. *Renewable Energy*, 51:159–169, mar 2013.
- [98] M. Verhaegen and V. Verdult. *Filtering and system identification: a least squares approach*. Cambridge university press, 2007.
- [99] A.K. Pamososuryo, S.P. Mulders, R. Ferrari, and J.W. van Wingerden. Periodic load estimation of a wind turbine tower using a model demodulation transformation. In *2022 American Control Conference (ACC)*, pages 5271–5276, June 2022.
- [100] M. Saathoff, M. Rosemeier, T. Kleinselbeck, and B. Rathmann. Effect of individual blade pitch angle misalignment on the remaining useful life of wind turbines. *Wind Energy Science*, 6(5):1079–1087, September 2021.
- [101] A.D. Wright and L.J. Fingersh. Advanced Control Design for Wind Turbines; Part I: Control Design, Implementation, and Initial Tests. Technical Report NREL/TP-500-42437, 927269, March 2008.
- [102] K. Lau, G.C. Goodwin, and R.T. M’Closkey. Properties of modulated and demodulated systems with implications to feedback limitations. *Automatica*, 41(12):2123–2129, December 2005.
- [103] A.H. Sacks, M. Bodson, and W. Messner. Advanced methods for repeatable runout compensation [disc drives]. *IEEE Transactions on Magnetics*, 31(2):1031–1036, March 1995.
- [104] K.B. Ariyur and M. Krstic. Feedback attenuation and adaptive cancellation of blade vortex interaction on a helicopter blade element. *IEEE Transactions on Control Systems Technology*, 7(5):596–605, September 1999.
- [105] Y. Xu, M. de Mathelin, and D. Knittel. Adaptive rejection of quasi-periodic tension disturbances in the unwinding of a non-circular roll. In *Proceedings of the 2002 American Control Conference (IEEE Cat. No.CH37301)*, volume 5, pages 4009–4014 vol.5, May 2002.

- [106] H. Zhong, V. Kulkarni, and L. Pao. Adaptive control for rejecting disturbances with time-varying frequencies in tape systems. In *Proceedings of the 2005, American Control Conference, 2005.*, pages 533–538 vol. 1, June 2005.
- [107] R. Ungurán, V. Petrović, S. Boersma, J.W. van Wingerden, L.Y. Pao, and M. Kühn. Feedback-feedforward individual pitch control design for wind turbines with uncertain measurements. In *2019 American Control Conference (ACC)*, pages 4151–4158. American Control Conference.
- [108] M. Steinbuch. Repetitive control for systems with uncertain period-time. *Automatica*, 38(12):2103–2109, December 2002.
- [109] Y. Liu, R. Ferrari, and J.W. van Wingerden. Load reduction for wind turbines: An output-constrained, subspace predictive repetitive control approach. *Wind Energy Science*, 7(2):523–537, March 2022.
- [110] S. Skogestad and I. Postlethwaite. *Multivariable feedback control: analysis and design*. John Wiley & Sons, 2005.
- [111] W. Messner and M. Bodson. Design of adaptive feedforward algorithms using internal model equivalence. *International Journal of Adaptive Control and Signal Processing*, 9(2):199–212, 1995.
- [112] NREL. Openfast/openfast: Openfast v3.0.0, June 2021.
- [113] C. Hendrickson and R.T. M’Closkey. Phase Compensation Strategies for Modulated-Demodulated Control With Application to Pulsed Jet Injection. *Journal of Dynamic Systems, Measurement, and Control*, 134(1):011024, January 2012.
- [114] International Electrotechnical Commission. IEC 61400-1: Wind turbines part 1: Design requirements. Technical report, 2005.
- [115] P.F. Odgaard, L.F.S. Larsen, R. Wisniewski, and T.G. Hovgaard. On using Pareto optimality to tune a linear model predictive controller for wind turbines. *Renewable Energy*, 87:884–891, mar 2016.
- [116] M. Hanger, T.A. Johansen, G.K. Mykland, and A. Skullestad. Dynamic model predictive control allocation using CVXGEN. In *2011 9th IEEE International Conference on Control and Automation (ICCA)*, pages 417–422, Santiago, Chile, December 2011. IEEE.

Curriculum Vitæ

Born

1991 Born in Medan, Indonesia

Education

2007-2010 De Britto High School, Yogyakarta, Indonesia

2010-2014 Bachelor's degree in Engineering Physics
Bandung Institute of Technology, Bandung, Indonesia

2015-2018 Master's degree in Systems and Control
Delft University of Technology, Delft, Netherlands

2020-2024 Doctoral degree in Systems and Control
Delft University of Technology, Delft, Netherlands
Thesis title: Wind Turbine Load Control and Estimation: Advancements by Coordinate Transformations
Promoters: prof. dr. ir. J.W. van Wingerden, dr. R.M.G. Ferrari, and dr. ir. S.P. Mulders

Award

2023 O. Hugo Schuck Best Paper Award: Application Category from the American Automatic Control Council, San Diego, USA

List of Publications


Journal Publications


6. **A.A.W. van Vondelen, A.K. Pamososuryo, S.T. Navalkar, J.W. van Wingerden.** Control of Periodically-Waked Wind Turbines. Submitted to: *IEEE Transaction in Control Systems Technology*.
5. **A.K. Pamososuryo, S.P. Mulders, R.M.G. Ferrari, J.W. van Wingerden.** On the analysis and synthesis of wind turbine side-side tower load control via demodulation. *IEEE Transaction in Control Systems Technology*, 2024.
4. **A.K. Pamososuryo, Y. Liu, T.G. Hovgaard, R.M.G. Ferrari, J.W. van Wingerden.** Convex economic model predictive control for blade loads mitigation on wind turbines. *Wind Energy* 26 (12), 1276-1298, 2023.
3. **Y. Liu, A.K. Pamososuryo, S.P. Mulders, R.M.G. Ferrari, J.W. van Wingerden.** The proportional integral notch and Coleman blade effective wind speed estimators and their similarities. *IEEE Control Systems Letters* vol. 6, 2022.
2. **Y. Liu, A.K. Pamososuryo, S.P. Mulders, R.M.G. Ferrari, J.W. van Wingerden.** The immersion and invariance wind speed estimator revisited and new results. *IEEE Control Systems Letters* vol. 6, 2022.
1. **S.P. Mulders, G.E. Disario, A.K. Pamososuryo, J.W. van Wingerden.** Analysis and optimal individual pitch control decoupling by inclusion of an azimuth offset in the multiblade coordinate transformation. *Wind Energy* 22 (3), 341-359, 2018.

Conference Proceedings

8. **A.A.W. van Vondelen, A.K. Pamososuryo, S.T. Navalkar, J.W. van Wingerden.** On the optimal azimuth offset for individual pitch control in aeroelastic code coupled with a high-fidelity flow solver. *Accepted for: European Control Conference (ECC)*, Stockholm, Sweden, 2024.
7. **L. Brandetti, Y. Liu, A.K. Pamososuryo, S.P. Mulders, S. Watson, J.W. van Wingerden.** Unscented Kalman filter-based blade-effective wind speed estimation for a vertical-axis wind turbine. In *International Federation of Automatic Control (IFAC) World Congress*, Yokohama, Japan, 2023.
6. **A.A.W. van Vondelen, J. Ottenheim, A.K. Pamososuryo, S.T. Navalkar, J.W. van Wingerden.** Phase synchronization for helix enhanced wake mixing in downstream wind turbines. In *International Federation of Automatic Control (IFAC) World Congress*, Yokohama, Japan, 2023.

5. **A.K. Pamososuryo, S.P. Mulders, R.M.G. Ferrari, J.W. van Wingerden.** Periodic load estimation of a wind turbine tower using a model demodulation transformation. In *American Control Conference (ACC)*, Atlanta, Georgia, USA, 2022.
4. **Z. Feng, A.J. Gallo, Y. Liu, A.K. Pamososuryo, R.M.G. Ferrari, J.W. van Wingerden.** An economic model predictive control approach for load mitigation on multiple tower locations of wind turbines. In *IEEE 61st Conference on Decision and Control (CDC)*, Cancún, Mexico, 2022.
3. **A.K. Pamososuryo, Y. Liu, T.G. Hovgaard, R.M.G. Ferrari, J.W. van Wingerden.** Individual pitch control by convex economic model predictive control for wind turbine side-side tower load alleviation. In *The Science of Making Torque from Wind (TORQUE)*, Delft, Netherlands, 2022.
2. **Y. Liu, A.K. Pamososuryo, R.M.G. Ferrari, T.G. Hovgaard, J.W. van Wingerden.** Blade effective wind speed estimation: a subspace predictive repetitive estimator approach. In *European Control Conference (ECC)*, Rotterdam, Netherlands, 2021.
1. **S.P. Mulders, A.K. Pamososuryo, J.W. Van Wingerden.** Efficient tuning of individual pitch control: a Bayesian optimization machine learning approach. In *The Science of Making Torque from Wind (TORQUE)*, Delft, Netherlands, 2020.

 Included in this thesis.

 Winner of the 2023 *O. Hugo Schuck Best Paper Award: Application Category* from the American Automatic Control Council.